LASER-DRIVEN PROTON BEAMS:

Mechanisms for spectral control and efficiency enhancement

Ceri M. Brenner

A thesis submitted for the degree of Doctor of Philosophy

Department of Physics, University of Strathclyde

2012

Declaration of authorship

This thesis is the result of the author's original research. It has been composed by the author and has not been previously submitted for examination which has led to the award of a degree.

Signed:
Date: 17/08/2012

Abstract

This thesis reports on investigations of proton acceleration driven by the interaction of short, intense laser pulses with thin, solid targets. Laser-driven plasma interactions are used to establish accelerating quasi-electrostatic field gradients, on the rear surface of the target, that are orders of magnitude higher than the current limit of conventional, radio-frequency-based accelerator technology. The resulting high energy (multi-MeV) proton beams are highly laminar, have ultra-low emittance, and the inherently broad energy spectrum is particularly effective for use in proton imaging, heating and transmutation applications. This thesis reports on a series of investigations carried out to explore routes towards control of the spectral properties of laser-driven proton sources and optimisation of laser-to-proton energy conversion efficiency.

The dependence of laser accelerated proton beam properties on laser energy and focal spot size in the interaction of an intense laser pulse with an ultra-thin foil is explored at laser intensities of 10^{16}-10^{18} W/cm^2. The results indicate that whilst the maximum proton energy is dependent on both these laser pulse parameters, the total number of protons accelerated is primarily related to the laser pulse energy. A modification to current analytical models of the proton acceleration, to take account of lateral transport of electrons on the target rear surface, is suggested to account for the experimental findings. The thesis also reports on an investigation of optical control of laser-driven proton acceleration, in which two relativistically intense laser pulses, narrowly separated in time, are used. This novel approach is shown to deliver a significant enhancement in the coupling of laser energy to medium energy (5-30 MeV) protons, compared to single pulse irradiation. The ‘double-pulse’ mechanism of proton acceleration is investigated in combination with thin targets, for which refluxing of hot electrons between the target surfaces can lead to optimal conditions for coupling laser drive energy into the proton beam. A high laser-to-proton conversion efficiency is measured when the delay between the pulses is optimised at 1 ps. The subsequent effect of double-pulse drive on the angular distribution of the proton beam is also explored for thick targets.

Role of the author

With reference to the list of publications that follow, the author has contributed to an extensive amount of international, collaborative experimental work in high-power laser-plasma interactions during the course of the PhD.

The author gained experience of ion acceleration diagnostic design and implementation during experimental campaigns carried out using the Astra-Gemini laser at the Central Laser Facility (CLF), UK, and the PHELIX laser at the GSI Helmholtz Centre for Heavy Ion Research GmbH (GSI) in Germany. Experiments involving short-pulse laser interactions with solid-density targets were performed to investigate the physics of laser-driven for ion acceleration [5] [7] [17], for diagnostic development [12] [14] and to study efficient harmonic generation from reflection at the front surface [2], [11]. In particular, the author took a lead role in the design, construction and running of proton beam spatial profile diagnostics, mainly employing radiochromic (RCF) dosimetry film stacks. Proton beams were measured as part of experimental campaigns conducted to investigate hot electron generation and transport in dense plasma [8], including the effects of lateral beam spreading [4] and refluxing in thin foils [13], and the combination of these effects on rear surface sheath-acceleration fields [3] [6]. The author actively contributed to all of these experimental campaigns.

The author contributed to the development of a scintillator-based ion beam profiler described in [9] by running an early version of the diagnostic during an experimental campaign carried out using the J-KAREN laser at the Advanced Photon Research Centre in Japan, investigating optimisation and control of proton acceleration from thin target foils [1].

The author carried out a detailed analysis of proton beam scaling with laser energy and intensity using data acquired during an experimental campaign on the Astra laser, at the CLF, UK, in August-September 2007. This resulted in a lead-author publication [10] (reported in chapter 5), building on work performed in the context of an earlier publication of [16]. Modifications to analytical modelling of laser-driven proton acceleration (to reproduce the results reported in [10]) were carried out by the author, and are also reported in chapter 5. All simulations and subsequent analysis reported in chapter 6 were carried out by the author.

Analysis carried out by the author of the angular distribution of double-pulse accelerated proton beams measured using RCF stacks contributed towards an exploration of the observed energy-conversion efficiency enhancements reported in [15]. The author progressed to a leading role in the planning and running of an experimental campaign carried out using the Vulcan Petawatt laser at the CLF, UK, in August-September 2010 to investigate the double-pulse mechanism in combination with thin foils (reported in chapter 7). Extraction of proton beam dose from RCF stacks and subsequent spectral and angular analysis of the resultant proton beam spatial-intensity distribution was carried out by author.

Publications

1. “Quasi-monochromatic pencil beam of laser-driven protons generated using a conical cavity target holder”
M. Nishiuchi, A. S. Pirozhkov, H. Sakaki, K. Ogura, T. Zh. Esirkepov, T. Tanimoto, M. Kanasaki, A. Yogo, T. Hori, A. Sagisaka, Y. Fukuda, Y. Matsumoto, S. Entani, S. Sakai, **C. Brenner**, D. Neely, T. Yamauchi, S. V. Bulanov and K. Kondo. *Physics of Plasmas* 19, 030706 (2012)

2. “Soft X-ray harmonic comb from relativistic electron spikes”
A. S. Pirozhkov, M. Kando, T. Zh. Esirkepov, P. Gallegos, H. Ahmed, E. N. Ragozin, A. Ya. Faenov, T. A. Pikuz, T. Kawachi, A. Sagisaka, J. K. Koga, M. Coury, J. Green, P. Foster, **C. Brenner**, B. Dromey, D. R. Symes, M. Mori, K. Kawase, T. Kameshima, Y. Fukuda, L. Chen, I. Daito, K. Ogura, Y. Hayashi, H. Kotaki, H. Kiriyama, H. Okada, N. Nishimori, T. Imazono, K. Kondo, T. Kimura, T. Tajima, H. Daido, P. Rajeev, P. McKenna, M. Borghesi, D. Neely, Y. Kato and S. V. Bulanov. *Physical Review Letters* 108, 135004 (2012)

3. “Influence of laser irradiated spot size on energetic injection and proton acceleration in foil targets”
M. Coury, D. C. Carroll, A. P. L. Robinson, X. H. Yuan, **C. M. Brenner**, M. Burza, R. J. Gray, M. N. Quinn, K. L. Lancaster, Y. T. Li, X. X. Lin, O. Tresca, C.-G. Wahlström, D. Neely and P. McKenna. *Applied Physics Letters* 100, 074105 (2012)

4. “Surface transport of energetic electrons in intense picosecond laser-foil interactions”
R. J. Gray, X. H. Yuan, D. C. Carroll, **C. M. Brenner**, M. Coury, M. N. Quinn, O. Tresca, B. Zielbauer, B. Aurand, V. Bagnoud, J. Fils, T. Kühl,X. X. Lin, C. Li, Y. T. Li, M. Roth, D. Neely and P. McKenna. *Applied Physics Letters* 99, 171502 (2011)

5. “Proton acceleration using 50 fs, high intensity ASTRA-Gemini laser pulses”.

R. Prasad’ , S. Ter-Avetisyan, D. Doria, K.E. Quinn, L. Romagnani, P.S. Foster, **C.M. Brenner**, J.S. Green, P. Gallegos, M.J.V. Streeter, D.C. Carroll, O. Tresca, N.P. Dover, C.A.J. Palmer, J. Schreiber, D. Neely, Z. Najmudin, P. McKenna, M. Zepf and M. Borghesi. *Nuclear Instruments and Methods in Physics Research Section A: Accelerators, Spectrometers, Detectors and Associated Equipment*, 653 (1), 113–115 (2011)

6. “Controlling the properties of ultraintense laser–proton sources using transverse refluxing of hot electrons in shaped mass-limited targets”
O Tresca, D C Carroll, X H Yuan, B Aurand, V Bagnoud, **C M Brenner**, M Coury, J Fils, R J Gray, T Kühl, C Li, Y T Li, X X Lin, M N Quinn, R G Evans, B Zielbauer, M Roth, D Neely and P McKenna, *Plasma Physics and Controlled Fusion*, 53, 105008 (2011)

7. “Fast ion acceleration from thin foils irradiated by ultra-high intensity, ultra-high contrast laser pulses”
R. Prasad, A. A. Andreev, S. Ter-Avetisyan, D. Doria, K. E. Quinn, L. Romagnani, **C. M. Brenner**, D. C. Carroll, N. P. Dover, D. Neely, P. S. Foster, P. Gallegos, J. S. Green, P. McKenna, Z. Najmudin, C. A. J. Palmer, J. Schreiber, M. J. V. Streeter, O. Tresca, M. Zepf, and M. Borghesi. *Applied Physics Letters*. 99, 121504 (2011)

8. “Effect of lattice structure on energetic electron transport in solids irradiated by ultraintense laser pulses”
P. McKenna, A. P. L. Robinson, D. Neely, M. P. Desjarlais, D. C. Carroll, M. N. Quinn, X. H. Yuan, **C. M. Brenner**, M. Burza, M. Coury, P. Gallegos, R. J. Gray, K. L. Lancaster, Y. T. Li, X. X. Lin, O. Tresca, and C.-G. Wahlström. *Physical Review Letters*, 106, 185004 (2011)

9. “Scintillator-based ion beam profiler for diagnosing laser-accelerated ion beams”
J. S. Green, M. Borghesi, **C. M. Brenner**, D. C. Carroll, N. P. Dover, P. S. Foster, P. Gallegos, S. Green, D. Kirby, K.J. Kirkby, P. McKenna, M. J. Merchant, Z.

Najmudin, C. A. J. Palmer, D. Parker, R. Prasad, K.E. Quinn, P. P. Rajeev, M. P. Read, L. Romagnani, J. Schreiber, M. J. V. Streeter, O. Tresca, M. Zepf and D. Neely. *Proc. SPIE 8079*, 807919 (2011)

10. “Dependence of laser accelerated protons on laser energy following the interaction of defocused, intense laser pulses with ultra-thin targets”
C. M. Brenner, J. S. Green, A. P. L. Robinson, D. C. Carroll, B. Dromey, P. S. Foster, S. Kar, Y. T. Li, K. Markey, C. Spindloe, M. J. V. Streeter, M. Tolley, C. –G. Wahlstrom, M. H. Xu, M. Zepf, P. McKenna and D. Neely. *Laser and Particle Beams*, 29 (3), 345-351 (2011)

11. “Relativistic plasma surfaces as an efficient second harmonic generator”
M.J.V. Streeter, P.S. Foster, F.H. Cameron, M. Borghesi, **C.M. Brenner**, D.C. Carroll, E. Divall, N.P. Dover, B. Dromey, P. Gallegos, J.S. Green, S. Hawkes, C.J. Hooker, S. Kar, P. McKenna, S.R. Nagel, Z. Najmudin, C.A.J. Palmer, R. Prasad, K.E. Quinn, P.P. Rajeev, A.P.L. Robinson, L. Romagnani, J. Schreiber, C. Spindloe, S. Ter-Avetisyan, O. Tresca, M. Zepf and D. Neely**.** *New Journal of Physics*, 13 023041 (2011)

12. “Spatially resolved X-ray spectroscopy using a flat HOPG crystal”
X.H. Yuan, D.C.Carroll, M.Coury, R.J.Gray, **C.M.Brenner**, X.X.Lin, Y.T.Li, M.N. Quinn, O.Tresca, B.Zielbauer, D.Neely, P.McKenna. *Nuclear Instruments and Methods in Physics Research Section A: Accelerators, Spectrometers, Detectors and Associated Equipment*, 653 (1), 145–149 (2011).

13. “Refluxing of fast electrons in solid targets irradiated by intense, picosecond laser pulses”
M N Quinn, X H Yuan, X X Lin, D C Carroll, O Tresca, R J Gray, M Coury, C Li, Y T Li, **C M Brenner**, A P L Robinson, D Neely, B Zielbauer, B Aurand, J Fils, T Kuehl and P McKenna. *Plasma Physics and Controlled Fusion*, 53 025007 (2011)

14. “Calibration of Thomson parabola—MCP assembly for multi-MeV ion spectroscopy”
R. Prasad, D. Doria, S. Ter-Avetisyan, P.S. Foster, K.E. Quinn, L. Romagnani, **C.M. Brenner**, J.S. Green, P. Gallegos, M.J.V. Streeter, D.C. Carroll, O. Tresca, N. Dover, C.A.J. Palmer, J. Schreiber, D. Neely, Z. Najmudin, P. McKenna, M. Zepf and M. Borghesi. *Nuclear Instruments and Methods in Physics Research Section A: Accelerators, Spectrometers, Detectors and Associated Equipment*, 623 (2), 712–715 (2010).

15. “Spectral Enhancement in the Double Pulse Regime of Laser Proton Acceleration”
K. Markey, P. McKenna, **C. M. Brenner**, D. C. Carroll, M. M. Gunther, K. Harres, S. Kar, K. Lancaster, F. Nu¨rnberg, M. N. Quinn, A. P. L. Robinson, M. Roth, M. Zepf, and D. Neely. *Physical Review Letters*, 105, 195008 (2010)

16. “Enhanced proton flux in the MeV range by defocused laser irradiation”
J S Green, D C Carroll, **C Brenner**, B Dromey, P S Foster, S Kar, Y T Li, K Markey, P McKenna, D Neely, A P L Robinson, M J V Streeter, M Tolley, C-G Wahlström, M H Xu and M Zepf. *New Journal of Physics*, 12, 085012 (2010).

17. “Carbon ion acceleration from thin foil targets irradiated by ultra-high contrast, ultraintense laser pulses”
D C Carroll, O Tresca, R Prasad, L Romagnani, P S Foster, P Gallegos S Ter-Avetisyan, J S Green, M J V Streeter, N Dover, C A J Palmer, **C M Brenner**, F H Cameron, K E Quinn, J Schreiber, A P L Robinson, T Baeva, M N Quinn, X H Yuan, Z Najmudin, M Zepf, D Neely, M Borghesi and P McKenna. *New Journal of Physics*, 12, 045020 (2010).

18. “Evolution of elastic x-ray scattering in laser-shocked warm dense lithium”
N. L. Kugland, G. Gregori, S. Bandyopadhyay**, C. M. Brenner**, C. R. D. Brown, C. Constantin, S. H. Glenzer, F. Y. Khattak, A. L. Kritcher, C. Niemann, A. Otten, J. Pasley, A. Pelka, M. Roth, C. Spindloe, and D. Riley. *Physical Review E*, 80, 066406

(2009).

Acknowledgements

There are many people to whom I owe a great deal, and must express my appreciation for, in helping me to reach the finishing line of my PhD journey. Too many to mention here, but there are a few to whom I doff my cap.

First, I would like to express my sincere gratitude to my excellent supervisors David Neely and Paul McKenna for giving me this great opportunity and for passing on their wisdom and experience – thank you. I would also like to thank Todd Huffman and Gianluca Gregori for their encouragement and support during my undergraduate degree and for that first summer placement at the Central Laser Facility (CLF), which led to my discovery of the exciting field of high power laser-plasma physics.

To John Pasley, thank you for being a true friend and great mentor from the very beginning. Many thanks also go to James Green and David Carroll for being fantastic post-docs; for their guidance and for teaching me the ways of experimental research. Alex Robinson has my immense gratitude for the theoretical support he provides to our experimental data; for use of his simulation code and the excellent viva tutorials that he orchestrated - thank you. To my Strathclyde research group - Olivier, Graeme, Ross, Pablo, Mireille, David M, Xiaohui, Mark – thank you for being a great team to be a part of.

Having spent the duration of my PhD at the CLF, I would also like to thank the CLF staff for being so welcoming and supportive, with a special mention to the target fabrication team, engineering group and laser scientists - you are a credit to the facility, thank you for always being so accommodating. Thank you to Robbie Scott, Keith Markey and the Vulcan team for helping me acquire that important final data set and to Satya Kar for helping me extract the result. Thank you especially to the experimental science group and to Peta Foster and Kate Lancaster for being great plasma companions and fellow science communicators.

To all of my colleagues in the LIBRA consortium, especially those with whom I have been on experiments, I would like to extend my thanks. I have also been very fortunate to have had the opportunity to participate in experimental campaigns outside of the UK; thank you to Alexander Pirozhkov and Paul Bolton for hosting me at PMRC, Japan, Igor Pogorelsky at BNL, New York, and the PHELIX team at GSI, Germany.

A nod to those great friends, old and new, scientists and non-scientists, who provided many a happy distraction to see me through the last year; you know who you are - thank you.

Finally, I would like to show my appreciation to my parents, sisters and Jonathan. Thank you for believing in me and for getting me to, and through, university, twice. Your love and patience provided the strength and determination I needed; this work is dedicated to you.

Contents

1.Introduction 1

1.1. A brief history 2

1.2. Motivation behind laser-driven ion acceleration research 3

1.3. Thesis overview 6

2. Laser-plasma interactions 11

2.1. Ionisation 12

2.2. Plasma 14

2.3. Wave propagation in a plasma 16

2.4. Plasma electrons under the influence of the laser fields 17

2.5. Laser energy absorption by plasma electrons 21

2.5.1. Collisional processes 21

2.5.2. Collisionless processes 23

2.6. Suprathermal (hot) electron beam generation and transport in solid targets ... 25

2.6.1. Electron beam parameters relevant to laser-driven ion acceleration 26

2.6.2. Electron beam transport relevant to laser-driven ion acceleration 30

3. Laser-driven ion acceleration 38

3.1. Introduction 39

3.2. Laser-driven ion acceleration by surface electrostatic sheath fields 40

3.2.1. Target Normal Sheath Acceleration (TNSA) mechanism 40

3.2.2. Plasma-sheath expansion models for ion acceleration 43

3.2.3. Scaling of ion beam parameters with laser parameters 48

3.2.4. Spatial and angular characteristics of sheath acceleration........................ 50

3.3. Advanced laser-driven ion acceleration concepts 52

3.3.1. Advanced TNSA techniques.. 52

3.3.1.1. Multi-pulse sheath acceleration (MPSA).. 52

3.3.1.2. Self-induced transparency and the laser break-out afterburner (BOA) technique 54

3.3.2. Alternative laser acceleration mechanisms.. 56

3.3.2.1. Shock acceleration 56

3.3.2.2. Radiation pressure acceleration (RPA)... 57

4. Methods.. 64

4.1. Introduction to high power laser systems and the CPA technique................. 65

4.2. Laser systems used 66

4.2.1. Astra laser.. 67

4.2.2. Vulcan Petawatt laser 68

4.2.3. Vulcan Petawatt in double-pulse mode 70

4.3. Amplified spontaneous emission (ASE) and laser contrast ratio 71

4.3.1. Improving the intensity contrast of a laser pulse..................................... 72

4.4. Experiment diagnostics 74

4.4.1. Radiochromic film (RCF) proton detector stacks.................................... 75

4.4.1.1. Proton beam dose extraction from RCF stacks................................. 77

4.4.1.2. Proton beam analysis using RCF stacks 80

4.4.2. Thomson parabola ion spectrometer.. 82

4.4.2.1. Proton beam spectra extraction from TP ion spectrometers.............. 84

4.4.3. Reflectivity monitor.. 85

4.5. Numerical simulations using 1D Particle-In-Cell (PIC) codes 86

5. Scaling of laser-driven sheath acceleration of protons following the interaction of intense, defocused laser pulses with ultra-thin foil targets 93

5.1. Introduction 94

5.2. Experimental method.. 95

5.3. Fluence of accelerated protons as a function of laser energy and focal spot... 98

5.3.1. Experimental results 98

5.3.2. Discussion: dependence of proton fluence on laser energy.................... 105

5.4. Maximum proton energy as a function of laser energy and focal spot size .. 109

5.4.1. Experimental results 109

5.4.2. Discussion: dependence of maximum proton energy on laser energy and focal spot size.. 111

5.5. An analytical approach to modeling the laser-plasma interaction................. 113

5.5.1. Maximum proton energy as a function of laser intensity 113

5.5.2. Modelling the effect of a large focal spot size on the maximum proton energy.. 115

5.6. Conclusion and summary 120

6. 1D simulations of a moderately intense laser plasma interaction 125

6.1. Simulating laser-driven ion acceleration using a PIC code 126

6.2. Proton spectra obtained with varying laser intensity 126

6.2.1. Comparison of 1D simulation with experimental results 128

6.2.2. Introduction of an ultra-short plasma scale length at the target front surface 131

6.2.3. Simulated laser-plasma absorption and hot electron temperature as a function of laser intensity 135

6.3. Discussion 139

7. Development of the Multiple Pulse Sheath Acceleration technique 143

7.1. Multiple pulse sheath acceleration 144

7.1.2. Development of the double-pulse acceleration technique 145

7.2. Experimental arrangement 147

7.3. Results 149

7.3.1. Proton fluence enhancement using thin foils 149

7.3.2. Laser energy to proton energy conversion efficiency 154

7.3.2. Reflectivity monitor 156

7.3.4. Angular distribution of the proton beam 157

7.3.5. Proton beam divergence 159

7.4. Modelling the divergence of the plasma expansion 161

7.5. Summary and conclusion 165

8. Conclusion and future outlook 169

8.1. Thesis summary and further work 170

8.1.1. Spectral control 170

8.1.2. Conversion efficiency enhancement 172

8.2. Future outlook for laser-driven proton acceleration 173

8.2.1. Proton beam delivery and laser intensity distribution 173

8.2.2. Novel target design and laser cutting technique for demonstration of advanced laser proton acceleration schemes 174

8. Appendix A 180

A.1. Spectra obtained using Thomson parabola spectrometers 180

A.2. Divergence as a function of proton energy using sheath model 181

Chapter 1: Introduction

This chapter serves to provide the reader with background and motivation for the field of research from which this thesis has derived: laser-driven ion acceleration. A brief introduction is given to the developments leading up to successful experimental demonstration of MeV proton beams from intense laser-plasma interactions. There are many fields, from medicine to high energy density physics, to which laser-produced ion beams can be applied and, in some cases, perhaps provide a better alternative to conventional particle accelerator technology. A selection of these applications will be introduced, along with the requirements of the proton beams to enable these. Finally, an outline of the thesis content is given.

1.1. A brief history

When the laser was invented in 1960 [1] [2] it was referred to as ‘a solution looking for a problem’. Since then, improvements and developments in laser technology have opened the door to hundreds of uses for lasers. From barcode scanners to medical scalpels, from CD and DVD players to industry production lines to investigating plasma physics in the laboratory, the laser has proven itself to be a versatile and world-changing piece of technology.

Plasma, the exotic, fourth state of matter is a result of a material being heated to such an extent that electrons are stripped from their host atoms, thus producing an ionised, gaseous medium. It is in this state that processes such as fusion, recombination and therefore narrow-band light production or electrical conductivity can occur; which has given rise to many applications for plasmas from plasma TVs and strip lighting to the promising potential of fusion fuelled power stations. Almost as soon as the laser had been realised, these concentrated packets of light energy were considered for plasma production in the laboratory [3] [4]. Furthermore, their use in the study of high energy density physics and specifically for laser-driven fusion, were one of the first challenges for which the laser was deemed a solution.

While ion emission from laser produced plasmas has been measured since the 1960’s [5] [6], a proposition for laser produced plasmas to be used specifically for compact particle acceleration was first made in 1979 by Tajima and Dawson [7]. The study focused on electron beam generation and remained purely theoretical until the laser technology managed to deliver intensities up to 10^{15} W/cm^2 that were high enough to explore this idea experimentally. In the early years of laser-plasma acceleration, the focus was on laser accelerated beams of electrons and the subsequent gamma-ray and x-ray production that also comes as a result of a laser-plasma interaction. Laser produced beams of ions were also studied at these moderate laser intensities [8] [9] however their potential as compact ion sources was stifled due to their low particle flux and poor beam quality compared to conventionally sourced (RF) beams.

When the intensity threshold of the original laser chain systems was surpassed with the introduction of the chirped pulse amplification technique (see chapter 3) in 1985 [10], new regimes of laser-plasma interaction were enabled. High current beams of electrons with relativistic energies could now be produced and the field of laser-plasma acceleration rapidly grew into a very active area of laser-plasma physics, see [11] [12] [13] for detailed topical reviews. At about the same time, a significant amount of high quality, ionising radiation in addition to the electrons was also being produced, which was soon discovered to be ions of ~ MeV energy. In 2000, the production of highly laminar, ultra-short multi-MeV ion beams was first reported by a handful of experimental groups [14] [15] [16]. Having experimentally realised a high quality laser-driven ion source, the promise of a compact and novel particle accelerator scheme that could respond to flexible demands remains one of the key motivators for a great deal of work in the field of laser-plasma interaction physics.

1.2 Motivation behind laser-driven ion acceleration research

Ion accelerator technology was first established in the 1930s and has since seen rapid progress, leading to the development of the tunable and reproducible ion sources that are available today. ‘Conventional’ systems source the acceleration with the use of a series of electrodes that generate alternating electric fields through which the ions pass and experience successive ‘push’ and ‘pull’ effects. The electric field alternation typically reaches the radio frequency range for high ion energies, hence the term RF cavity. Cyclic variations of the cavity structure can be used in combination with magnetic fields to confine the ions to an orbit of increasing radius (cyclotrons), while the most advanced systems rely on electric and magnetic fields that adjust for relativistic ion energies and maintain a fixed orbital radius (synchrotrons). The minimum size of an ion accelerator is defined by the maximum accelerating gradient that the structure can host which, unfortunately for conventional systems, is limited to ~ 10^7 V/m with even the best superconducting cavities before field-induced break down of the solid material occurs. Add to this the substantial amount of radiation shielding and costly structural components involved and the motivation to develop alternative schemes is one driven by a requirement of compactness and flexible delivery, which is highly desirable for the applications of ion beams explored in this chapter.

Highly ionised plasma offers the potential to host accelerating gradients that are many orders of magnitude higher than solid state systems with short, intense laser pulses acting as the driver to generate them. Intense laser irradiation of a solid density target creates a region of high energy density at the laser focus in which concentrated bunches of plasma electrons are accelerated to relativistic energies, creating charge separation fields of the order TV/m that are sustained over longitudinal distances of nanometres to microns. Under such fields, bright (~ 10^{12} ions per pulse), ultra-short (~ ps) multi-MeV ion beams are generated. Furthermore, the ultra-low transverse emmittance (< 0.004 mm·mrad) [17] of laser-driven ion beams offers a substantial improvement (two orders of magnitude) over RF-accelerated beams. As such, laser-driven ion sources are considered as potential replacements for traditional injector systems for conventional accelerator technology, enhancing the peak brightness of the beam. It is therefore imperative that knowledge of how the ion beam properties vary with laser parameters is well understood. Currently, ion beams with an exponentially decreasing energy spectrum extending to a maximum energy which scales with the laser irradiance ($I_L\lambda^2$) have been produced by many experimental groups worldwide.

Owing to the small effective source area (< 10 μm^2) and short bunch duration, **proton radiography and probing** can be used to monitor density variations and the temporal evolution of electric fields in a sample with unprecedented spatial (micron) and temporal (picoseconds) resolution. An ‘image’ of the proton beam after propagating through a sample can be formed by using stacks of particle dosimetry media such as Radiochromic film. Density variations can be detected by utilising the energy loss characteristics of protons passing through matter and electric fields can be measured from the deflection of the protons. In situ, ultra-fast proton imaging of plasma evolution, for example, is an application that can only be realised with laser-driven acceleration as the driver (laser) can be easily guided to a point of interest and the broad spectral distribution of currently available beams means that they are effectively ‘chirped’; the fastest protons arrive ahead of the bunch and capture an image at an earlier time than those of lower energy at the rear of the proton front. This advanced imaging technique has already been established experimentally [18] [19] [20] [21] and is proving to be a popular choice of probing technique for various laser-plasma interactions [22] [23].

Further use of the short bunch duration of a laser-driven proton beam can be made for **isochoric heating of matter**. This method is highly beneficial compared to conventionally sourced, relatively ‘long’ pulse (ns) beams given that a high flux, laser-driven proton beam can be delivered to a secondary target within a few picoseconds, before significant hydrodynamic expansion occurs. Controlled, uniform heating of a sample material under a single density state can be used to determine fundamental material properties, such as the equation of state and opacity. Consequently, laser-driven ion sources are preferential for use in warm-dense matter production and the study of high energy density physics, in which their application could be particularly effective. Laser-driven proton heating was first demonstrated by Patel *et al* [24] in 2003 and has since seen considerable development [25] [26] and continued use [27] [28] .

Exploiting the potential of localised heating over picoseconds timescales of material at high density achievable with medium energy (5-30 MeV) protons, laser-driven proton beams have also been considered as ignitor beams in the **fast-ignition (FI) scheme of laser fusion** [29]. The FI approach to laser fusion scheme separates the compression and heating phases. Long pulse laser irradiation (~ ns) first compresses the fusion fuel capsule via laser ablation of the outer shell, driving spherical converging shocks, and then a second high intensity laser-accelerated particle beam would be used to super-heat the compressed fuel to temperatures under which high-gain fusion reactions can be ignited. Temporal *et al* [30] used 2D simulations to suggest that a broad spectrum proton beam with temperature ~ 3 MeV and containing ~ 10-25 kJ of energy could be sufficient for high-gain fusion ignition. The HiPER [31] project is exploring many schemes for laser-based, high-gain fusion from laser-driven shock ignition to the FI approach, however significant coupling efficiency between laser and proton beam energy needs to be achieved before protons can be considered for the ignitor beam over a laser-driven electron beam.

In a similar vein, medium energy (10-30 MeV) laser-driven ion beams have also been considered for the **production of short-lived medical isotopes**, used in positron emission tomography (PET) imaging, for example [32] [33] [34]. The potential to use compact and bright laser-driven proton sources to drive nuclear reactions is attractive for both economic and accessibility reasons. Furthermore, using laser-driven proton beams for **neutron generation** is of considerable interest for studies of impulsive damage of matter, replicating the conditions on the first wall of a fusion reactor for example [35].

Proton imaging, heating and transmutation are applications for which currently available laser-driven proton beams could be optimised and would offer significant benefits compared to conventional alternatives. A more detailed review of the potential applications of laser-driven proton sources is given in [36]. The proton beam properties that are required for these applications are focusability, determined by the emmitance and divergence, short duration, significant laser-to-proton conversion efficiency (~ 10%) and controllable spectral distribution. The first of these two are already at or within satisfactory acceptance values using currently available beams. However the last two requirements have yet to be met with full reproducibility. As such, the work presented in this thesis concentrates on the optimisation and control of the spectral content of currently achievable laser-driven proton beams, that could potentially be used for the applications explored above.

1.3 Thesis overview

In the chapters that follow, an introduction to the plasma physics involved in short pulse, intense laser interactions with solid density targets is provided (chapter 2) in preparation for an overview of the mechanisms and theory behind laser-driven proton acceleration (chapter 3). Chapter 4 introduces the reader to high-power laser pulse generation and the methods used to obtain the measurements presented in the results chapters, 5-7.

Chapters 5 and 6 present an investigation of the interaction of a moderately intense, ultra-short (40 fs) laser pulse with ultra-thin (25 nm thick) foil targets. In chapter 5, the scaling of maximum proton energy and proton flux is investigated experimentally as a function of both laser pulse energy and intensity. A modification to current models of proton acceleration is suggested to account for the experimental findings. Chapter 6 presents a numerical investigation of the laser-plasma interaction conditions experimentally investigated in chapter 5 and discusses the benefits and limitations of modelling the underlying physics in 1D. Chapter 7 reports on an investigation involving the use of two intense laser pulses, narrowly separated in time, to significantly enhance the coupling of laser energy to medium energy (5-30 MeV) protons. The first half of this chapter explores the possibility of combining this all-optical enhancement technique with thin targets, in which significant flux enhancement can be obtained, in order to optimise the laser-to-proton conversion efficiency. In the latter part of this chapter, the resulting affect on the angular distribution of these double-pulse accelerated proton beams is reported on.

Chapter 8 encompasses a summary of the key conclusions that can be drawn from the investigations presented in this thesis and discusses future directions for further work relating to laser-driven proton acceleration.

References

1. Gould, R.G. The LASER, light amplification by stimulated emission of radiation. In *The Ann Arbor Conference on Optical Pumping, the University of Michigan* (1959), 128.
2. Maiman, TH. Stimulated Optical Radiation in Ruby. *Nature*, 187, 4736 (1960), 493--494.
3. Linlor, WI. Plasma Produced by Laser Bursts. *Bull. Am. Phys. Soc*, 7 (1962), 440.
4. Linlor, W.I. Some Properties of Plasma Produced by Laser Giant Pulse. *Physical*

Review Letters, 12, 14 (1964), 383--385.

5. Linlor, W.I. Ion energies produced by laser giant pulse. *Appl. Phys. Letters*, 3 (1963).
6. Fenner, NC. Ion energies in the plasma produced by a high power laser. *Physics Letters*, 22, 4 (1966), 421--422.
7. Tajima, T. and Dawson, JM. Laser electron accelerator. *Physical Review Letters*, 43, 4 (1979), 267--270.
8. Gitomer, SJ, Jones, RD, Begay, F., Ehler, AW, Kephart, JF, and Kristal, R. Fast ions and hot electrons in the laser--plasma interaction. *Physics of Fluids*, 29 (1986), 2679.
9. Kishimoto, Y., Mima, K., Watanabe, T., and Nishikawa, K. Analysis of fast-ion velocity distributions in laser plasmas with a truncated Maxwellian velocity distribution of hot electrons. *Physics of Fluids*, 26 (1983), 2308.
10. Strickland, D. and Mourou, G. Compression of amplified chirped optical pulses. *Optics Communications*, 55, 6 (1985), 447--449.
11. Umstadter, D. Relativistic laser--plasma interactions. *Journal of Physics D: Applied Physics*, 36 (2003), R151.
12. Joshi, C. and Malka, V. Focus on laser-and beam-driven plasma accelerators. *New Journal of Physics*, 12 (2010), 045003.
13. Ledingham, KWD and Galster, W. Laser-driven particle and photon beams and some applications. *New Journal of Physics*, 12 (2010), 045005.
14. Clark, EL, Krushelnick, K., Zepf, M. et al. Energetic heavy-ion and proton generation from ultraintense laser-plasma interactions with solids. *Physical review letters*, 85, 8 (2000), 1654--1657.
15. Maksimchuk, A., Gu, S., Flippo, K., Umstadter, D., and Bychenkov, V.Y. Forward ion acceleration in thin films driven by a high-intensity laser. *Physical review letters*, 84, 18 (2000), 4108--4111.
16. Snavely, RA, Key, MH, Hatchett, SP et al. Intense high-energy proton beams from petawatt-laser irradiation of solids. *Physical Review Letters*, 85, 14 (2000), 2945--2948.

17. Cowan, TE, Fuchs, J., Ruhl, H. et al. Ultralow emittance, multi-MeV proton beams from a laser virtual-cathode plasma accelerator. *Physical review letters*, 92, 20 (2004), 204801.
18. Borghesi, M., Bigongiari, A., Kar, S. et al. Laser-driven proton acceleration: source optimization and radiographic applications. *Plasma Physics and Controlled Fusion*, 50 (2008), 124040.
19. Romagnani, L., Fuchs, J., Borghesi, M. et al. Dynamics of electric fields driving the laser acceleration of multi-MeV protons. *Physical review letters*, 95, 19 (2005), 195001.
20. Borghesi, M., Campbell, DH, Schiavi, A. et al. Electric field detection in laser-plasma interaction experiments via the proton imaging technique. *Physics of Plasmas*, 9 (2002), 2214.
21. Romagnani, L., Borghesi, M., Cecchetti, CA et al. Proton probing measurement of electric and magnetic fields generated by ns and ps laser-matter interactions. *Laser and Particle Beams*, 26, 02 (2008), 241--248.
22. Mackinnon, AJ, Patel, PK, Borghesi, M. et al. Proton radiography of a laser-driven implosion. *Physical review letters*, 97, 4 (2006), 45001.
23. Sarri, G., Cecchetti, CA, Romagnani, L. et al. The application of laser-driven proton beams to the radiography of intense laser--hohlraum interactions. *New Journal of Physics*, 12 (2010), 045006.
24. Patel, PK, Mackinnon, AJ, Key, MH et al. Isochoric heating of solid-density matter with an ultrafast proton beam. *Physical review letters*, 91, 12 (2003), 125004.
25. Mancic, A., Robiche, J., Antici, P. et al. Isochoric heating of solids by laser-accelerated protons: Experimental characterization and self-consistent hydrodynamic modeling. *High Energy Density Physics*, 6, 1 (2010), 21--28.
26. Roth, M., Alber, I., Bagnoud, V. et al. Proton acceleration experiments and warm dense matter research using high power lasers. *Plasma Physics and Controlled Fusion*, 51 (2009), 124039.
27. Pelka, A., Gregori, G., Gericke, DO et al. Ultrafast melting of carbon induced by

intense proton beams. *Physical review letters*, 105, 26 (2010), 265701.

28. Snavely, RA, Zhang, B., Akli, K. et al. Laser generated proton beam focusing and high temperature isochoric heating of solid matter. *Physics of Plasmas*, 14 (2007), 092703.
29. Roth, M., Cowan, TE, Key, MH et al. Fast ignition by intense laser-accelerated proton beams. *Physical review letters*, 86, 3 (2001), 436--439.
30. Temporal, M., Honrubia, JJ, and Atzeni, S. Numerical study of fast ignition of ablatively imploded deuterium--tritium fusion capsules by ultra-intense proton beams. *Physics of Plasmas*, 9 (2002), 3098.
31. Batani, D., Koenig, M., Baton, S. et al. The HiPER project for inertial confinement fusion and some experimental results on advanced ignition schemes. *Plasma Physics and Controlled Fusion*, 53 (2011), 124041.
32. Spencer, I., Ledingham, KWD, Singhal, RP et al. Laser generation of proton beams for the production of short-lived positron emitting radioisotopes. *Nuclear Instruments and Methods in Physics Research Section B: Beam Interactions with Materials and Atoms*, 183, 3 (2001), 449--458.
33. Ledingham, KWD, McKenna, P., McCanny, T. et al. High power laser production of short-lived isotopes for positron emission tomography. *Journal of Physics D: Applied Physics*, 37 (2004), 2341.
34. Lefebvre, E., d’Humières, E., Fritzler, S., and Malka, V. Numerical simulation of isotope production for positron emission tomography with laser-accelerated ions. *Journal of applied physics*, 100 (2006), 113308.
35. Perkins, LJ, Logan, BG, Rosen, MD et al. The investigation of high intensity laser driven micro neutron sources for fusion materials research at high fluence. *Nuclear fusion*, 40 (2000), 1.
36. Borghesi, M., Fuchs, J., Bulanov, SV, Mackinnon, AJ, Patel, PK, and Roth, M. Fast ion generation by high-intensity laser irradiation of solid targets and applications. *Fusion science and technology*, 49, 3 (2006), 412--439.

Chapter 2: Laser-plasma interactions

Short, intense pulses of laser light impacting on a solid foil target will very quickly ionise and drive the material into the plasma state. The physics governing the subsequent laser-plasma interaction is introduced in this chapter, as a prologue to the experimental results presented in later chapters.

2.1. Ionisation

The mechanisms which lead to laser-driven ion acceleration are a result of the interaction between the strong electromagnetic fields of a laser pulse and an ionised medium. The processes that lead to the ionisation of matter in the presence of such fields are not of primary concern in this study. However it is important to recognise the initial steps that occur before the main interaction physics is discussed. Furthermore, ionisation of atoms in the presence of strong quasi-electrostatic fields leads to ion acceleration from the non-irradiated side of a solid foil target, as described in the following chapter.

Laser-atom interactions can be characterised by comparing the electric field strength in the Coulomb potential of a hydrogen atom to the field strength within in a high-intensity laser pulse. At the Bohr radius, a_B, the electron is bound to the nucleus by the atomic unit of electric field, E_{atom}.

$$a_B = \frac{4\pi\varepsilon_0\hbar^2}{m_e e^2} \cong 5.3 \times 10^{-11}\ \mathrm{m} \tag{2.1}$$

$$E_{atom} = \frac{e}{4\pi\varepsilon_0 a_B^2} \cong 5.1 \times 10^{9}\ \mathrm{Vm^{-1}} \tag{2.2}$$

where ε_0 is the permittivity of free space, $\hbar$ is the reduced Planck's constant and m_e and e are the electron mass and charge respectively. This leads to a definition of the **atomic unit of intensity**, $\boldsymbol{I_{atomic}}$, at which the laser field is equal to the binding field experienced by the electron, given by

$$I_{atomic} = \frac{\varepsilon_0 c E_{atom}^2}{2} \cong 3.51 \times 10^{16}\ \mathrm{Wcm^{-2}} \tag{2.3}$$

The majority of laser-driven ion acceleration experiments are carried out using laser intensities, I_L, that far exceed this value, thus ensuring ionisation of the target material.

However, ionisation can also occur at intensities below this threshold. An electron can be excited from the atom by the absorption of a single high frequency photon, as in the photoelectric effect, or, in the case of sufficiently high photon density, many photons with energy lower than the ionisation potential can be absorbed by the electron in a process called **multi-photon ionisation**. Laser intensities above 10^{10} W/cm^2 are sufficient to observe this process and **above-threshold ionisation** has also been reported, whereby an electron absorbs more photons than needed to be free of the host atom.

At laser intensities approaching the atomic intensity, the laser field is strong enough to significantly distort the binding field experienced by the electron. The Coulomb barrier is suppressed by the presence of the strong electric field of the laser pulse, which enables the electron to quantum mechanically tunnel free with some finite probability. This is known as **tunnelling ionisation**. The transfer from a regime where multi-photon ionisation is dominant to one where tunnelling ionisation is significant can be distinguished using the Keldysh parameter, γ_K, which relates the strength of the laser potential to that experienced by an electron, given by:

$$\gamma_K = \sqrt{\frac{V_{ion}}{2U_p}} \tag{2.4}$$

where V_{ion} is the ionisation potential and U_p is the time averaged kinetic energy of a free electron oscillating in the laser's electric field known as the ponderomotive potential of the laser pulse, given by:

$$U_p = \frac{e^2 E_0^2}{4 m_e \omega_L^2} \tag{2.5}$$

where E_o is the peak electric field and ω_L is the laser frequency. Therefore, for $\gamma_K > 1$ the ionisation can be described as a multi-photon process and for $\gamma_K < 1$ the ionisation process is primarily down to a tunnelling process.

In the case of even higher laser intensities the barrier can be sufficiently suppressed to below the ionisation potential so that spontaneous emission of the electron can occur, leading to **over-the-barrier** or **barrier suppression ionisation**. For example, the threshold laser intensity for barrier suppression to occur for Hydrogen is only 1.4 x 10^{14} W/cm^2, thus indicating the need for the intensity of any pre-pulses arriving before the main pulse to be below this threshold if one requires there to be limited ionisation of the target surface prior to the arrival of the main pulse.

Another mechanism which is significant at the front surface of laser pulse interactions with solid density targets, such as those used in the work presented herein, is **collisional ionisation**. Once there is a sufficient population of free electrons, the rate of ionisation through collisions with atoms and ions becomes dominant compared to field distortion effects.

2.2. Plasma

The ionisation induced during the rising edge of the laser pulse rapidly transforms the irradiated surface, known as the front surface, of the target from being a cold solid state to a plasma state of matter. A plasma can be formally described as [1]:

‘*a quasi-neutral gas of charged and neutral particles which exhibits collective behaviour*’.

On a macroscopic scale, the plasma medium is considered to be charge neutral and ‘collective behaviour’ denotes that the motion of the plasma components directly affects those around them through the generation of electromagnetic forces that act over a large number of particles.

A plasma is often described using key properties such as the **free electron density**, $\boldsymbol{n_e}$ [m^{-3}], and the **plasma electron temperature**, $\boldsymbol{T_e}$, written as $k_B T_e$ when measured in units of energy such as electron-volts [eV] (1 eV = 1.6 x 10^{-19} J ≈ 10^4 K), where k_B is the Boltzmann constant. For the type of plasmas that are produced during the intense laser-solid interactions presented in this work typical values for the electron density and temperature are $10^{25} \rightarrow 10^{29}$ m^{-3} and keV→MeV respectively.

Due to their much lower charge-to-mass ratio, the plasma ions are considered immobile on the timescale of an optical period compared to the plasma electrons, forming a positive background to which the electrons respond to. The motion of the electrons in response to the potential of an ion in their vicinity will be to group around the ion, thus effectively shielding the ion and limiting the distance over which the field will penetrate into the plasma. The Coulomb potential, $V_{Coulomb}$, of an ion with charge state, Z^*, will therefore decrease exponentially over distance, r, with a decay length that is characteristic of the plasma.

$$V_{Coulomb}\,(r) = \frac{Z^*}{4\pi\varepsilon_0 r}\exp\left(-\frac{r}{\lambda_D}\right) \tag{2.6}$$

The distance over which this potential decreases to 1/e (~ 37 %) of the maximum value is known as the **Debye length**, $\boldsymbol{\lambda_D}$, of the plasma and is dependent on both the temperature, T_e, and density, n_e, of the plasma electrons as:

$$\lambda_D = \sqrt{\frac{\varepsilon_0 k_B T_e}{n_e e^2}} \tag{2.7}$$

The Debye length is commonly used to depict the distance beyond which an ion's electric field is sufficiently shielded so as to have negligible effect on any other surrounding plasma particles.

Energetic electrons within a plasma medium that are displaced from the uniform ion background will experience a restoring force due to their charge separation which then acts to reverse the electrons' motion. The electrons typically overshoot their equilibrium position and an oscillatory, simple-harmonic motion is established with a frequency that is characteristic of a plasma with electron density, n_e, known as the **plasma frequency**, $\boldsymbol{\omega_p}$.

$$\omega_p = \sqrt{\frac{e^2 n_e}{\varepsilon_0 \gamma m_e}} \tag{2.8}$$

Here, use has been made of the relativistic Lorentz factor, γ, of the electrons averaged over one oscillation period, where $\gamma = \frac{1}{\sqrt{1-\beta^2}} = \sqrt{1+\left(\frac{|\boldsymbol{p}|}{m_e c^2}\right)}$.

A plasma, being a hot ionised gas, will have a pressure associated with it, causing it to expand into the surrounding vacuum. The rate of expansion is highly dependent on the motion of the heaviest species, the ions, under the influence of the temperature of the plasma particles. Plasma expansion during a laser-plasma interaction can thus be described using the **ion sound speed**, $\boldsymbol{c_s}$:

$$c_s = \sqrt{\frac{k_B(Z^* T_e + T_i)}{m_i}} \tag{2.9}$$

where Z^* is the ion charge state, k_BT_e is the plasma electron temperature in eV, k_BT_i is the plasma ion temperature in eV and m_i is the ion mass.

The heating and subsequent pressure gradient induced by the laser-plasma interaction causes the front surface plasma to expand outwards. In doing so the step-like density profile of the cold target now becomes one that, in the case of a simple isothermal expansion, falls off exponentially with a **plasma scale length**, $\boldsymbol{L_0}$:

$$n_e(z) = n_0 \exp\left(-\frac{z}{L_0}\right) \tag{2.10}$$

where z is the distance away from the target front surface and n_0 is the initial electron density of the target. The plasma scale length therefore characterises the distance over which the electron density falls to n_0/e ~ $0.37n_0$. One can estimate the plasma scale length with the use of an expansion time, τ_{exp}, and the ion sound speed:

$$L_0 \approx c_s\tau_{exp} \tag{2.11}$$

A plasma's scale length is normally compared to the laser wavelength, λ_L, in order to define its size. 'Long' plasma scale lengths are for the case of $L_0 >> \lambda_L$ and 'short' plasma scale lengths are for the case where $L_0 \leq \lambda_L$. The plasma scale length is a useful parameter to be aware of during a laser-plasma interaction as it can be an indicator as to how the laser's energy is absorbed by the plasma electrons, as discussed in section 2.5.

2.3. Wave propagation in a plasma

The wave equation for a laser propagating through a plasma in which there are small density variations and quasi-neutrality holds ($\rho \approx 0$), is given by:

$$\nabla^2\boldsymbol{E} = \frac{1}{c^2}\frac{\partial^2\boldsymbol{E}}{\partial t^2} + \mu_0\frac{\partial\boldsymbol{j}}{\partial t} \tag{2.12}$$

where the current density, $\boldsymbol{j}$, is given by $\boldsymbol{j} = -en_e\frac{d\boldsymbol{r}}{dt}$, n_e being the electron density and μ_0 being the permeability of free space. Using a wave solution of the form:

$$\boldsymbol{E} = E_0\hat{\mathrm{e}}_{\boldsymbol{x}}\, e^{[i(\boldsymbol{kz}-\omega t)]} \tag{2.13}$$

along with the electrostatic force experienced by an electron in the presence of an ion:

$$\boldsymbol{F_e} = m_e \frac{d^2\boldsymbol{r}}{dt^2} = -e\boldsymbol{E} \tag{2.14}$$

and substituting into the terms of the wave equation, equation 2.14 becomes:

$$-k^2\boldsymbol{E} = -\frac{1}{c^2}\,\omega_L^{\boldsymbol{2}}\boldsymbol{E} + \mu_0 \frac{e^2 n_e \boldsymbol{E}}{m_e} \tag{2.15}$$

Making use of equation 2.8 and re-arranging, one notices that the **dispersion relation** for a wave travelling through a plasma is very similar to that for travelling through vacuum, apart from the inclusion of the plasma frequency term:

$$\omega_L^2 - \omega_p^2 = k^2c^2 \tag{2.16}$$

This result embodies a description of laser pulse propagation through plasma as it immediately shows that the wavevector, k, is only real when the laser frequency, ω_L, exceeds the plasma frequency, ω_p. At the point at which the plasma frequency equals the laser frequency, the laser pulse can no longer propagate and is reflected. The point at which the laser pulse reflects in the plasma's density profile is known as the **critical surface**. Given that the plasma frequency is a function of electron density, a **critical electron density** can be defined, using equation 2.8, at which the plasma frequency equals the laser frequency:

$$n_c = \frac{\gamma \varepsilon_0 m_e \omega_L^2}{e^2} \tag{2.17}$$

The use of the Lorentz factor in equation 2.17 is only relevant when the laser intensity becomes relativistic and in doing so, the critical surface is effectively shifted further into the target; an effect known as **laser-induced transparency**.

The critical electron density can be used to define two regions of the plasma; one in which the laser pulse can propagate, known as **under-dense,** for which $n_e < n_c$ and one in which the laser pulse cannot propagate, known as **over-dense,** for which $n_e > n_c$.

2.4. Plasma electrons under the influence of the laser's fields

The motion of a single electron of charge, e, and velocity, $\boldsymbol{v}$, in the electric, $\boldsymbol{E}$, and magnetic, $\boldsymbol{B}$, fields of a laser pulse can be described using the Lorentz force equation:

$$\boldsymbol{F_L} = \frac{d\boldsymbol{p}}{dt} = -e(\boldsymbol{E} + \boldsymbol{v} \times \boldsymbol{B}) \tag{2.18}$$

where $\boldsymbol{p} = \gamma m_e \boldsymbol{v}$ is the momentum of the electron with the inclusion of the relativistic factor, γ , written as a function of the electron's velocity as a fraction of the speed of light, $\beta = v / c$.

In the case that the electron is moving non-relativistically, where $v << c$, the effect of the laser's magnetic field on the electron is negligible and the electron is confined to oscillate, with a quiver velocity defined by the laser frequency, ω_L, in a plane defined by the laser's polarisation, perpendicular to the laser propagation axis. However as the electron's kinetic energy approaches that of its rest mass energy the magnetic component term ($e\boldsymbol{v}$ x $\boldsymbol{B}$), which acts in the longitudinal direction of the laser axis, has a significant effect on the electron's subsequent motion. It is useful at this point to introduce the normalised vector potential of the laser field, commonly presented as the **dimensionless light amplitude**, $\boldsymbol{a_0}$.

$$a_0 = \frac{eE_0}{\omega_L m_e c} = \sqrt{\frac{I_L \lambda_L^2}{1.37\ x\ 10^{18}}} \tag{2.19}$$

in which the laser intensity, I_L, is calculated in units of W/cm^2 and the wavelength of the laser, λ_L, is given in units of μm.

The value of a_0 is an indicator of the ratio of the force acting longitudinally to that of the force acting transversely, which can also be interpreted as the ratio of the relativistic to classical momenta. It can therefore be used to define whether the laser intensity is in the non-relativistic regime; $a_0 << 1$, or the regime in which relativistic effects need to be considered; $a_0 \geq 1$. The combination of these component terms under linear polarisation results in the electron oscillating with a figure-of-eight motion, the longitudinal motion becoming ever more dominant with increasing a_0 and the electron experiencing a net drift along the laser axis. Over a single laser cycle of an infinite plane wave laser field the electron does not receive a net gain of energy and will eventually return to rest after the laser pulse has passed.

However, in reality, a laser pulse has a finite beam waist and in the case of a tightly focused laser beam its spatial profile will have considerable radial variation; the intensity, typically, being centrally peaked. The time-averaged oscillation potential of the laser varies over the beam area which means that an electron moving across this gradient will not experience an equal restoring force. In other words, a break in the planar symmetry of the situation described above results in an electron being driven out of an area of high intensity over the first half of the laser cycle and experiencing a weaker return effect during the second half-cycle of the laser oscillation. Therefore, the electron receives a net gain in energy over the laser cycle.

In the case of a relativistic laser interaction using linear polarisation a time-averaged force, the **ponderomotive force**, acts to drive an electron away from regions of high intensity along the laser propagation axis. The ponderomotive force can be defined in terms of the gradient of these variations in the spatial component of the electric field, E_s, as so:

$$\boldsymbol{F_{pond}} = -\frac{e^2}{4m_e\omega_L^2}\nabla E_s^2 = -m_e c^2\sqrt{1+\frac{a_0^2}{2}} \qquad (2.20)$$

for a relativistic laser-plasma interaction where a_0 is the dimensionless light amplitude defined by equation 2.19 and m_e is the electron mass (see [1] for derivation). The energy transferred to the electron during one laser cycle is therefore equivalent to the **ponderomotive potential**, $\boldsymbol{U_{pond}}$, given by:

$$U_{pond} = m_e c^2\left(\sqrt{1+\frac{a_0^2}{2}}-1\right) \qquad (2.21)$$

Other laser-plasma absorption processes will be discussed in the following section.

The ponderomotive force is independent of charge and so also acts on the heavy ions, however the ponderomotive potential experienced by an ion in the intensity regime investigated in this thesis ($I_L < 10^{20}$ W/cm^2) is much less than the rest mass energy of the ions and so they are considered to be quasi-stationary compared to the resultant electron motion.

As the laser travels through the under-dense region, the plasma medium can affect the laser's spatial profile and like-wise the laser pulse can affect the plasma density profile. The former is a result of the ponderomotive force expelling electrons from regions of the highest laser intensity, forming regions of electron depletion. For a laser pulse, the highest intensity is centred on the laser axis and so there will also exist a local minimum in the electron density on the laser axis, resulting in an electron density profile that is the inverse of the laser intensity profile. The importance of this result becomes apparent if one examines the definition of the **refractive index** of the plasma, η_{ref}.

$$\eta_{ref} \approx \sqrt{1-\left(\frac{\omega_p}{\omega_L}\right)^2} = \sqrt{1-\frac{n_e}{n_c}} \tag{2.22}$$

Thus, in regions where the electron density is minimal the refractive index will be a maximum and vice versa. The resulting refractive index profile, that of a convex lens, acts to focus the laser beam, further increasing the laser intensity in a process termed **self-focussing**.

The density profile of an expanding plasma can also be affected by the radiation pressure exerted in the domain of the critical surface by the relativistic laser interaction. If this radiation pressure exceeds the thermal pressure of the plasma, then **plasma density profile steepening** will occur which acts to resist and work against further expansion of the front surface plasma, therefore reducing the under-dense region.

For the experiments described herein, a sharp plasma density gradient, $L_0 \ll \lambda_L$, was maintained by limiting the amount of plasma expansion prior to the arrival of the intense laser pulse. This means that the laser was interacting with a plasma that was primarily over-dense. Even though the laser pulse will quickly reach the critical surface of the front surface plasma, it will still be able to penetrate evanescently into the over-dense region, exponentially attenuating as it does so over a distance known as the **skin depth**, $\boldsymbol{\delta}$. The wavevector, k, will be imaginary beyond the critical surface implying that the spatial dependence of the wave will take the form:

$$e^{i\boldsymbol{k}\boldsymbol{z}} = e^{-|\boldsymbol{k}|\boldsymbol{z}} = e^{-\frac{z}{\delta}} \qquad (2.23)$$

where

$$\delta = \frac{c}{\sqrt{\omega_p^2 - \omega_L^2}} \qquad (2.24)$$

Therefore a fraction of the laser pulse is able to penetrate through the mirror-like critical surface and transfer the laser's energy to those plasma electrons found within the skin depth layer of the over-dense region.

2.5. Laser energy absorption by plasma electrons

In the experimental investigations of laser driven ion acceleration described herein, the ions are not strongly accelerated by the laser-plasma interaction directly. Instead, the laser-plasma interaction first accelerates a population of electrons into the target which then subsequently accelerates ions under the correct conditions. The transfer of the laser's energy into a population of energetic electrons is therefore a crucial step, requiring an introduction to the processes that govern how the laser energy is absorbed by the plasma before proceeding to a full description of the ion acceleration mechanism.

As will become obvious, there is not just one single mechanism by which the laser energy is absorbed. Instead, there are a number of mechanisms that have become applicable as laser technology has improved and enabled different regimes of laser-plasma interaction to be explored; indeed, it is common for measurements of laser absorption to be accredited to a combination of several processes. The laser intensity, polarisation, contrast and plasma scale length are all parameters that can be used to distinguish the conditions under which each mechanism is dominant, as described below.

2.5.1. Collisional processes

A plasma can be described as being collisional if the mean free path of the plasma electrons is smaller than the linear dimensions of the plasma, in which case a substantial amount of those electrons undergo collisions with the plasma ions. In the case of laser-solid interactions using a laser pulse of relatively low laser intensity ($I_L < 10^{15}$ W/cm^2) these conditions are satisfied. The resultant effect is that electrons oscillating under the influence of the laser's fields (see section 2.3) will have their motion damped through collisions with the background ions, thus preventing energy being transferred back to the laser at the end of the laser cycle. Therefore, the laser experiences a net loss of energy which, during the collision, has been accumulated by the electrons and ions. The process by which plasma particles gain energy from incoming photons in the presence of colliding electrons and ions is known as **inverse bremsstrahlung heating** and is the dominant absorption mechanism in low temperature, long scale length collisional plasmas.

The process predominately occurs in regions of under-dense plasma up to the critical surface and is highly dependent on the electron-ion collision frequency, ν_{ei}, given by:

$$\nu_{ei} \propto \frac{n_e Z^*}{T_e^{\frac{3}{2}}} \tag{2.25}$$

where Z^* denotes the ionisation charge state of the plasma and therefore the number of electrons per ion. For interactions of a low intensity laser pulse with a long scale length plasma, L_0, hosting a linear density profile and a Maxwellian electron distribution, the fraction of laser energy absorbed by inverse bremsstrahlung, f_{IB}, is given by [2] [3]:

$$f_{IB} = 1 - \exp\left(-\frac{32}{15}\left(\frac{\nu_{ei}(n_e)}{c}\right)L_0\right) \tag{2.26}$$

These two relations indicate that collisional heating is maximised at the critical surface of high Z plasmas but that its contribution to the overall absorption rate will rapidly decrease with increasing plasma temperature, T_e. As the laser intensity increases above $I_L \sim 10^{15}$ W/cm^2 the oscillation velocity of the electron approaches that of the thermal velocity which acts to reduce the effective collision frequency further still [4] [5] at which point collisionless processes become the dominant absorption mechanism.

2.5.2. Collisionless processes

A p-polarised laser pulse is defined as one in which the electric field is oscillating in the plane of incidence. If a p-polarised laser pulse is incident on a slab of plasma at an angle, θ, to the target normal then it will refract as it travels through the plasma density gradient and eventually reflect at an electron density, n_{ref}, that is slightly lower than the critical density, where $n_{ref} = n_c \cos^2\theta$. The electric field component that runs parallel to the plasma density gradient (along the target normal axis) will tunnel through to the critical surface at which point the laser frequency and plasma frequency are in resonance, thus exciting electron plasma waves. A net transfer of energy from the laser to the plasma can be achieved through collisional damping of the resonant electron oscillations as described above, but in the case of high laser intensity, $I_L > 10^{15}$ W/cm^2, the amplitude of the plasma wave becomes large and wave breaking can occur which imparts kinetic energy to the electrons, injecting them into the plasma along the target normal. The fraction of laser energy transferred to the plasma through the process of **resonance absorption**, f_{RA}, is given by [3]:

$$f_{RA} \approx \frac{\phi^2(Q)}{2} \tag{2.27}$$

where

$$\phi \approx 2.3\, Q \exp\left(-\frac{2}{3}\, Q^3\right) \tag{2.28}$$

and

$$Q = \left(\frac{\omega_L L_n}{c}\right)^{\frac{1}{3}} sin\theta \tag{2.29}$$

Under optimised conditions of long plasma scale length and angle of incidence in the laser irradiance region $10^{12} < I_L\, \lambda_L^2 < 10^{17}$ W/cm^2 μm^2, this absorption mechanism is particularly effective, achieving absorption fractions of up to 50 % [6] into a population of energetic electrons that have a Maxwellian energy distribution.

For laser-plasma interactions in which the plasma scale length is very short and a steep density gradient exists, the plasma waves excited at the critical surface can drive electron displacements that are comparable to or greater than the plasma scale length. In this case, the standard approach to resonant absorption cannot apply. Instead, it was proposed by Brunel [7] that the electrons can gain energy directly from the component of the electric field that acts along the target normal axis. Electrons exposed to the laser field will first be pulled back into the vacuum and then as the field changes direction they will be accelerated forward into the plasma, parallel to the plasma gradient and, crucially, will drive beyond the critical surface into the over-dense region of the plasma. Given that the laser fields cannot penetrate further than the skin depth, the electrons cannot be further affected by the laser field and a net transfer of energy from the laser to the accelerated electron is achieved. This absorption mechanism, known as **vacuum heating**, is of particular importance to the work carried out in this thesis as it is one of the dominant processes for absorption in very short plasma scale length interactions ($L_0/\lambda_L < 0.1$) under moderate, short pulse laser irradiance. The fraction of the laser energy absorbed into the accelerated electrons through the process of vacuum heating, f_{VH}, is given by [3]:

$$f_{VH} = \frac{\eta_{osc}}{2\pi} \frac{v_N^3}{c v_0^2 cos\theta} \tag{2.30}$$

where η_{osc} is an absorption coefficient indicating how much oscillatory motion of the electrons is lost to heating the plasma, v_N is the electron quiver velocity due to the target normal component of the electric field and v_0 is the electron quiver velocity due to the laser electric field.

Like resonant absorption, vacuum heating requires there to be a component of the electric field present at the critical surface that is parallel to the plasma density gradient, therefore oblique incidence of p-polarised light onto a very steep plasma gradient are the ideal interaction conditions. The mechanism is optimised at an angle of incidence of 45° at which point the incident and reflected wave combine to maximise the electric field component normal to the target surface [8].

Another dominant absorption mechanism for short pulse laser interactions with steep plasma gradients is known as **relativistic *j x B* heating** [9]. In the relativistic interaction regime, where $a_0 > 1$, electrons are predominantly driven by the ***v*** x ***B*** component of the Lorentz force that acts in the longitudinal direction of the laser propagation. As described in section 2.3, electrons can be accelerated by the ponderomotive force of the laser pulse, gaining energy equivalent to the ponderomotive potential. The force can act on electrons up to and within the skin depth, wherein they undergo longitudinal oscillations at twice the laser frequency that launch them into the over-dense region of the plasma enabling them to travel into the bulk of the target with relativistic energies and exhibiting a quasi-Maxwellian velocity distribution. Unlike vacuum heating, ponderomotive heating is effective under both s- and p-polarised polarisation, but not under circular polarisation. Another distinction is that it will accelerate bunches of energetic electrons along the laser axis, doing so at twice the frequency as those accelerated by vacuum heating. The crucial difference being that under the $j \times B$ absorption mechanism the electrons are driven by the Lorentz force, whereas in the vacuum heating mechanism the electrons are driven by a component of the electric field acting along the target normal axis. This difference means that $j \times B$ heating is very effective for normal incidence onto a short scale length plasma and is thus the dominant absorption mechanism under this interaction condition. It is also reported to be optimised in the case that the plasma interaction density is close to the critical density [3]. In the case of ultra-intense laser interactions, for $I_L > 10^{20}$ W/cm^2, the electron motion is dominated by oscillation along the laser axis due to the $\boldsymbol{v} \times \boldsymbol{B}$ component compared to motion in the electric field component normal to the target surface and therefore the $j \times B$ heating mechanism is expected to dominate over vacuum heating.

2.6. Suprathermal (hot) electron beam generation and transport in solid targets

The generation of a population of energetic electrons at the front surface of the target through the absorption mechanisms mentioned in the previous section is an integral process to the laser driven ion acceleration mechanism that has been employed in the work of this thesis. The transport of these electrons through the dense target is an important step in the transfer of energy from the laser pulse to the ions that are accelerated from the rear surface. A brief review of the physics of hot electron generation and transport relevant to ion acceleration is given here. Electron beam transport is the result of a complex convolution of effects and as such is far from being completely understood, making it a very active area of laser-plasma research. For a more detailed introduction to this field of laser-plasma research, please refer to texts written by Gibbon [10] and Bell *et al* [11].

2.6.1. Electron beam parameters relevant to laser driven ion acceleration

As suggested in the introduction to laser absorption mechanisms, the laser pulse energy is primarily coupled to a population of hot electrons that exhibit a Maxwellian-like energy spectrum. Noting that a single temperature Maxwellian energy distribution as a function of the hot electron energy, E_{hot}, appears as so:

$$f(E_{hot}) = N_{hot}\sqrt{\frac{4E_{hot}}{\pi(k_B T_{hot})^3}}\exp\left(-\frac{E_{hot}}{k_B T_{hot}}\right) \tag{2.31}$$

implies that parameters such as the **total number of hot electrons**, $\boldsymbol{N_{hot}}$, and the **hot electron beam temperature**, $\boldsymbol{k_B T_{hot}}$, are sufficient to describe the hot electron population. As will become apparent in the following chapter, these parameters are also very relevant in ion acceleration and especially so in determining the properties of an ion beam accelerated from the rear surface of a solid target.

The spectrum of the initial forward propagating hot electrons is not readily directly measureable, given that the electrons are accelerated into a dense medium. Only a fraction of the electrons will be able to escape the target unperturbed before strong charge separation fields are developed that confine the beam to the target. The temperature of the escaping electron beam can be measured however, using a magnetic spectrometer, for example, from which the initial hot electron temperature is inferred by assuming a similarity between the temperature of the initial and escaping beam spectra [12]. Recent numerical work by Link *et al* [13] has compared the spectrum of the escaping electron beam to that of the initial propagating beam. They concluded that although the spectrum of an electron beam detected by a spectrometer is significantly modified compared to the original and has a much lower average energy, the hot electron slope temperature of the original is retained. A very similar result was found experimentally by Habara *et al* [14] by comparing the spectrum obtained by an electron spectrometer to that obtained from measurements of Cherenkov radiation. Indirect measurements of the hot electron temperature can also be made by spectrally resolving x-ray photon emission that is initiated as the hot electron passes through the target material [15]. The initial electron temperature is then computed by combining these secondary emission detections with the use of models. An approximation to the temperature of the hot electron population can therefore be extracted experimentally, which can provide information on the interaction at the front surface.

The scaling of hot electron temperature has been investigated experimentally and numerically as a function of laser irradiance, $I_L\lambda_L^2$, subsequently leading to the development of scaling relations that are widely used to estimate k_BT_{hot} in a given interaction. Simulations carried out to investigate resonance absorption (see section 2.5.2) [16] [17] found the hot electron component of the beam to scale as:

[16]
$$k_BT_{hot}\,(keV) \approx 14\,(k_BT_eI_{16}\lambda_L^2)^{\frac{1}{3}} \tag{2.32}$$

[17]
$$k_BT_{hot}\,(keV) \approx 20\,T_e^{\frac{1}{4}}\,(I_{16}\lambda_L^2)^{0.39} \tag{2.33}$$

where I_{16} is the laser intensity in units of 10^{16} W/cm^2, λ_L is the laser wavelength in units of microns and k_BT_e is the background electron plasma temperature in keV. Likewise, scaling relations for vacuum absorption were also developed using simulations. Gibbon [18] derived an experimentally relevant scaling relation in the case of moderate laser intensity ($I_L < 10^{17}$ W/cm^2) and very steep plasma gradients ($L_0 < 0.1\,\lambda_L$) that goes as:

$$k_BT_{hot} \approx 7\,(I_{16}\lambda_L^2)^{\frac{1}{3}} \tag{2.34}$$

Experimental investigations such as those carried out by Beg *et al* [15] and Chen *et al* [12] of hot electron temperature scaling with laser irradiance have confirmed a $I_L^{1/3}$ scaling dependence, therein given as:

[15]
$$k_BT_{hot} \approx 215\,(I_{18}\lambda_L^2)^{\frac{1}{3}} \tag{2.35}$$

[12]
$$k_BT_{hot} \propto (I_L\lambda_L^2)^{0.34} \tag{2.36}$$

where I_{18} is the laser intensity in units of 10^{18} W/cm^2 and I_L is the laser intensity. Interestingly, Beg *et al* report this scaling as being effective in the case of relatively long plasma scale lengths and for laser intensities below 10^{19} W/cm^2, whereas Chen *et al* report their scaling as being effective in the case of very steep plasma gradients in the laser intensity range I_L ~ 10^{18} – 10^{21} W/cm^2. The latter being of particular interest given that in the ultra-relativistic laser interaction regime (I_L > 10^{20} W/cm^2) the hot electron temperature is expected to be dominated by the $\boldsymbol{j} \times \boldsymbol{B}$ absorption mechanism, for which the scaling relation has been derived, for the case of linear polarisation, from simulations as being [19]:

$$k_B T_{hot}\,(\text{keV}) \approx 511\left(\sqrt{1+\left(\frac{I_L \lambda_L^2}{1.37\ x\ 10^{18}}\right)}-1\right) \qquad (2.37)$$

A number of reported measurements of hot electron temperature [20] [21] can be fitted with a trend line that goes as $(I_L \lambda_L{}^2)^{1/2}$, many of which have been extracted under conditions (plasma scale length, pulse duration, angle of incidence) that are preferential for ponderomotive heating.

The observations of Chen *et al* were described as being the result of oblique incidence in combination with the laser intensity being strong enough to rapidly increase the interaction density to well above critical; conditions under which the ponderomotive scaling (equation 2.37) might require modification and is superseded by vacuum heating absorption. The work of Tanimoto *et al* [21] also reported a departure from the ponderomotive scaling under a range of interaction conditions with the measured data following a scaling relation in closer agreement with that derived from the Haines relativistic model [22]:

$$k_B T_{hot}(\text{keV}) \approx 511\left(\sqrt{1+\sqrt{I_{18}\lambda_L^2}}-1\right) \qquad (2.38)$$

Kluge *et al* [23] have recently presented an interesting model for hot electron temperature for the case of ultra-short plasma scale length interactions that predicts a transition from a $I_L\lambda_L^2$ dependence for a_0 << 1 to a ~ $\sqrt{I_L\lambda_L^2}$ dependence for a_0 >> 1 which is well-matched to a collection of experimental and simulation measurements.

The total number of hot electrons**,** N_{hot}, can be approximated if one has a measure of the **efficiency of laser energy absorption into the hot electron beam**, $\boldsymbol{\eta_{L\to e}}$, by using:

$$N_{hot} = \frac{\eta_{L\to e}E_L}{k_B T_{hot}} \tag{2.39}$$

A review of the laser absorption mechanisms (see section 2.5) reveals how the achievable absorption rate during an interaction is very dependent on the scale length of the front surface plasma and in some cases the incident angle. Consequently, it is also very dependent on the temporal intensity contrast (see chapter 4) of the laser pulse as this will determine the extent of plasma formation prior to the arrival of the main pulse, known as ‘pre-plasma’. In comparing the measured values of laser absorption found in the literature it is therefore important to assess the pre-plasma conditions associated with the interaction. A recent and thorough review of published experimental and numerical values of laser absorption and hot electron conversion efficiency has been written by Davies [24]. The concluding remarks in this review and references therein state that for laser intensities between 10^{18} and 10^{21} W/cm^2 and sizeable plasma scale length, laser absorption increases with laser irradiance, $I_L\lambda_L^2$, increases for lower plasma densities and is highest at oblique angles of incidence. The scaling of laser absorption with laser irradiance has been found to increase with a power between 0.2 and 0.3 [24] [25] and yet it has also been found to scale much faster with laser intensity, as $I_L^{0.74}$ [26] [27]; the discrepancy between the two being the result of different laser contrast levels and therefore different front-surface plasma conditions. Experimentally it has been shown that the variation in laser absorption with increasing density scale length is complex [28]; initially increasing but then decreasing with increasing scale length above L_0>100 λ_L as significant pre-plasma causes the propagating beam to filament.

However, in the case of ultra-high contrast laser-plasma interactions whereby the front surface of the target is relatively undisturbed prior to the arrival of the main pulse, and the plasma scale length is much shorter than the wavelength, it has been found that the laser absorption is roughly constant across a wide range of laser intensities [29] [30].

The collective suggestion from a number of sources [24] [31] [32] [30] is that the laser to electron conversion efficiency is roughly in the range 20 % and 40 % but that it is difficult to be globally more precise than that due to differences in interaction conditions and the methods for absorption measurement as well as some discrepancies between parameter definitions. An absorption rate of ~ 30 % was found to be adequate for use in numerical modelling to reproduce experimental results [33] from Vulcan laser campaigns. Measurements made during the interaction of the ultra-short (50 fs), ultra-high contrast laser system Astra Gemini with a solid foil target have indicated that the laser absorption under these conditions is also around 30 % [29] [30]. Furthermore, Streeter *et al* were able to show that over the intensity range $I_L \sim 10^{17}$ - 10^{21} W/cm^2, the measured absorption fraction only increased by 8 % and was effectively constant (within error) over the intensity range $I_L \sim 10^{17} - 10^{19}$ W/cm^2 which is particularly noteworthy for the laser-plasma interaction conditions employed in the work presented herein.

2.6.2. Electron beam transport relevant to laser driven ion acceleration

The result of an intense laser interaction with a front-surface plasma is that a fraction of the laser's energy is coupled into a population of energetic electrons which subsequently pass straight into the solid region of the target. The mean free path of these suprathermal (hot) electrons is far longer than the thickness of the target used in such experiments enabling them to pass through the bulk of the target without significant scattering. However, a beam of these laser-accelerated hot electrons has a peak current of the order of ~ MA [34], the propagation of which, into the target, is not trivial. In the process of such a high current leaving the area of laser absorption at the front surface, a strong charge separation field develops which acts to inhibit the electron beam's propagation and confine it to the absorption region.

Yet, hot electron transport through solid targets is possible; the solution being provided by the existence of a **balancing return current** made up of a high-density population of thermal electrons that act to locally neutralise the hot electron beam. A **current balance relation** [11] in terms of the hot electron beam current density, $\boldsymbol{j}_{hot}$, and the cold return current density, $\boldsymbol{j}_r$, is used to illustrate this condition:

$$\boldsymbol{j}_{hot} + \boldsymbol{j}_r = 0 \tag{2.40}$$

The cold return current is sourced from the background electrons of the target and is drawn into the absorption region by the electric field that is generated by the escaping hot electron beam [35]. **Spatial current neutrality** is also vital so that the magnetic energy contained in the magnetic field generated around the region of beam propagation does not lead to an energy conservation violation as noted by Bell *et al* [36]. Therefore the return current must follow the same path as the hot electron current (but in the opposite direction).

Further evidence for the existence of current neutrality comes about when one considers the magnetic fields formed in response to high current flow. These self-generated magnetic fields grow with the current of the electron beam and can become so strong that they reverse the flow direction of the hot electrons; the threshold current for this happening being defined as the **Alfvén limit**, $\boldsymbol{I_A}$ [37] [38]:

$$I_A \cong \frac{m_e c^2 \beta\gamma}{e} = 1.7 \times 10^4 \beta\gamma \tag{2.41}$$

where $\beta = \frac{v_e}{c}$ and $\gamma = \frac{1}{\sqrt{1-\beta^2}}$, v_e being the electron velocity.

The Alfvén limit for laser interactions like those described in the work of this thesis is of the order of kA, which is far exceeded by the MA currents in the laser accelerated electron beams produced at the front surface. Therefore in order for these electrons to be able to propagate through the target a mechanism must be acting which neutralises the current of the forward propagating beam and ensures that it does not breach this limit.

The requirement on there being a return current generated in order for the hot electron beam to propagate means that hot electron transport is dependent on properties of the target, such as resistivity and free electron density. For example, the efficiency with which a balanced return current can develop will depend on the target material's resistivity, which in turn can affect the hot electron beam in terms of the energy losses associated with the work done against the inhibiting electric fields in the case of insufficient return current available at high resistivities. The dense, thermal return current is also collisional which means that the hot electron beam will be indirectly affected by collisions in the solid target material. The counter propagating nature of these beams of repelling electrons means that they are vulnerable to instabilities [39] which can hinder their propagation or filament the hot electron beam [40].

A necessity for the main ion acceleration scheme detailed in the next chapter is efficient transport of the hot electron population through to the rear surface of the target, therefore it also highly dependent on effective generation of a return current to achieve this. As well as target composition, the target thickness can also play a role in determining the effective density of hot electrons at the rear surface through a process known as **recirculation** which has been observed to be effective in very thin targets [41] [42] [43] [44].

When the hot electron beam breaks through the rear surface of the target foil, only a small percentage of the highest energy electrons will escape into the vacuum before an electrostatic field is formed in rapid response to the charge separation. This field is strong enough to reverse the direction of the remaining hot electrons and re-inject them back into the target. The same effect can also occur at the target's front surface so long as the target is thinner than the stopping distance of the energetic electrons in the target material (typically of the order of mm), effectively confining the hot electrons to the target. Recirculation is of noticeable importance to ion acceleration if the target is thin enough that recirculation occurs on a timescale of the order of the laser pulse duration, $\tau_{L,}$ under the condition that the target thickness, *d*, is given by:

$$d < \frac{c\tau_L}{2} \tag{2.42}$$

Using thin targets that satisfy this condition implies that energetic electrons reaching the target rear surface for the first time will be combined with electrons that have been recirculated through the target, thus enhancing the hot electron density at the rear surface which is favourable for rear surface ion acceleration. Use is made of targets that are ultra-thin with respect to the laser pulse length in the work of this thesis in order to exploit the benefits of recirculation for optimising the interaction conditions.

References

1. Chen, F.F. *Introduction to plasma physics and controlled fusion: plasma physics*. Springer, 1984.
2. Ginzburg, VL. *The propagation of electromagnetic waves in plasmas*. Pergammon Press (Oxford and New York), 1964.
3. Wilks, S.C. and Kruer, W.L. Absorption of ultrashort, ultra-intense laser light by solids and overdense plasmas. *Quantum Electronics, IEEE Journal of*, 33, 11 (1997), 1954--1968.
4. Gibbon, P. and Förster, E. Short-pulse laser-plasma interactions. *Plasma physics and controlled fusion*, 38 (1996), 769.
5. Pert, GJ. Inverse bremsstrahlung in strong radiation fields at low temperatures. *Physical Review E*, 51, 5 (1995), 4778.
6. Kieffer, JC, Audebert, P., Chaker, M. et al. Short-pulse laser absorption in very steep plasma density gradients. *Physical review letters*, 62, 7 (1989), 760--763.
7. Brunel, F. Not-so-resonant, resonant absorption. *Physical review letters*, 59, 1 (1987), 52--55.
8. Gibbon, P. and Bell, AR. Collisionless absorption in sharp-edged plasmas. *Physical review letters*, 68, 10 (1992), 1535--1538.

9. Kruer, WL and Estabrook, K. J$\times$ B heating by very intense laser light. *Physics of Fluids*, 28 (1985), 430.
10. Gibbon, P. *Short pulse laser interactions with matter*. Imperial College Press London, 2005.
11. Bell, AR, Davies, JR, Guerin, S., and Ruhl, H. Fast-electron transport in high-intensity short-pulse laser-solid experiments. *Plasma physics and controlled fusion*, 39 (1997), 653.
12. Chen, H., Wilks, SC, Kruer, WL, Patel, PK, and Shepherd, R. Hot electron energy distributions from ultraintense laser solid interactions. *Physics of plasmas*, 16 (2009), 020705.
13. Link, A., Freeman, RR, Schumacher, DW, and Van Woerkom, LD. Effects of target charging and ion emission on the energy spectrum of emitted electrons. *Physics of Plasmas*, 18 (2011), 053107.
14. Habara, H., Ohta, K., Tanaka, K.A. et al. Direct, absolute, and in situ measurement of fast electron transport via cherenkov emission. *Physical review letters*, 104, 5 (2010), 055001_1--055001_4.
15. Beg, FN, Bell, AR, Dangor, AE et al. A study of picosecond laser-solid interactions up to 1019 W cm-2. *Physics of Plasmas*, 4, 2 (1996), 447--457.
16. Forslund, DW, Kindel, JM, and Lee, K. Theory of hot-electron spectra at high laser intensity. *Physical Review Letters*, 39, 5 (1977), 284--288.
17. Estabrook, K. and Kruer, WL. Properties of resonantly heated electron distributions. *Physical Review Letters*, 40, 1 (1978), 42--45.
18. Gibbon, P. Efficient production of fast electrons from femtosecond laser interaction with solid targets. *Physical review letters*, 73, 5 (1994), 664--667.
19. Wilks, SC, Kruer, WL, Tabak, M., and Langdon, AB. Absorption of ultra-intense laser pulses. *Physical review letters*, 69, 9 (1992), 1383--1386.
20. Brandl, F., Pretzler, G., Habs, D., and Fill, E. \vCerenkov radiation diagnostics of hot electrons generated by fs-laser interaction with solid targets. *EPL (Europhysics Letters)*, 61 (2003), 632.
21. Tanimoto, T., Habara, H., Kodama, R. et al. Measurements of fast electron

scaling generated by petawatt laser systems. *Physics of Plasmas*, 16 (2009), 062703.

22. Haines, MG, Wei, MS, Beg, FN, and Stephens, RB. Hot-electron temperature and laser-light absorption in fast ignition. *Physical review letters,* 102, 4 (2009), 45008.
23. Kluge, T., Cowan, T., Debus, A., Schramm, U., Zeil, K., and Bussmann, M. Electron Temperature Scaling in Laser Interaction with Solids. *Physical Review Letters,* 107, 20 (2011), 205003.
24. Davies, JR. Laser absorption by overdense plasmas in the relativistic regime. *Plasma Physics and Controlled Fusion*, 51 (2009), 014006.
25. Ping, Y., Shepherd, R., Lasinski, BF et al. Absorption of short laser pulses on solid targets in the ultrarelativistic regime. *Physical review letters,* 100, 8 (2008), 085004.
26. Key, MH, Cable, MD, Cowan, TE et al. Hot electron production and heating by hot electrons in fast ignitor research. *Physics of Plasmas,* 5 (1998), 1966.
27. Town, RPJ, Chen, C., Cottrill, LA et al. Simulations of electron transport for fast ignition using LSP. *Nuclear Instruments and Methods in Physics Research Section A: Accelerators, Spectrometers, Detectors and Associated Equipment,* 544, 1 (2005), 61--66.
28. McKenna, P., Carroll, DC, Lundh, O. et al. Effects of front surface plasma expansion on proton acceleration in ultraintense laser irradiation of foil targets. *Laser and Particle Beams,* 26 (2008), 591--596.
29. Pirozhkov, AS, Choi, IW, Sung, JH et al. Diagnostic of laser contrast using target reflectivity. *Applied Physics Letters,* 94 (2009), 241102.
30. Streeter, MJV, Foster, PS, Cameron, FH et al. Relativistic plasma surfaces as an efficient second harmonic generator. *New Journal of Physics,* 13 (2011), 023041.
31. Myatt, J., Theobald, W., Delettrez, JA et al. High-intensity laser interactions with mass-limited solid targets and implications for fast-ignition experiments on OMEGA EP. *Physics of plasmas,* 14 (2007), 056301.
32. Nilson, PM, Theobald, W., Myatt, JF et al. Bulk heating of solid-density plasmas

during high-intensity-laser plasma interactions. *Physical Review E*, 79, 1 (2009), 016406.

33. Davies, JR, Bell, AR, Haines, MG, and Guerin, SM. Short-pulse high-intensity laser-generated fast electron transport into thick solid targets. *Physical Review E*, 56, 6 (1997), 7193.
34. Santos, JJ, Amiranoff, F., Baton, SD et al. Fast electron transport in ultraintense laser pulse interaction with solid targets by rear-side self-radiation diagnostics. *Physical review letters*, 89, 2 (2002), 25001.
35. Hammer, DA and Rostoker, N. Propagation of high current relativistic electron beams. *Physics of Fluids*, 13 (1970), 1831.
36. Bell, AR, Robinson, APL, Sherlock, M., Kingham, RJ, and Rozmus, W. Fast electron transport in laser-produced plasmas and the KALOS code for solution of the Vlasov--Fokker--Planck equation. *Plasma Physics and controlled fusion*, 48 (2006), R37.
37. Alfvén, H. On the motion of cosmic rays in interstellar space. *Physical Review*, 55, 5 (1939), 425.
38. Lawson, JD. On the classification of electron streams. *Journal of Nuclear Energy. Part C, Plasma Physics, Accelerators, Thermonuclear Research*, 1 (1959), 31.
39. Weibel, E.S. Spontaneously growing transverse waves in a plasma due to an anisotropic velocity distribution. *Physical Review Letters*, 2, 3 (1959), 83.
40. Batani, D., Manclossi, M., Santos, JJ, Tikhonchuk, VT, Faure, J., Guemnie-Tafo, A., and Malka, V. Transport of intense laser-produced electron beams in matter. *Plasma physics and controlled fusion*, 48 (2006), B211.
41. Mackinnon, A.J., Sentoku, Y., Patel, PK et al. Enhancement of proton acceleration by hot-electron recirculation in thin foils irradiated by ultraintense laser pulses. *Physical review letters*, 88, 21 (2002), 215006.
42. Sentoku, Y., Cowan, TE, Kemp, A., and Ruhl, H. High energy proton acceleration in interaction of short laser pulse with dense plasma target. *Physics of Plasmas*, 10 (2003), 2009.

43. Huang, Y., Lan, X., Duan, X. et al. Hot-electron recirculation in ultraintense laser pulse interactions with thin foils. *Physics of Plasmas*, 14 (2007), 103106.

44. Quinn, MN, Yuan, XH, Lin, XX et al. Refluxing of fast electrons in solid targets irradiated by intense, picosecond laser pulses. *Plasma Physics and Controlled Fusion*, 53 (2011), 025007.

Chapter 3: Laser-driven ion acceleration

The interaction of a sub picosecond, intense laser pulse with a solid foil target can be used to accelerate ions up to multi-MeV energies. This novel, next-generation particle acceleration mechanism is a very promising alternative to conventional accelerator technology. Motivated by the plethora of applications that laser-driven ion beams could lend themselves to (see chapter 1), ion acceleration remains a very active field of study in laser-plasma physics. The ephemeral processes that lead to the generation of bright, high-quality, ultra-short beams of laser-accelerated ions are introduced in this chapter, along with a brief summary of advances made in the field over the past decade.

3.1. Introduction

In the decades following the first experimental observation of laser-plasma accelerated ions in the 1960’s [1] [2] using long pulse (nanosecond), low intensity lasers, progress in the field was slow and restricted due to the inability of the laser systems available at the time to achieve intensities of more than $I_L \sim 10^{16}$ W/cm^2. Under such conditions, bursts of relatively low energy ions in quasi-thermal equilibrium with a directly accelerated hot electron population were produced and were described using plasma expansion models [3]. The introduction of the chirped pulse amplification (CPA) technique in 1985 [4] saw ultra-short laser pulses (≤ ps) being produced in the subsequent years which were capable of delivering intensities exceeding $I_L \sim 10^{18}$ W/cm^2 on to the target foil. It was in 2000 that the production of high quality, highly laminar, multi MeV ions from thin, laser irradiated foils was first reported [5] [6] [7]. Since then, a substantial amount of work has been dedicated to studying the underlying mechanisms behind this novel acceleration technique.

Over the last decade, a number of laser-driven ion acceleration mechanisms have been identified, distinguishable by the location of the charge separation induced by the laser-plasma interaction and the laser intensity. The most widely accepted mechanism behind many of the experimental observations of MeV proton beams made so far is Target Normal Sheath Acceleration (TNSA). The research presented in this thesis has been conducted in the TNSA dominated interaction regime and is therefore the primary focus of this chapter in preparation for the experimental work presented in later chapters. However, a brief description of alternative acceleration concepts has also been included at the end of this chapter for completeness.

3.2. Laser driven ion acceleration by surface electrostatic sheath fields

3.2.1 Target Normal Sheath Acceleration (TNSA) mechanism

As described in the previous chapter, the interaction of an intense laser pulse with a solid foil target results in the transfer of a fraction of the laser's energy into a population of suprathermal 'hot' electrons. These relativistic electrons are able to travel short distances through the solid medium of the target relatively unperturbed, the most energetic of which will actually be able to escape through the rear of the target. The escaping electrons will give rise to an electrostatic potential derived from the charge separation at the target-vacuum interface. The remaining oncoming electrons are consequently confined under Coulombic forces to a sheath field that extends outwards from the target surface over a distance characterised by the Debye length, λ_D, of the cloud of electrons (see chapter 2). The typical Debye length for laser plasma interactions similar to those described in this thesis being of the order of a few microns. The peak field, E_{sheath}, associated with the charge separation is given by the hot electron temperature, $k_B T_{hot}$ and the sound speed of the plasma, c_s, [8]:

$$E_{sheath} \sim \frac{2k_B T_{hot}}{e c_s \tau} \sim \frac{2k_B T_{hot}}{e L_n} \tag{3.1}$$

noting that $L_n \sim c_s \tau$ is the local plasma scale length, or the Debye length in this instance, which further implies that the peak field is also dependent on the hot electron density. The strength of the electrostatic sheath field that develops as laser accelerated electrons arrive on the rear surface is of the order TV/m which is strong enough to pull back the forward propagating hot electrons, injecting them back into the target to undergo recirculation (see chapter 2).

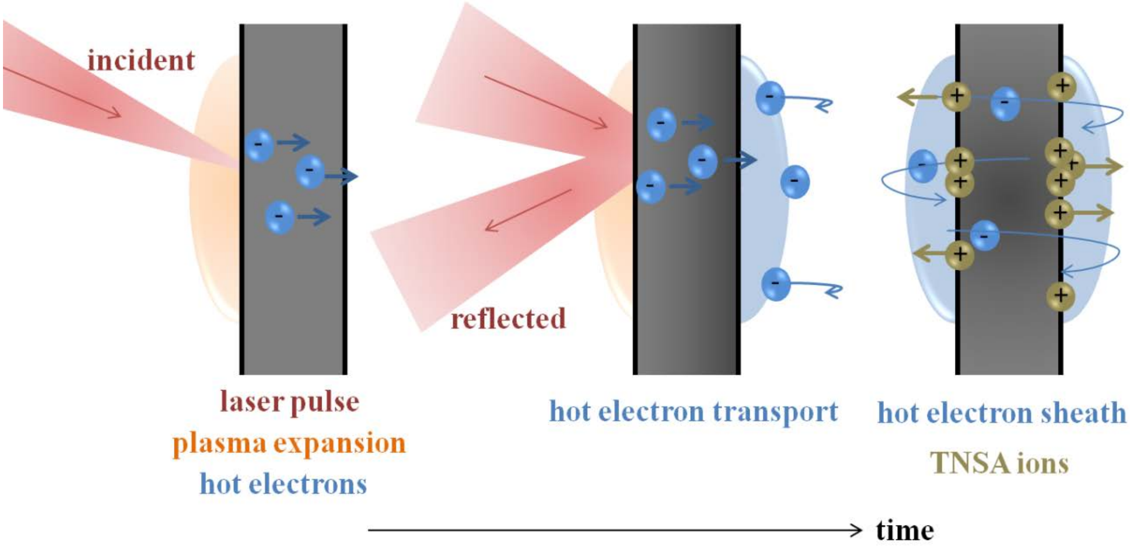

Figure 3.1: Schematic illustration of the TNSA mechanism over time, whereby protons are preferentially accelerated from contaminant layers (shown in black) on the surface of the target foil

Recalling the processes of ionisation described at the beginning of chapter 2, an electric field of this magnitude rapidly ionises atoms present on the rear surface of the target. For the laser and target parameter regime investigated in this thesis, barrier suppression ionisation has been found to be the dominant source of ions [9] [10] at the rear surface of a laser-irradiated foil target. Ions existing in a field of strength ~TV/m which is effective over a distance of a few microns will therefore be accelerated to the order of MeV energies, driving a plasma expansion from the rear surface in the target normal direction (see figure 3.1). Noting that, for the typical vacuum pressures and conditions used in these experiments, the surfaces of most materials are commonly coated with a thin (nm) layer of contaminant atoms such as water vapour and hydrocarbons, protons are almost always accelerated during the TNSA process and preferentially so, compared to heavier ions, due to their higher charge-to-mass ratio. Therefore, the plasma expansion will be dominated by a population of energetic protons, containing the majority of the energy transferred from the hot electrons, followed by a front of heavier ions such as carbon, oxygen and the target substrate nuclei.

A similar process, known as ‘sweeping acceleration’ [11], also accelerates ions in the forward and backward direction at the front surface of the target foil as a result of electrons being ponderomotively swept out of the laser irradiation area across the critical surface, leaving behind an electron depletion region. The potential difference between the two charge layers is in balance with the ponderomotive potential, U_p, of the laser pulse, which implies that the maximum ion energy obtained from sweeping acceleration is given by U_p [11] (typically < 1 MeV for $I_L \leq 10^{19}$ W/cm^2). The effectiveness of front surface acceleration is however also dictated by the plasma scale length and therefore the contrast of the laser pulse. Front surface ions that are accelerated into the target and penetrate through to the rear surface before the rear surface sheath field has decayed will also experience an acceleration boost. Fuchs *et al* [12] compared front and rear surface forward acceleration experimentally and found that ions accelerated from the rear surface were of higher maximum energy, lower divergence and contained a higher proportion of the energy converted to ions. Additionally, for thin foils in the refluxing regime (see chapter 2), the front surface sheath field that accelerates ions in the backward direction can be enhanced by the arrival of hot electrons that have been recirculated from the rear surface. For example, Ceccotti *et al* [13] observed very similar ion beam production at the front and rear surfaces when a high contrast laser pulse was used in combination with an ultra-thin target.

The mechanism known as *Target Normal Sheath Acceleration,* coined by Wilks *et al* in 2001 [14], was based on earlier work on electron driven plasma expansion [15] [16] and was used to explain the experimental observations noted in the pioneering work published in the year before. In the years that followed, a number of analytical models were proposed to describe the myriad of experimental observations of sheath-accelerated ion beams which were being reported. The most relevant of these models to the work presented herein are introduced below.

3.2.2. Plasma-sheath expansion models for ion acceleration

The effect of sheath field generation during the process of TNSA has been studied closely both numerically, through simulation codes, and also theoretically through the use of analytical models.

A detailed 1D model examining the ion front that results from an isothermal, collisionless plasma expansion into vacuum has been presented by Mora [8]. This analytical approach begins with a population of ions of density, n_{i0}, with a step-like distribution at the target-vacuum boundary, where x = 0, and a population of hot electrons of density, n_{h0}, and temperature, T_h, that exhibit a continuous, Boltzmann distribution:

$$n_h = n_{h0} \exp\left(\frac{e\Phi}{k_B T_h}\right) \tag{3.2}$$

where $\Phi(x)$ is the electrostatic potential generated as the electrons exit the target. Quasi-neutrality is assumed in the expanding plasma, $n_{h0} = Zn_{i0}$, and $\Phi(-\infty) = 0$, but this assumption is no longer valid when the plasma has expanded over a distance of the order of the Debye length, thereby defining a first-order maximum acceleration energy. Mora was able to show, by making use of the Poisson equation and finding a self similar solution to the fluid equations of continuity and motion, that the ion spectrum produced would be an exponentially decreasing function of ion energy with a cut-off given by:

$$E_{\max} = 2Zk_B T_h \left[\ln\left(\tau + \sqrt{\tau^2 + 1}\right)\right]^2 \tag{3.3}$$

where $\tau = \frac{\omega_{pi} t}{2\exp(1)}$ is the acceleration time, *t*, normalised to the ion plasma frequency, $\omega_{pi} = \sqrt{\frac{Zn_{ho}e^2}{\varepsilon_o m_i}}$. Similar models that examine charge separation effects on an expanding plasma cloud were also proposed by others [17] [18]. Passoni *et al* [18] described a stationary, isothermally expanding plasma cloud with a single electron temperature and used a spatial parameter to place a limit on the acceleration to ensure energy conservation, thus leading to the same conclusion that a maximum ion energy could be derived.

These simplified models are built upon there being a constant hot electron temperature which can only be reasonably assumed while the laser pulse is present. Consequently, the isothermal model approach has been found to be a suitable description of ion acceleration for ‘long’ laser pulse interactions (> ps) [19] where the laser pulse duration is comparable to the acceleration time. However, the isothermal, 1D plasma expansion model is an idealised approach as in reality the temperature of the hot electron population will decrease after the laser pulse has ended as energy is transferred to the ions, leading eventually to the ion front ‘catching up’ with the electron front and the electrostatic potential decreasing to zero, ending the acceleration.

Mora presented a modified version of the model that included an adiabatic description of the plasma expansion [20] as being better suited in the case of short laser pulse durations and ultrathin targets where the target thickness, L, is comparable to the initial Debye length of the hot electron population, λ_{D0}. Here, the maximum ion energy is given by:

$$E_{max} \cong 2Zk_BT_{h0}\left[\ln\left(a\frac{L}{\lambda_{D0}}+\ b\right)\right]^2 \tag{3.6}$$

where a and b are constants and are slight functions of hot electron temperature and can be found in reference [20]. The model was also improved with the addition of a dual electron temperature description as proposed by Passoni *et al* [21] which takes into account the presence of the cold electron background. Inclusion of both the hot (subscript h) and cold (subscript c) electron populations that exist during a laser-solid interaction (see chapter 2) in the plasma expansion model leads to an electric field at the target-vacuum boundary that is highly dependent on the ratio of the cold and hot electron pressures, $\frac{n_cT_c}{n_hT_h} = ab$, where a and b are the cold to hot electron density and temperature ratios respectively. For $ab \approx 1$ and $ab \ll 1$, the boundary electric field reduces to being approximately twice that given by the single electron temperature solution. Interestingly, in the case where the cold electron pressure dominates, where $ab \gg 1$, the boundary electric field is dominated by the parameters of the cold electron population:

$$E(x=0) \sim \sqrt{\frac{2}{\exp(1)}}\left(\frac{k_B T_c}{e\lambda_{dc}}\right) \tag{3.7}$$

where λ_{dc} is the cold electron Debye length. This results in a significant enhancement in the maximum electric field, compared to the opposite case, and furthermore the field will penetrate deeper into the target when the cold electron pressure dominates, thereby increasing the number of ions accelerated. The temperature, and therefore pressure, of the cold electron population can increase through Ohmic heating processes induced by the return current flowing through a highly resistive target material. Therefore, this effect is predicted to be noticeable for longer pulse durations of the order of hundreds of femtoseconds where a significant cold electron temperature boost is possible.

Robson *et al* [22] presented an interesting model which was developed to reproduce experimental results obtained using laser intensities in the range $10^{19} < I_L < 6 \text{ x } 10^{20}$ W/cm^2 with laser energy up to 400 J. Their two-phase temperature model included temporal variation of the electron temperature; rising linearly during the laser pulse duration and then cooling adiabatically at later times. Multi-dimensional effects of the radial plasma expansion were also approximated by curtailing the acceleration during the adiabatic phase at a time when the longitudinal expansion distance is twice that of the initial lateral extension of the plasma sheath. Employing these modifications, Robson *et al* reported much better agreement with experimental results of maximum proton energy, especially for increasing laser intensity where multidimensional effects become increasingly more important as the longitudinal excursion of energetic ions becomes of the order of the transverse plasma size in a shorter time [22]. Multi-dimensional considerations of the rear surface sheath are also shown to be of importance in determining the maximum proton energy in the case of defocused laser irradiation, as explored by Coury *et al* [23] and in chapter 5.

Refinements in the analytical modelling of sheath acceleration, such as incorporating the two distinct populations of electrons and the finite size of the target [24], have improved the predictive power of the fluid model, however they rely on approximations for the hot electron temperature and density at the rear of the target. Schreiber *et al* [25] have proposed a model based on the surface charge that develops as the electrons pass through which requires no description of the properties of the plasma. It is based on calculations of the quasi-electrostatic sheath field formed at the target rear surface, which involves determination of the number of electrons and the area over which they are spread. It therefore makes use of the laser pulse power, P_L = E_L/τ_L, the laser energy absorption rate into the hot electron population, η_e, and the radius of the electron exit area on the target rear surface, *R*. Here, the maximum ion energy in the case of unlimited acceleration time is predicted to go as:

$$E_{(\max,\infty)} = Z2m_e c^2 \left(\frac{\eta P_L}{P_R}\right)^{\frac{1}{2}} \tag{3.8}$$

where $P_R = \frac{m_e c^3}{r_e}$ = 8.71 GW is the relativistic power unit and r_e is the classical electron radius. Experimentally relevant values of maximum ion energy, E_{max}, are given by incorporating a finite acceleration time, as so:

$$\frac{\tau_L}{\tau_0} = X\left(1 + \frac{1}{2}\frac{1}{1 - X^2}\right) + \frac{1}{4}\ln\left(\frac{1 + X}{1 - X}\right) \tag{3.9}$$

where a reference time, $\tau_0 = \frac{R}{v(\infty)}$, has been used to emphasize the time that the ion spends in the vicinity of the surface charge, $v(\infty)$ being the maximum possible ion velocity, and $X = \left(\frac{E_{max}}{E_{(max,\infty)}}\right)^{\frac{1}{2}}$. Under such a scheme it is predicted that an optimum laser pulse duration exists for laser driven sheath acceleration with a given laser energy.

All of the models mentioned thus far are appropriate for modelling a front of ions made up of a single ion species. An important extension to the two-temperature plasma expansion model to include the role of multiple ion species was described by Tikhonchuk *et al* [26]. The simple analytical model considers a plasma made up of two populations of ions; a mixture of heavy ions with charge Z_1, mass $A_1 m_p$ and density n_1 and light ions with charge Z_2, mass $A_2 m_p$ and density n_p, where m_p is the mass of a proton. Under the influence of the accelerating sheath field, the lighter, more mobile, ion population will become separated from the heavier ions. The light ions will accumulate at the plasma-vacuum front ahead of the heavy ion population which will reside deeper in the expanding plasma. In the regions dominated by one of the ion species, the plasma expansion dynamics are dictated by that ion species and therefore a single ion species expansion solution can be inferred, whereby the rarefaction wave is described by the relevant ion sound speed, c_{s1} or c_{s2}. However it is the transient region between these two regions where the most interesting effect takes place. The slowest of the light ion population, those in the closest vicinity to the heavy ion front, will experience a potential, φ, at time t created by the presence of the heavy ions under the influence of the hot electron temperature T_{hot}, given by:

$$e\varphi = -T_{hot}\left(1 + \frac{x}{c_{s1}t}\right) \tag{3.10}$$

where

$$c_{s1} = \left(\frac{Z_1 T_{hot}}{A_1 m_p}\right) \tag{3.11}$$

The electric field generated at this interface is stronger than the field that would be created by the light ions themselves and they therefore experience a boosted potential which enables them to reach higher energies. The bunching effect of this electrostatic shock between the two populations leads to the formation of a modulated light ion population made up of a high density, plateau-like region in the lower energy portion expanding behind an exponentially decreasing distribution of light ions made up of higher energies. The formation of spectral peaks were noted in subsequent numerical simulations carried out to investigate this effect [26] and experimental observations of quasi-monoenergetic spectral features were explained by a very similar method [27]. This effect is exploited to enhance the proton beam produced during a multiple laser pulse interaction and is explored in chapter 7.

Recent advances and refinements in the sheath model have been directed towards better representing experimental conditions. Adiabatic solutions to the Poisson equation have been given that account for two-species plasma expansion in the case of ultra-high contrast laser pulse interactions with ultra-thin targets that have a thickness comparable to the laser skin depth [28]. Solutions to the Passoni-Lontano model that include the bound electrons only and use only the hot electron beam parameters and laser energy also seem to be highly predictive [29]. An extensive comparison of a collection of theoretical approaches with experimental is presented by Perego *et al* [30]. Perego *et al* discuss the importance of evaluating the acceleration time in the various approaches and how this parameter is much longer than the laser pulse duration in the case of ultra-short (< 150 fs) pulse irradiation. The acceleration time is also a point of key discussion in examining the results presented in chapter 5.

3.2.3. Scaling of ion beam parameters with laser parameters

A myriad of studies have been carried out, both experimentally and through the use of simulation codes, in order to determine how properties of the beam scale with laser parameters. Extracting the dependence of the ion beam on the laser pulse and interaction conditions is important in order to gain control of the mechanism and ultimately deliver tailored, reproducible laser-driven ion beams. Extrapolating the scaling relations to beyond current laser capabilities also acts as a good estimate for the ion beam parameters that one can expect to achieve as laser technology advances. The maximum proton energy and conversion efficiency between laser energy and proton energy are the most common properties of the ion beams studied as these are the most relevant for use in applications (see chapter 1). Both of these parameters have been found to increase with increasing laser irradiance as $(I_L\lambda_L^2)^n$, with the value of n being highly dependent on the interaction conditions at the front surface and even varying considerably between observations.

The majority of sheath expansion models for ion acceleration have indentified the maximum ion energy, E_{pmax}, as being directly correlated to the temperature of the hot electron population, T_{hot}, effective on the rear surface. Indeed, experimental [14] [19] and numerical [31] [32] investigations of these parameters under a wide range of interaction conditions have revealed a similar scaling relation.

A number of reviews of the scaling of TNSA beams can be found in the literature. Experimental investigations of the scaling of maximum ion energy with laser intensity that have been conducted using pulses of duration from ~ 300 fs up to ~ 1ps

[33] [19] [22] have routinely found a $I_L^{0.5}$ dependence; owing in part to the dominance of ponderomotive heating of T_{hot} at relativistic laser intensities which follows a similar scaling with intensity. The interaction conditions under which these initial parameter scans were undertaken were of laser pulses in the intensity region $I_L \sim 10^{18} - 10^{20}$ W/cm^2 interacting with targets that were > 1 μm in thickness with a relatively long scale length pre-plasma on the front surface ($L_0 > \lambda_L$). 2D simulations carried out under very similar interaction conditions have also shown a $I_L^{0.5}$ dependence [32] and furthermore, predict a scaling that goes as $E_{max} \propto I_L$ for sub relativistic laser intensities interactions and significant pre-plasma formation.

For ultra-short (< 100 fs), high temporal contrast laser interactions whereby the scale length is small compared to the laser wavelength, the scaling of E_{pmax} appears to follow almost a linear relation with laser intensity in some cases [34] [35] [36]. Schnurer *et al* [35] described their observation, made with high atomic number target foils, as a result of the ionisation, and therefore hot electron density, increasing with laser intensity as well as the hot electron temperature for intensities $I_L \sim 10^{18}$–10^{19} W/cm^2. They further noted that when the ionisation rate saturates that the scaling of E_{pmax} with laser intensity resorts back to a $I_L^{\ 0.5}$ dependence. Zeil *et al* [34] used a revised version of the Schreiber model to relate the maximum proton energy to the laser power P_L; finding a linear relation between them for pulse durations less than ~ 50 fs and P_L ~ 100 TW which resorts to a square root dependence with increasing pulse duration and for higher laser power.

Many papers also examine the scaling of E_{pmax} with respect to the laser pulse duration τ_L [33] [19] [37] [38] [36]. The results of these investigations indicate that the effect of pulse duration on the TNSA mechanism is dependent on the thickness of the target foil and the contrast of the pulse. For low-medium contrast laser pulses incident on thin (< 10 μm) targets, an optimum pulse duration will apply for rear surface sheath acceleration. The optimum will depend on the interplay between a shock wave initiated at the front surface by the ASE pedestal, propagating through the target and perturbing the rear surface as it breaks out, and the duration of the main pulse. Where the shock break-out time is larger than the laser pulse duration then an increase in the duration will be beneficial, due to the accelerating field established on the rear surface existing for longer times. Consequently, for low contrast laser pulses incident on relatively thick targets [19] or in the case of ultra high-contrast pulse interactions [31], the maximum proton energy and conversion efficiency increase with τ_L. This is a result of the competing effects of an increase in absorption on the front surface during the rising edge of the pulse along with increasing acceleration time, compared with a decrease in the temperature of the hot electrons due to the decrease in laser intensity.

3.2.4. Spatial and angular characteristics of sheath acceleration

Rear surface sheath acceleration tends to lead to proton source sizes that are many times the diameter of the laser focal spot (5-10 μm, at tight focus), owing to the transverse expansion of the sheath field on the rear surface during the initial, ion-static, phase. On their first pass through the target, hot electrons travelling at, or more than, the average divergence angle will reach the rear surface at slightly later times than those travelling along the laser axis. Even though the number of hot electrons injected at wider angles is low compared to the electron density on axis, they are still able to generate a sheath field, resulting in rapid expansion along the surface. Ridgers *et al* [39] presented a detailed model and simulation study of rear surface sheath expansion that showed superluminal expansion velocities at a distance 10 μm along the surface initially, before expanding with velocity $< c$ at subsequent times due to recirculation (see chapter 2) in the case of thin foils. Measurements made on the transverse sheath expansion velocity made by Quinn *et al* [40] give 0.95c for the charge front along the rear surface and 0.4c for lateral spreading due to recirculation of hot electrons, while McKenna *et al* [9] give 0.75c for the latter.

Measurements made in the far-field of the diverging proton beam give an indication of the spatial profile of the proton source and hot electron sheath field from which they came. For example, McKenna *et al* [41] used proton beam dose profiles to diagnose the hot electron density distribution, and therefore sheath field distribution, on the rear surface of the target foil to compare the effect of target lattice structure on hot electron beam filamentation. Along with the hot electron transport between the surfaces of the target foil, the intensity distribution or shape of the laser focal spot as well as structure on the rear surface can also imprint features into the proton beam profile [42]. Using targets that have been fabricated with a well characterised periodic groove structure [43] [42] [44], microfocusing of the proton beam in each groove can be induced to generate beamlets that map onto the radiochromic film as line patterns in the dose distribution. The source size of the proton beam can be extracted by counting the number of periodic line features observed on the film.

Cowan *et al* [43] demonstrated that the source size of protons in a single beam increases with decreasing proton energy. This suggests that the highest energy protons emanate from the centre of the accelerating sheath and that the sheath field has a centrally peaked, bell-shaped distribution. Nurnberg *et al* [44] further demonstrated that the beam source size is also dependent on the type of laser system employed, ranging from ~ 50 μm for the TRIDENT (600 fs, 20 J at the time of measurement) and LULI (350 fs, 16 J at the time of measurement) systems up to > 200 μm for the Vulcan Petawatt system (1000 fs, 125 J at the time of measurement).

The quasi-static accelerating sheath field strength decays transversely, expands over time and the peak strength decreases once the maximum has been reached, leading to an envelope divergence angle that increases with decreasing proton energy [45]. An increase from ~ 2-5° up to ~ 20-30° between the maximum and minimum proton energy is typical for the half-angle beam width of a sheath accelerated proton beam. By assuming a Gaussian decrease of the peak field in time, Carroll *et al* [46] devised a model to determine the transverse sheath field shape by fitting to the divergence data. They demonstrated that the decrease in divergence angle with proton energy changes significantly with spatial shape in agreement with the findings of Brambrink *et al* [45]; with either a Gaussian distribution or inverse parabolic distribution fitting well to the experimental data, dependent on the front surface interaction conditions.

3.3. Advanced laser driven ion acceleration concepts

In search of laser-driven acceleration mechanisms that offer improved energy conversion efficiency or higher maximum ion energy compared to the conventional TNSA approach alone, there have been many studies carried out to investigate advanced forms of the TNSA mechanism including multi-pulse sheath acceleration and laser break-out afterburner. The former is of particular interest with respect to the experimental work presented in chapter 7 of this thesis and is described below.

Alternative laser-driven ion acceleration mechanisms to the TNSA mechanism have also been investigated over the last decade. These include shock acceleration and radiation pressure acceleration (RPA). Recent experimental work has been dedicated to investigating these acceleration regimes and has shown promise for exploiting these mechanisms using laser pulse conditions currently available. For completeness a brief introduction to these alternative mechanisms is also given below.

3.3.1. Advanced TNSA techniques

3.3.1.1. Multi-pulse sheath acceleration (MPSA)

A proposition to use more than one ultra-intense laser pulse during the laser-plasma interaction for the benefit of ion acceleration was first made in the numerical work of Robinson *et al* [47]. Using 1D Vlasov and PIC simulations, Robinson *et al* demonstrated that employing two, temporally resolved high intensity laser pulses resulted in an increase in the laser-to-proton energy conversion efficiency for medium energy protons (2-10 MeV) compared to when a single pulse was used.

Peaks in the proton spectra were observed in both simulations, with further investigation indicating that the enhancement was the result of a two-stage variant of the sheath acceleration mechanism detailed in the previous section. The first pulse, having a fraction of the intensity of the second, initiates sheath acceleration of ions and protons on the rear surface of the target. The acceleration of protons ahead of a front of ions leads to a density modulation in the proton population (see figure 3.2(b)), caused by the boosted potential experienced by the lower energy protons that are in the presence of the ions as described by equation 3.10. The arrival of the second pulse drives an increase in the hot electron temperature. The subsequent rise in the temperature of the sheath electrons on the rear surface greatly increases the shock associated with the heavy ion front and the resultant strong accelerating field is most effective on the lower energy, dense population of protons in its vicinity (see figure 3.2(c)). In the case of ultra-short pulses (< 100 fs) with a temporal separation of ~ 150 fs, the boosted potential experienced by the dense population of protons is observed in the proton phase space as giving rise to the generation of significant spectral peaks at the lower energy end of the spectrum.

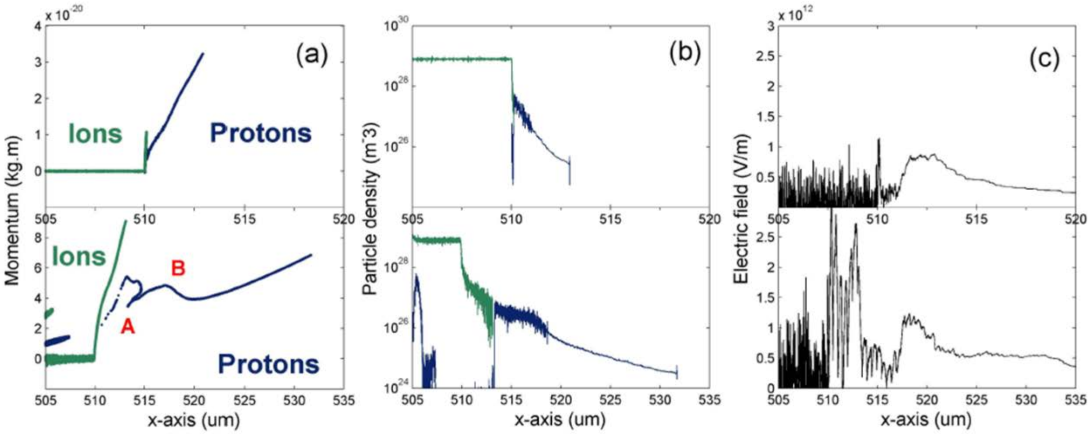

Figure 3.2 [48]: a) Ion and proton momentum phase spaces, b) particle densities and c) electric field with respect to longitudinal distance during simulations of a single pulse (top) and double pulse (bottom) laser-solid interaction. The effect on the proton population in the presence of the ion front can be seen at point A, and the subsequent interface between the low and high energy proton populations can be seen at point labelled B.

The MPSA mechanism was further explored for its potential to increase the laser-to-proton energy conversion efficiency in the experimental work presented by Markey *et al* [48]. With the Vulcan Petawatt laser in double-pulse mode (see chapter 4), two collinear laser pulses, each of 700 fs duration, were used to interact with a 100 μm thick Au foil target with temporal separation from 0.75 ps up to 2.5 ps. 1D PIC simulations were also used to model the interaction and track the resultant boost in the accelerating sheath field on the rear surface. The experimental results demonstrated that the laser-to-proton conversion efficiency increased by a factor of 3 across the entire proton spectrum when the optimum double pulse configuration (temporal separation ~ 0.75 ps) was employed. The simulations verified that the enhancement, compared to the single pulse case, was due to a boosted potential, at the interface of the two proton layers, generated by the double-pulse interaction. The simulated and measured optimum temporal separations were also in good agreement, indicating the high predictive ability of 1D PIC codes for the enhancing mechanism.

In light of the initial work carried out by Markey *et al*, the MPSA mechanism was further explored for its effect on the angular distribution of the proton beam and application with targets in which refluxing of hot electrons occurs. The results of this investigation are presented in chapter 7. The double pulse mechanism, being optically based, is a route worth pursuing for proton spectral enhancement as it does not require complex target fabrication which bodes well for high repetition employment.

3.3.1.2. Self-induced transparency and the laser break-out afterburner (BOA) technique

Numerical [49] and experimental investigations [50] have demonstrated that the maximum energy of ions generated at the rear surface of an ultra-thin target is significantly enhanced if the laser is able to fully penetrate through the entire length of the foil target. Employing an ultra-thin target (of the order 10-50 nm thick) and irradiating the front surface with a short (~ 100 fs), ultra-high contrast laser pulse at an intensity $I_L \sim 10^{21}$ W/cm^2 gives rise to a three-stage mechanism. The first stage is the standard sheath acceleration mechanism on the rear surface of the target. Recalling that the fields of a laser pulse incident on the front surface cannot propagate beyond a critical electron density (see equation 2.17 and section 2.3), initially the over-dense target is opaque to the linearly polarised laser pulse and only an evanescent component of the laser fields can penetrate into the target. The fields extend into the target over a distance defined by the skin depth of the plasma, $l_s \cong \frac{c}{\omega_p}$, where $\omega_p = \sqrt{\frac{n_e e^2}{\varepsilon_0 \gamma m_e}}$ is the plasma frequency. For solid density target foils the initial skin depth is ~ 6 nm. An increasing number of electrons expelled to the sheath regions at the surfaces of the foil during this initial phase acts to lower the effective target electron density. During the rising edge of the laser pulse, the electrons will also be heated to highly relativistic energies implying that the Lorentz factor, γ, becomes significant. These two effects result in a lowering of the effective plasma frequency and an increase in the skin depth of the laser fields; an effect known as relativistic induced transparency. The second stage is an enhanced sheath acceleration phase that occurs in response to the skin depth of the laser pulse increasing to become comparable to the thickness of the target foil. As a consequence, a significant fraction of the cold target electrons in the focal volume of the laser pulse are directly driven by the laser field and high energy conversion efficiency between laser and electrons is expected. The resultant longitudinal sheath field acting on the ions at the rear surface is much stronger as it is the combined result of thermally expanding electrons boosted directly by the ponderomotive force of the laser pulse.

The break-out afterburner phase refers to the point at which the enhanced longitudinal field is co-moving with the ion front. The dynamics of the sheath electrons in the penetrated laser field give rise to an additional ion heating mechanism. The laser fields drive the electrons that are expanding at the rear surface into a highly relativistic beam while in the presence of a non-relativistic ion front. This large relative drift acting between the electrons and the ions leads to a Buneman-like instability, which responds quickly and acts to reduce the relative drift. The phase velocity of the Buneman instability is resonant with the ions which results in efficient coupling of the laser energy to the ions.

Recent work on this technique [51] [50] has demonstrated its potential for heavy ion beam enhancement over the standard TNSA mechanism. However it requires ultra-thin foil targets, combined with an ultra-high intensity contrast laser pulse at intensities at or around 10^{20} W/cm^2, which is currently achievable, but for very few experimental groups worldwide.

3.3.2. Alternative laser acceleration mechanisms

3.3.2.1. Shock acceleration

As a result of the ponderomotive force that acts on the critical density surface of a laser-plasma interaction, a concentrated population of electrons are expelled into the bulk of the target. This charge separation at the front surface drives a flow of ions into the bulk material of the target, thus generating an ion acoustic wave. The propagation of a dense population of ions, with density n_i, mass m_i and velocity υ_i, through the bulk material of the target launches a collisionless, electrostatic ion shock in front of it, with a velocity, $\upsilon_s \sim \upsilon_i$, so determined by a balance between the pressure of the ions, P_{ions}, and the laser pressure, P_{rad}, [52]:

$$P_{ions} = n_i m_i v_i^2 = \frac{(1+R)I_L}{c} = P_{rad} \tag{3.12}$$

where R is the reflected fraction of the initial laser pulse with intensity I_L. As the shock propagates through the target, ions are reflected and accelerated in the forward direction [53] [54] [55]. The maximum energy that can be transferred to the target ions occurs for total reflection of counter streaming ions, implying that the maximum velocity under shock acceleration is given by $v_{\max} \cong 2\, v_s$ [53]. Silva *et al* used 1D and 2D simulations to investigate shock acceleration in thin (2-11 μm) targets and indicated that this mechanism becomes dominant over sheath acceleration when the ion velocity gained from the shock is greater than that gained in the sheath field on the surface. Their results predict that the threshold laser intensity for shock acceleration to become dominant in thin targets is given by a laser field parameter $a_0 \sim 16$ ($I_L \sim 3 \times 10^{20}$ W/cm^2 for Vulcan Petawatt pulses), at which point a plateau-like region in the proton energy spectrum will provide a signature of the mechanism at work.

3.3.2.2. Radiation pressure acceleration (RPA)

When an ultra-intense laser pulse is incident on an opaque target foil, a radiation pressure is exerted, as given by equation 3.12. The radiation pressure is coupled to the target foils through the strong charge separation field generated by the bulk displacement of electrons by the laser. Therefore a foil target can be accelerated simply by reflecting the laser light from the critical density surface. Furthermore, the energy conversion efficiency between a laser and a ‘light-sail’ accelerated object becomes significant if the object is moving with a relativistic velocity [56]. Esirkepov *et al* [57] demonstrated that for linearly polarised pulses with laser intensities in excess of $I_L \sim 10^{23}$ W/cm^2 incident on foils with thickness ~ λ_L, the ions are accelerated to relativistic energies within a single laser cycle. The rapid ‘laser-piston’ acceleration of the ions to relativistic velocities means that the charge separation field between the ions and the directly accelerated electrons is maintained throughout the laser irradiation. It also implies that rear surface expansion due to sheath acceleration is suppressed by the compression driven from the front surface. Thus the entire foil is propelled forward with relativistic velocity due to the radiation pressure of the laser pulse; producing a mono-energetic ion beam and achieving high energy conversion efficiency. A second regime of radiation pressure acceleration (RPA) is possible for slightly thicker targets, in which the relativistic ions accelerated at the front surface propagate into the target and emerge at the rear surface. The force accelerating the ions originates from the same charge separation described above, however the laser pulse is now pushing against the critical surface with a relatively thick region of over-dense plasma ahead of it; the so-called ‘hole-boring’ regime.

While laser intensities of $I_L \sim 10^{23}$ W/cm^2 are not yet available, radiation pressure acceleration has, however, been shown to dominate over sheath acceleration at much lower laser intensity if circular polarisation is employed [54] [58] [59]. Robinson *et al* [58] demonstrated theoretically that the threshold for RPA domination with circularly polarised pulses could be as low as $I_L \sim 10^{20} - 10^{21}$ W/cm^2. Employing circular polarisation greatly suppresses the majority of electron heating processes described in section 2.5. due to the lack of oscillating components in the Lorentz force. Consequently, the effectiveness of sheath acceleration on the rear surface is severely reduced. However, the ponderomotive force is independent of the polarisation, resulting in an electron depletion region at the critical surface of the target and radiation pressure acceleration of ions as in the linear case. As a result, the RPA mechanism dominates over the rear-surface sheath acceleration mechanism and mono-energetic features are expected to be observed in the measured spectra. In light of the spectral quality and high conversion efficiency expected from this laser acceleration technique it is currently being pursued experimentally by many groups, with initial results looking promising [60] [61].

References

1. Fenner, NC. Ion energies in the plasma produced by a high power laser. *Physics Letters*, 22, 4 (1966), 421--422.

2. Gitomer, SJ, Jones, RD, Begay, F., Ehler, AW, Kephart, JF, and Kristal, R. Fast ions and hot electrons in the laser--plasma interaction. *Physics of Fluids*, 29 (1986), 2679.

3. Crow, JE, Auer, PL, and Allen, JE. The expansion of a plasma into a vacuum. *Journal of Plasma Physics*, 14 (1975), 65--76.

4. Strickland, D. and Mourou, G. Compression of amplified chirped optical pulses. *Optics Communications*, 55, 6 (1985), 447--449.

5. Clark, EL, Krushelnick, K., Zepf, M. et al. Energetic heavy-ion and proton generation from ultraintense laser-plasma interactions with solids. *Physical review letters*, 85, 8 (2000), 1654--1657.

6. Maksimchuk, A., Gu, S., Flippo, K., Umstadter, D., and Bychenkov, V.Y. Forward ion acceleration in thin films driven by a high-intensity laser. *Physical review letters*, 84, 18 (2000), 4108--4111.

7. Snavely, RA, Key, MH, Hatchett, SP et al. Intense high-energy proton beams from petawatt-laser irradiation of solids. *Physical Review Letters*, 85, 14 (2000), 2945--2948.

8. Mora, P. Plasma expansion into a vacuum. *Physical review letters*, 90, 18 (2003), 185002.

9. McKenna, P., Carroll, DC, Clarke, RJ et al. Lateral electron transport in high-intensity laser-irradiated foils diagnosed by ion emission. *Physical review letters*,

98, 14 (2007), 145001.

10. Hegelich, M., Karsch, S., Pretzler, G. et al. MeV ion jets from short-pulse-laser interaction with thin foils. *Physical review letters*, 89, 8 (2002), 85002.

11. Sentoku, Y., Cowan, TE, Kemp, A., and Ruhl, H. High energy proton acceleration in interaction of short laser pulse with dense plasma target. *Physics of Plasmas*, 10 (2003), 2009.

12. Fuchs, J., Sentoku, Y., Karsch, S. et al. Comparison of laser ion acceleration from the front and rear surfaces of thin foils. *Physical review letters,* 94, 4 (2005), 45004.

13. Ceccotti, T., Levy, A., Popescu, H. et al. Proton acceleration with high-intensity ultrahigh-contrast laser pulses. *Physical review letters*, 99, 18 (2007), 185002.

14. Wilks, SC, Langdon, AB, Cowan, TE et al. Energetic proton generation in ultra-intense laser--solid interactions. *Physics of Plasmas*, 8 (2001), 542.

15. Gurevich, AV, Pariiskaya, LV, and Pitaevskii, LP. Self-similar motion of rarefied plasma. *Soviet Journal of Experimental and Theoretical Physics*, 22 (1966), 449.

16. Gurevich, A., Anderson, D., and Wilhelmsson, H. Ion acceleration in an expanding rarefied plasma with non-Maxwellian electrons. *Physical Review Letters,* 42, 12 (1979), 769--772.

17. Bulanov, SV, Esirkepov, T.Z., Koga, J., Tajima, T., and Farina, D. Concerning the maximum energy of ions accelerated at the front of a relativistic electron cloud expanding into vacuum. *Plasma Physics Reports*, 30, 1 (2004), 18--29.

18. Passoni, M. and Lontano, M. One-dimensional model of the electrostatic ion acceleration in the ultraintense laser-solid interaction. *Laser and Particle Beams,* 22, 2 (2004), 163--169.

19. Fuchs, J., Antici, P., d’Humieres, E. et al. Laser-driven proton scaling laws and new paths towards energy increase. *Nature Physics,* 2, 1 (2006), 48--54.

20. Mora, P. Thin-foil expansion into a vacuum. *Physical Review E*, 72, 5 (2005), 056401.

21. Passoni, M., Tikhonchuk, VT, Lontano, M., and Bychenkov, V.Y. Charge separation effects in solid targets and ion acceleration with a two-temperature electron distribution. *Physical Review E*, 69, 2 (2004), 026411.

22. Robson, L., Simpson, PT, Clarke, RJ et al. Scaling of proton acceleration driven by petawatt-laser--plasma interactions. *Nature Physics*, 3, 1 (2007), 58--62.

23. Coury, M., Carroll, DC, Robinson, APL et al. Influence of laser irradiated spot

size on energetic electron injection and proton acceleration in foil targets. *Applied Physics Letters*, 100, 7 (2012), 074105--074105.

24. Betti, S., Ceccherini, F., Cornolti, F., and Pegoraro, F. Expansion of a finite-size plasma in vacuum. *Plasma physics and controlled fusion*, 47 (2005), 521.

25. Schreiber, J., Bell, F., Grüner, F. et al. Analytical model for ion acceleration by high-intensity laser pulses. *Physical review letters*, 97, 4 (2006), 45005.

26. Tikhonchuk, VT, Andreev, AA, Bochkarev, SG, and Bychenkov, V.Y. Ion acceleration in short-laser-pulse interaction with solid foils. *Plasma physics and controlled fusion*, 47 (2005), B869.

27. Hegelich, B.M., Albright, BJ, Cobble, J. et al. Laser acceleration of quasi-monoenergetic MeV ion beams. *Nature*, 439, 7075 (2006), 441--444.

28. Andreev, A., Levy, A., Ceccotti, T., Thaury, C., Platonov, K., Loch, RA, and Martin, P. Fast-ion energy-flux enhancement from ultrathin foils irradiated by intense and high-contrast short laser pulses. *Physical review letters*, 101, 15 (2008), 155002.

29. Passoni, M. and Lontano, M. Theory of light-ion acceleration driven by a strong charge separation. *Physical review letters*, 101, 11 (2008), 115001.

30. Perego, C., Zani, A., Batani, D., and Passoni, M. Extensive comparison among Target Normal Sheath Acceleration theoretical models. *Nuclear Instruments and Methods in Physics Research Section A: Accelerators, Spectrometers, Detectors and Associated Equipment* (2011).

31. Lefebvre, E., Gremillet, L., Lévy, A. et al. Proton acceleration by moderately relativistic laser pulses interacting with solid density targets. *New Journal of Physics*, 12 (2010), 045017.

32. Sentoku, Y., Bychenkov, V.Y., Flippo, K. et al. High-energy ion generation in interaction. of short laser pulse with high-density plasma. *Applied Physics B: Lasers and Optics*, 74, 3 (2002), 207--215.

33. Borghesi, M., Fuchs, J., Bulanov, SV, Mackinnon, AJ, Patel, PK, and Roth, M. Fast ion generation by high-intensity laser irradiation of solid targets and applications. *Fusion science and technology*, 49, 3 (2006), 412--439.

34. Zeil, K., Kraft, SD, Bock, S. et al. The scaling of proton energies in ultrashort pulse laser plasma acceleration. *New Journal of Physics*, 12 (2010), 045015.

35. Schnürer, M., Andreev, AA, Steinke, S. et al. Comparison of femtosecond laser-driven proton acceleration using nanometer and micrometer thick target foils. *Laser and Particle Beams*, 29, 4 (2011), 437.

36. Passoni, M., Bertagna, L., and Zani, A. Target normal sheath acceleration: theory, comparison with experiments and future perspectives. *New Journal of Physics*, 12 (2010), 045012.

37. Carrié, M., Lefebvre, E., Flacco, A., and Malka, V. Effect of femtosecond laser pulse duration on thin-foil accelerated protons. *Nuclear Instruments and Methods in Physics Research Section A: Accelerators, Spectrometers, Detectors and Associated Equipment*, 620, 1 (2010), 36--40.

38. Oishi, Y., Nayuki, T., Fujii, T. et al. Dependence on laser intensity and pulse duration in proton acceleration by irradiation of ultrashort laser pulses on a Cu foil target. *Physics of plasmas*, 12 (2005), 073102.

39. Ridgers, CP, Sherlock, M., Evans, RG, Robinson, APL, and Kingham, RJ. Superluminal sheath-field expansion and fast-electron-beam divergence measurements in laser-solid interactions. *Physical Review E*, 83, 3 (2011), 036404.

40. Quinn, K., Wilson, PA, Cecchetti, CA et al. Laser-driven ultrafast field propagation on solid surfaces. *Physical review letters*, 102, 19 (2009), 194801.

41. McKenna, P., Robinson, APL, Neely, D. et al. Effect of Lattice Structure on Energetic Electron Transport in Solids Irradiated by Ultraintense Laser Pulses. *Physical Review Letters*, 106, 18 (2011), 185004.

42. Roth, M., Brambrink, E., Audebert, P. et al. Laser accelerated ions and electron transport in ultra-intense laser matter interaction. *Laser and Particle Beams*, 23, 1 (2005), 95--100.

43. Cowan, TE, Fuchs, J., Ruhl, H. et al. Ultralow emittance, multi-MeV proton beams from a laser virtual-cathode plasma accelerator. *Physical review letters*, 92, 20 (2004), 204801.

44. Nürnberg, F., Schollmeier, M., Brambrink, E. et al. Radiochromic film imaging spectroscopy of laser-accelerated proton beams. *Review of scientific instruments*, 80 (2009), 033301.

45. Brambrink, E., Schreiber, J., Schlegel, T. et al. Transverse characteristics of short-pulse laser-produced ion beams: a study of the acceleration dynamics. *Physical review letters*, 96, 15 (2006), 154801.

46. Carroll, DC, McKenna, P., Lundh, O. et al. Active manipulation of the spatial energy distribution of laser-accelerated proton beams. *Physical Review E*, 76, 6 (2007), 065401.

47. Robinson, APL, Neely, D., McKenna, P., and Evans, RG. Spectral control in proton acceleration with multiple laser pulses. *Plasma Physics and Controlled*

Fusion, 49 (2007), 373.

48. Markey, K., McKenna, P., Brenner, CM et al. Spectral Enhancement in the Double Pulse Regime of Laser Proton Acceleration. *Physical review letters*, 105, 19 (2010), 195008.

49. Yin, L., Albright, BJ, Hegelich, BM, and Fernández, JC. GeV laser ion acceleration from ultrathin targets: The laser break-out afterburner. *Laser and Particle Beams*, 24, 02 (2006), 291--298.

50. Henig, A., Kiefer, D., Markey, K. et al. Enhanced laser-driven ion acceleration in the relativistic transparency regime. *Physical review letters*, 103, 4 (2009), 45002.

51. Yin, L., Albright, BJ, Bowers, KJ, Jung, D., Fernández, JC, and Hegelich, BM. Three-Dimensional Dynamics of Breakout Afterburner Ion Acceleration Using High-Contrast Short-Pulse Laser and Nanoscale Targets. *Physical Review Letters*, 107, 4 (2011), 45003.

52. Wilks, SC, Kruer, WL, Tabak, M., and Langdon, AB. Absorption of ultra-intense laser pulses. *Physical review letters*, 69, 9 (1992), 1383--1386.

53. Silva, L.O., Marti, M., Davies, J.R., Fonseca, R.A., Ren, C., Tsung, F.S., and Mori, W.B. Proton shock acceleration in laser-plasma interactions. *Physical review letters*, 92, 1 (2004), 15002.

54. Macchi, A., Cattani, F., Liseykina, T.V., and Cornolti, F. Laser acceleration of ion bunches at the front surface of overdense plasmas. *Physical review letters*, 94, 16 (2005), 165003.

55. Chen, M., Sheng, Z.M., Dong, Q.L., He, M.Q., Li, Y.T., Bari, M.A., and Zhang, J. Collisionless electrostatic shock generation and ion acceleration by ultraintense laser pulses in overdense plasmas. *Physics of plasmas*, 14 (2007), 053102.

56. Marx, G. Interstellar vehicle propelled by terrestrial laser beam. *Nature*, 211 (1966).

57. Esirkepov, T., Borghesi, M., Bulanov, SV, Mourou, G., and Tajima, T. Highly efficient relativistic-ion generation in the laser-piston regime. *Physical review letters*, 92, 17 (2004), 175003.

58. Robinson, APL, Zepf, M., Kar, S., Evans, RG, and Bellei, C. Radiation pressure acceleration of thin foils with circularly polarized laser pulses. *New Journal of Physics*, 10 (2008), 013021.

59. Qiao, B., Zepf, M., Borghesi, M., and Geissler, M. Stable GeV ion-beam acceleration from thin foils by circularly polarized laser pulses. *Physical review letters*, 102, 14 (2009), 145002.

60. Henig, A., Steinke, S., Schnürer, M. et al. Radiation-pressure acceleration of ion beams driven by circularly polarized laser pulses. *Physical review letters*, 103, 24 (2009), 245003.

61. Palmer, C.A.J., Dover, NP, Pogorelsky, I. et al. Monoenergetic proton beams accelerated by a radiation pressure driven shock. *Physical Review Letters*, 106, 1 (2011), 14801.

Chapter 4: Methods

Multi-MeV laser-driven proton acceleration is a relatively new experimental field of research, with the detection of bright, high quality, MeV proton beams first occurring as recently as the beginning of the last decade. However the methods utilised for laser-plasma production and subsequent diagnosis are generally well established, as experimental research in this field has been carried out since the 1970's. The methodology behind the acquisition of the data presented in this thesis is reviewed in this chapter. A description of the laser systems that were used is also given, along with a discussion of the role of laser pulse contrast and of the methods employed to improve it.

4.1 Introduction to high power laser systems and the CPA technique

In 2010, we celebrated 50 years of the laser. At the time of the first lasers being built, it was considered to be a solution looking for a problem. As physicists began to realise the great potential of the laser for plasma-based research, the demand for ever increasing laser intensity out-stretched the laser technology. Initially, progress in laser development was rapid, with the use of new lasing materials that gave improved gain characteristics and optics with higher damage thresholds that enabled ever increasing laser energy and fluencies to be achieved. Pulsed lasers were achieved with the introduction of the concept of Q-switching [1], which led the way to the development of high power laser systems. However, progress then slowed down significantly in the 1970’s as the laser systems reached the upper limits of optical damage thresholds and, more importantly, the saturation fluence for the amplifying mediums. At the time, a common method adopted to overcome the intensity limit was to increase the beam diameter. However, the cost of a series of large aperture optics soon stopped this from becoming a viable solution. Thus, the laser systems were restricted to an intensity of around 10^{16} W/cm^{2}$_{,}$ deliverable in pulses of kilojoule energy and nanosecond duration.

It was not until the 1980’s that the intensity barrier obstacle was overcome with the development of the chirped pulse amplification (CPA) technique which was first introduced by D. Strickland and G. Mourou in 1985 [2]. Using this technique, the pulse is stretched in time, in order to decrease the intensity of the pulse to below the damage threshold of the optical media in the laser chain. Therefore, one can achieve the highest laser energy possible from the amplification stages, before compressing the pulse in the final stages and thus delivering a short (< ps), ultra-intense laser pulse. The pulse is temporally stretched by taking advantage of its finite bandwidth. Before it reaches the amplification stages, a diffraction grating system can be used to impart a positive frequency chirp on the pulse; meaning that the separate frequency components of the pulse traverse different path lengths so that pulse becomes longer with the longer wavelengths preceding the shorter ones. A negative chirp is then induced into the pulse after amplification using a compressor system, usually made up of similar gratings as the stretcher, to re-compress the pulse to a duration of the same order as the seed pulse.

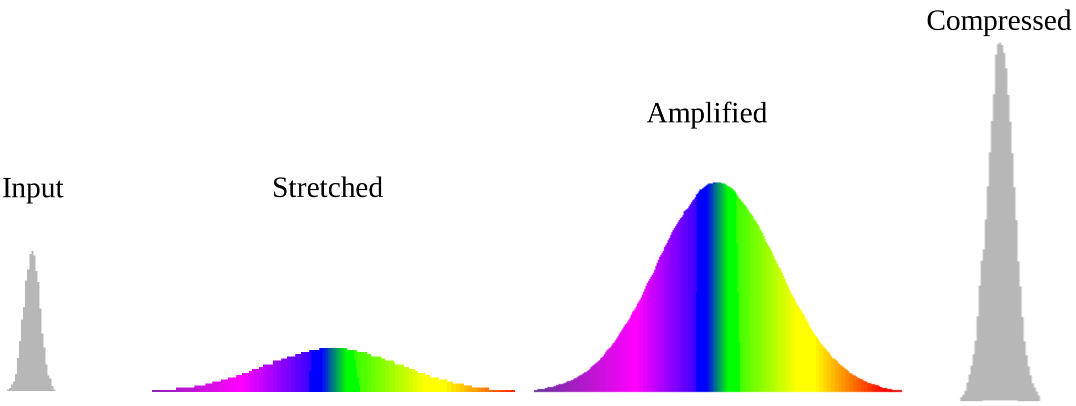

Figure 4.1 Schematic of the CPA technique.

However, complete recompression using the CPA technique alone is rarely achieved, particularly in high-gain systems, due to bandwidth narrowing [3] during the amplifying stages which thus limits the minimum pulse duration obtainable. In order to deliberately enhance the frequency bandwidth of the pre-amplified pulse and therefore obtain sub picosecond pulses from a high-gain laser system after recompression, a method called optical parametric amplification (OPA) [4] [5] can be adopted in conjunction with the CPA technique (often referred to as an OPCPA system). In this scheme the stretched pulses are first sent through an optical parametric amplifier which acts to transfer energy from a pump pulse to the seed pulse in a non-linear optical crystal, which gives rise to broad frequency bandwidth, high gain amplification. A broad bandwidth pulse can then be sent through to the main amplification stages which means that even with the effect of gain narrowing, the pulse still has a large enough bandwidth so that it can compressed effectively to an ultra-short (< 1ps) length.

4.2 Laser systems used

The Rutherford Appleton Laboratory’s Central Laser Facility (CLF) in Oxfordshire is host to a number of laser systems that provide the research community with world-class facilities for laser-plasma experimental campaigns. All three of the campaigns discussed in the experimental chapters of this thesis were conducted at the CLF; the first of which using the Astra laser and the following two using the Vulcan Petawatt laser. Like most high-power laser systems, both Astra and Vulcan are built on a Master Oscillator – Power Amplifier architecture. Another feature common to both is that they have been designed using a solid-state crystal as the lasing medium. However, here is where their similarity ends. Here follows a detailed description of the laser system components and specifications.

4.2.1 Astra laser

The Astra laser pulse is seeded using a nJ, 12 fs Titanium:Sapphire (TiS) oscillator and pre-amplifier system which provides 1 mJ, 7 ps, 800 nm pulses at 1 kHz. An ultrafast Pockels Cells is then used by means of a pulse picker to select pulses at a repetition rate of 10 Hz as an input to Astra's 3-stage, Nd:YAG pumped amplification process. Utilising the CPA technique, the pulses are stretched to 0.5 ns and then sent to the first amplification stage in which the pulse energy increases to 5 mJ using a three-pass Ti:S crystal amplifier pumped by a 100 mJ source. The second stage then increases the energy to 200 mJ using a four-pass Ti:S amplifier pumped by a 600 mJ source. The final amplification stage generates pulses containing 1.5 J of energy using a four-pass Ti:S amplifier pumped by a 4 J source. The pulse repetition rate required for delivery to the target area is then selected using a beam-switching mirror. The 0.5 ns laser pulse is increased in diameter to 60 mm in order to protect the final gratings and optics before being compressed down to 40 fs using a grating compressor, achieving maximum laser energy on to the target of approximately 650 mJ. Using an F/2.5 off-axis focussing parabola, the laser pulse is then focused to a minimum spot size of 4 x 6 μm^2, yielding a maximum laser intensity of approximately 2 x 10^{19} W/cm^2.

After the last two amplification stages, a vacuum spatial filter (VSF) is used to improve the beam profile by removing any spatial modulations in the beam distribution. The energy delivered on to the target can be controlled remotely using a half-wave plate in series with 2 polarizing plates.

4.2.2 Vulcan Petawatt laser

The Vulcan laser system is a Nd:glass based system that provides pulses to two target areas; Target Area West (TAW) and Target Area Petawatt (TAP). The data presented in this PhD thesis has been obtained from two experimental campaigns conducted using the TAP arm of the Vulcan laser and so a description of the TAP laser pulse only is included here. The Vulcan Petawatt beam line can deliver a peak laser intensity of 10^{21} W/cm^2 [6]. It features the aforementioned OPA system along with mixed-glass rod and disk amplifying stages under the CPA technique. Since its first opening, the front end of the TAP beamline has also further been upgraded to accommodate a picosecond OPCPA system at the front end of the laser chain. One of the two experimental campaigns mentioned in chapter 7 took place before this most recent upgrade and so it is necessary to describe the Petawatt system as it was during the first campaign and then describe the change that was brought about by the upgrade.

Seed pulses of duration 120 fs are provided by a 5 nJ, 1055 nm, Ti:S oscillator, which are then fed into a nanosecond stretcher comprising of a large area, 1480 lines/mm gold holographic grating. Two passes through this stretcher are sufficient to increase the pulse length to 4.8 ns in preparation for the amplification stages. Pre-amplification using OPA is necessary so as to ensure a bandwidth of more than 4 nm is maintained after full amplification, as this is the minimum bandwidth required in order to achieve the baseline pulse duration specification of 500 fs [7]. The pump pulse for the OPA is provided in the form of frequency-doubled, 200-300 mJ, 4.5 ns, 10 Hz pulses from a 1053 nm Nd:YAG laser. This pulse is used to pump a three-stage OPA system [7] which amplifies the stretched seed pulse over a gain of 10^7 as it passes through β-Barium Borate (BBO) crystals that are maintained in an oven at 40°.

The main amplification chain (see figure 4.2) is comprised of a series of Nd:Phosphate and Nd:Silicate rod and disk amplifiers that together deliver a high gain of 450, thus increasing the pulse to ~ 85 J. As the pulse passes through this amplification system, the diameter of the beam steadily increases from 9 mm, at its first pass through the first Nd:Silicate rod amplifier, up to 150 mm as it emerges from the final disk amplifier in this chain. In order to correct for wave front errors introduced during the optical chain and therefore improve the wave front quality for compression and focussing, the TAP beamline also makes use of a 120 mm deformable mirror in the form of an adaptive optics (AO) module [8]. This is positioned between the rod and disk amplifiers and works by correcting slowly varying aberrations with 64 individual elements in a 2D array. The mirror responds to a feedback loop mechanism that stems from wave front measurements made at the end of the final amplification stage.

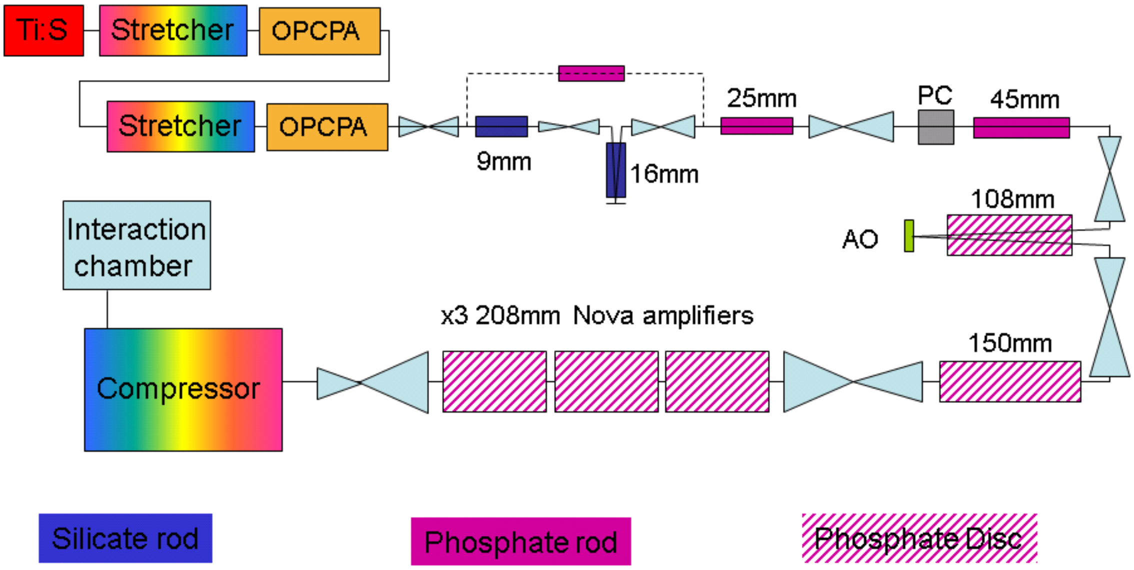

Figure 4.2 Schematic representation of the TAP beamline which is capable of delivering 450 J laser pulses in ~ 700 fs (figure provided by the CLF).

To further amplify the pulse to an energy of ~ 650 J, a series of 208 mm aperture, flash-lamp pumped disk amplifiers are then used for the final amplification stage. The beam is then expanded to a diameter of 600 mm using a VSF over a distance of 19 m, before being compressed down to approximately 700 fs duration using 1480 lines/mm, gold-coated holographic gratings of diameter 940 mm. A laser pulse containing ~ 450 J is then delivered into the target chamber whereby a 620 mm diameter, F/3 off-axis parabola is employed to focus the beam down to a minimum diameter of ~ 5 μm, yielding a maximum laser intensity on to the target of almost 10^{21} W/cm^2.

In 2010, the Vulcan Petawatt system was upgraded with the introduction of a picosecond optical parametric preamplifier [9] as an addition to the existing nanosecond OPA. The initial seed pulses from the Ti:S oscillator are first split into two, with one part of the pulse train being stretched to 3 ps using a 1500 lines/mm grating. The remainder of the pulse is amplified to 500 μJ by passing it through a regenerative amplifier in which gain narrowing causes the optical bandwidth to decrease and thus the pulse duration to lengthen to ~ 15 ps. The output of this regenerative amplifier is then frequency doubled to 527 nm and is used to pump the ps OPA which acts to amplify the 3 ps pulses up to 70 μJ using the same BBO medium as used for the nanosecond OPA. These higher energy seed pulses are then injected into the ns stretcher and pass through a reduced, two-stage ns OPA system, after which the system proceeds as described above. The implementation of a picosecond OPA system was necessary in order to improve the amplified spontaneous emission intensity contrast which is discussed in the next section.

4.2.3. Vulcan Petawatt laser in double-pulse mode

As part of the experimental study described in chapter 7 the Vulcan Petawatt laser was modified during the campaign so as to deliver two, ultra intense laser pulses on to the target per shot [10]. The pulses were requested to follow the same beam path and overlap in the spatial dimension but be separated temporally on the order of picoseconds. This was achieved with the introduction of an optical system, consisting of half-wave plates, beam splitter, translation stage and polarizing beam cube, into the laser chain between the picosecond and the nanosecond stretchers (see figure 4.2). The orientation between the half-wave plate and the beam splitter was used to control the intensity ratio between the first and second pulse. Both pulses were then retro-reflected using roof prisms, with one of these mounted on a translation stage in order to introduce a controllable, temporal delay into the double pulse structure. The polarisations of the pulses were then matched before being brought onto the same alignment using a non-polarising cube. By sending the 150 fs pulses from the seed oscillator through the system and observing the interference fringes that formed when the two test pulses were tilted and then overlapped in space and time, the nominal zero delay position between the two pulses was established to within 50 fs.

4.3 Amplified Spontaneous Emission (ASE) and laser contrast ratio

An intrinsic weakness of high power laser systems is in the production of a pedestal on which the main pulse is superimposed and of pre-pulses that precede it (see figure 4.3). This is due to the presence of spontaneous emission in the laser system which is then subsequently amplified, known as amplified spontaneous emission (ASE), as well as parts of the main pulse that are not fully re-compressed, leading to uncompensated dispersion. Analogous to ASE, the OPA technique also produces an unwanted background in the form of parametric fluorescence. Consequently, the rising edge of the laser pulse can have unwanted pulse energy on timescales of up to nanoseconds before the peak of the pulse.

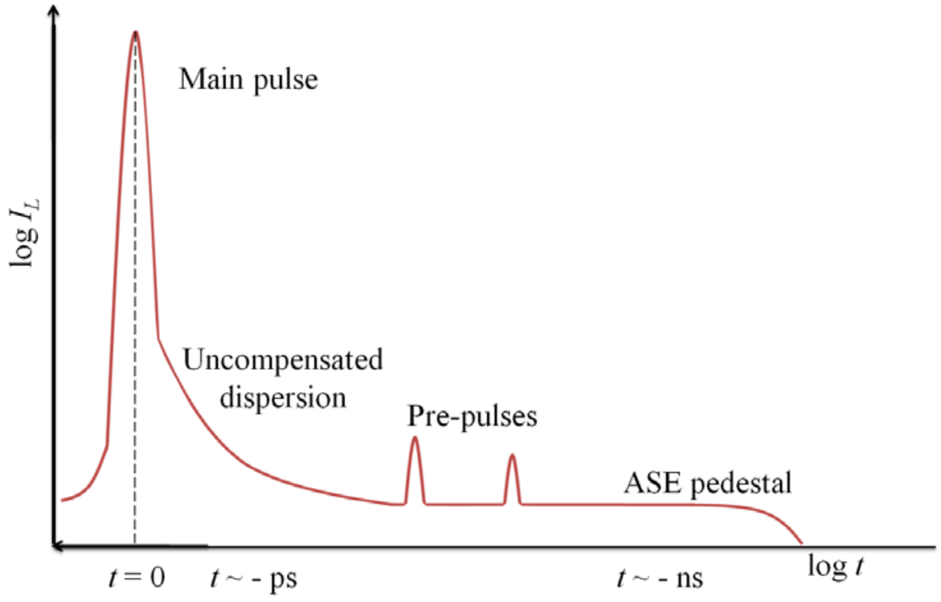

Figure 4.3: Schematic illustration of the temporal intensity profile of a typical laser pulse before contrast improvement.

The laser pulse contrast is defined as the ratio between the intensity of the peak of the pulse and of the pedestal or pre-pulses that precede it. The intensity contrast of a given laser pulse is an important factor in determining the conditions under which the laser-plasma interaction occurs at the front surface of a target. A poor intensity contrast can lead to significant pre-heating and therefore pre-plasma expansion, which gives rise to a large coronal plasma profile, or induces a significant shock-wave travelling into the target which can perturb the rear surface prior to the main pulse interaction. Therefore, it is important that the laser contrast is fully characterised and maximised, in most instances, before the laser pulse is employed. To this aim, it is common to state the contrast of a laser system at nanoseconds as well as picoseconds prior to the arrival of the peak.

At the time of the experiment, the contrast of the Astra laser system was given as 2×10^6 several picoseconds [11] before the peak of the pulse. Before the introduction of the picosecond OPA on the TAP beamline, it was shown that an ASE pedestal with a contrast of $4 \text{ x } 10^8$ arrived ~2 ns before the peak of the pulse and that the picosecond contrast was 10^6 at ~ 60 ps ahead of the peak [12]. During the September 2010 campaign using the TAP laser pulse, the ASE contrast was measured as having improved by at least two orders of magnitude following the introduction of the picosecond OPA system. This resulted in the achievement of a laser contrast of 10^{10} at 1ns and 10^8 at 100 ps before the peak of the pulse [9]. The parametric fluorescence caused by the picosecond OPA was also measured as starting ~ 15 ps before the peak pulse interaction.

4.3.1. Improving the intensity contrast of a laser pulse

The ways in which the temporal intensity contrast of the laser pulse can be improved can be divided into two subgroups: those that are implemented within the laser chain and those that are introduced at the end of the laser chain within the target interaction chamber itself. Examples of laser chain methods include the use of optical parametric amplification [12], energetic high contrast oscillator seed pulses [13] and the use of ultra-fast gating techniques [11]. Newer techniques, such as cross-polarised wave generation (XPW) [14], also offer another very promising solution to producing temporally clean laser pulses for picosecond and femtosecond laser systems.

A particularly effective and popular experimental method for enhancing the laser contrast involves the implementation of a plasma mirror into the beam path a short distance from the target. A plasma mirror system is normally comprised of an anti-reflection coated, optically flat dielectric substrate that is placed in the beam path at a certain distance from a focussing parabola so that it is irradiated away from the point focus of the beam (see figure 4.4).

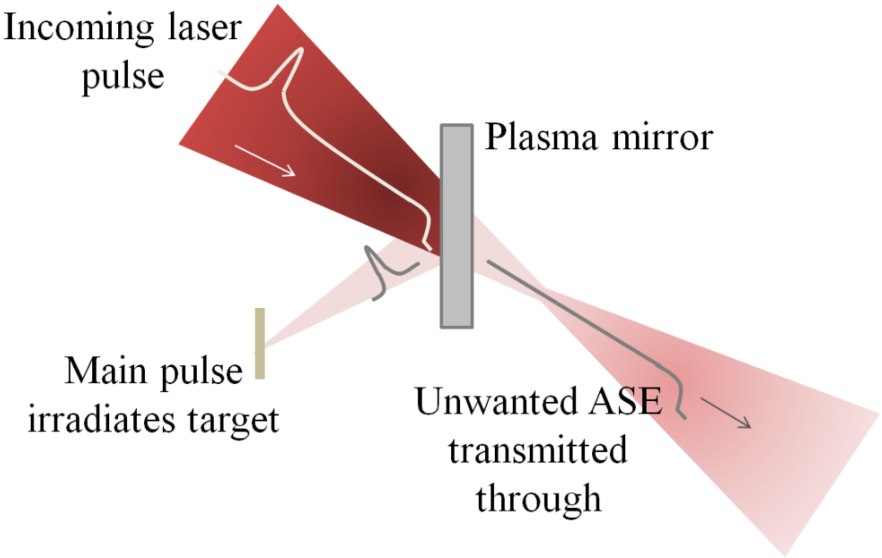

Figure 4.4: Schematic illustration of plasma mirror implemented into the laser beam path.

If the plasma mirror is placed so that it is effectively irradiated with a peak laser intensity of approximately 10^{15} W/cm^2, the intensity of the ASE pedestal and of any pre-pulses on the plasma mirror will be below the plasma formation threshold of ~ 10^{11}-10^{13} W/cm^2 [15]. This will result in the unwanted parts of the laser pulse (and thus a fraction of the laser energy) passing through the glass substrate and leaving the beam path. Aligning the plasma mirror at the Brewster angle to the incoming beam and using anti-reflection coatings are sufficient to ensure that reflection prior to the main pulse arriving is minimised. As soon as the intensity of the laser pulse is high enough to ionize the surface of the plasma mirror, a layer of over-dense plasma quickly forms which will act to reflect the remaining part of the laser pulse towards the target. Therefore, the plasma mirror will effectively ‘switch on’ during the rising edge of the main pulse. The glass substrate acts like a self-induced plasma shutter by gating out the low level intensity pedestal and pre-pulses and is capable of delivering two orders of magnitude improvement to the laser contrast [15] at the expense of slightly reduced laser energy delivered onto the target.

A single or even double plasma mirror system is commonplace within laser-plasma mirror experiments where ultra-high contrast is required. Their effect on the focusability of the beam and the quality of the laser pulse delivered on to the target has been well characterised [16] [17]. A critical parameter in determining the performance of the plasma mirror is the time between initial plasma formation and the main peak arriving. Significant expansion on the plasma mirror prior to the peak of the interacting can lead to wavefront distortions and a poor focal spot intensity distribution. It has been found that modulations on the plasma mirror surface are small compared to the laser wavelength when the plasma expansion timescale is less than ~ 2.5 ps [17]. Therefore, ionisation of the plasma mirror surface (switch-on) ideally needs to begin no more than 2 ps before the peak intensity of the pulse arrives.

4.4. Experiment diagnostics

Given the variety of radiation given off during a laser-plasma interaction, it is possible to describe the most commonly used laser-plasma diagnostics as belonging to one of three subgroups: energy resolving, spatial intensity profiling or photon/optically based. The diagnostics that were used to obtain the experimental data presented in the subsequent chapters are a good example of those typically used during laser-driven ion acceleration experimental campaigns. Here follows a description of the methodology of the diagnostic equipment used including a description of the type of detector employed and data extraction method.

4.4.1. Radiochromic film (RCF) proton detector stacks

Radiochromic film (RCF) is a widely used ionising radiation detector that is specifically produced for the purpose of radiation dosimetry. The film consists of a thin active layer, which is sensitive to ionising radiation, sandwiched between layers of clear plastic that act as the film's holder. RCF of type Gafchromic® HD-810, which has the composition shown in figure 4.5 below, was used to obtain the experimental data presented in this thesis.

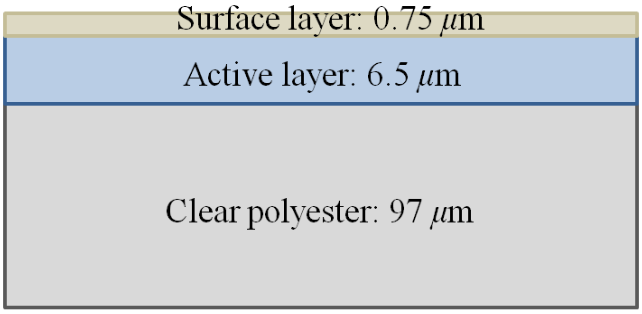

Figure 4.5: Layer composition of RCF type Gafchromic® HD-810 used in the experimental work presented in later chapters.

The active dosimetry layer is made up of an organic dye, polydiacetylene monomeric dispersion, which undergoes a polymerisation process when exposed to ionising radiation in the form of photons or energetic particles. The self-developing dye changes from colourless to blue as a consequence of the polymerisation process, turning a darker blue with increasing radiation dose, and continues to do so under continued exposure until the film is saturated. The optical density of the film is therefore a measure of the radiation dose that the film has been exposed to. The majority of the polymerisation takes place in the first few milliseconds after exposure, however the manufacturer has characterised the optical density as approaching a constant value about 48 hours after exposure. Newly exposed films are therefore sealed in light-tight containers for two days before the signal is digitised.

An RCF stack proton detector exploits the characteristic shape of the energy deposition curve of a proton in matter; the so-called Bragg peak curve. Quite unlike the deposition curves of photons and electrons which exhibit a peak usually within a small distance after they pass through the vacuum-solid interface, ions deposit the majority of their energy within a localised region at the end of their range. This forms a well defined peak at the end of the deposition curve; the depth of which is dependent on the composition of the medium that the ion is passing through and the energy and charge state of the ion. Bragg peak curves can be computed using the SRIM (stopping ranges of ions in matter) software package [18], which employs a Monte Carlo simulation of ion energy loss in matter. An example collection of Bragg peak curves for protons of various energies passing through a plastic target is shown below (see figure 4.6).

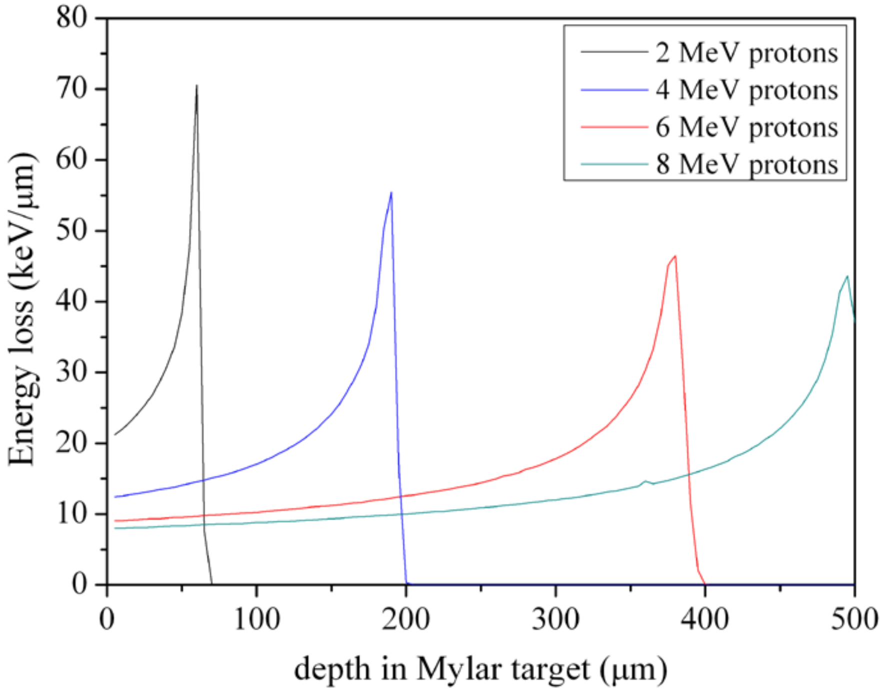

Figure 4.6: Proton energy deposition curves in solid Mylar for protons of various initial energies.

When layers of RCF are stacked together a proton beam passing through leaves behind a spectral footprint through the depth of the detector, as it deposits energy in the active layers, whereby lower energies are stopped at the beginning of the stack and higher energies penetrate through and are stopped at the rear of the stack. Due to the Bragg peak nature of the energy deposition, the thin active layers that are located at various depths within the stack will record a signal of which the majority of the dose deposited belongs to a relatively narrow range of proton energies whose Bragg peak coincides with the position of the active medium in the RCF layer. Further still, the typical exponentially decreasing spectrum of the sheath accelerated protons measured here means that a relatively small amount of the signal detected in a given RCF layer will come from protons of higher energy.

The energy resolution of the detector stack is determined by the thickness of material between the active layers and therefore the highest resolution possible would be achieved by using a stack consisting of RCF layers only. However, due to the ever increasing expense of the film it is common to interweave the RCF layers with layers of sub-millimeter thick Mylar or iron, for example, in order to increase the maximum detectable proton energy of the diagnostic. The front of the stack is made up of thin (13 μm thick) layers of aluminium foil in order to protect the first RCF layer from debris and stray laser light from the laser-plasma interaction. The aluminium foil is also capable of stopping the majority of ions heavier than protons so as to ensure that the signal recorded is primarily due to protons only. For example, 26 μm of aluminium will stop up to 28 MeV carbon ions and up to 40 MeV oxygen ions.

4.4.1.1. Proton beam dose extraction from RCF stacks

After the RCF stack has been exposed to a laser accelerated proton beam, the film is left to rest in a cool, light-tight container for approximately 48 hours to allow it to fully develop. The films are then digitised with the use of a high resolution optical scanner equipped with red, green and blue light emitting diodes. Each pixel of the scanned image is therefore a transmission measurement of the corresponding element of the film, for each of the three colour channels (Red, Green and Blue, RGB) of the scanner. The transmission signal recorded by the RGB colour channels of the scanner can be converted to a relative optical density (OD) using the numerical value of the image pixel, $signal_{RGB}$, and equation 4.1:

$$OD_{R,G,B} = \log\left(\frac{signal_{max}}{signal_{RGB}}\right) \tag{4.1}$$

where $signal_{max}$ is 255 for an 8-bit scanner and 65535 for a 16-bit scanner. In order to extract a dose signal, measured in Grays (Gy=J/kg), from the scanned images an absolute calibration between the OD recorded by the scanner in each colour channel and films exposed to a known dose must first be performed. This process needs to be done for every scanner that is employed for this purpose, unless cross-calibration between different scanners is possible. For the experimental work involving RCF stacks presented in this thesis, a Nikon Super Cool Scan 9000 ED was calibrated [19] with HD-810 film pieces that had been exposed to a range of doses using the monoenergetic proton beams provided by the University of Birmingham's cyclotron accelerator.

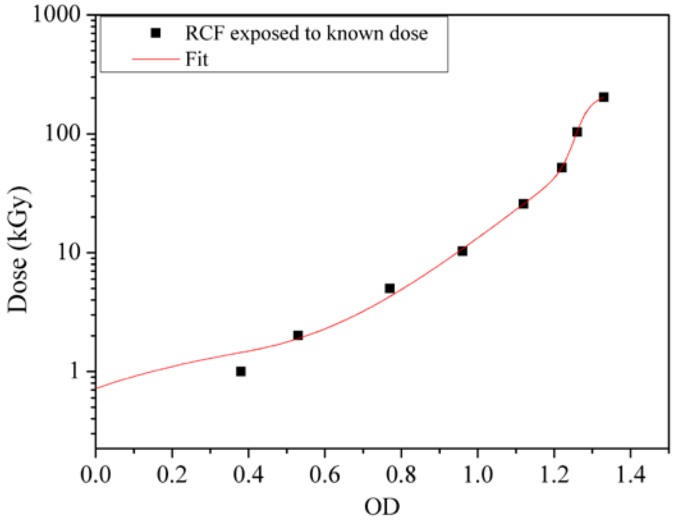

Figure 4.7: OD-dose calibration of RCF of type HD 810 for ultra-high dose levels conducted using a UV light source

Calibrating the RCF dose using the RGB channel method, rather than using a simple greyscale, is better suited for recording the high particle flux of a laser accelerated proton beam as it enables an order of magnitude increase in the dynamic range of the detectable dose. The relative difference in the sensitivity of the different wavelengths to absorption through the developed film means that there exists a separate OD-to-dose calibration curve for each of the colour channels. The red channel is the most reliable channel to use for low dose down to 0.5 Gy, whereas the blue channel is better suited for recording high doses as it has a saturation dose of ~ 30 kGy, see [19] and references therein. For proton dose in excess of 30 kGy, Scott *et al* [19] have also shown that UV wavelength light sources can be used to extend the dynamic range of the extraction technique up to ~ 200 kGy (see figure 4.7).

Figure 4.8: Example image of RCF exposed to a proton beam (left) and the corresponding dose map (right) of the image after conversion and background subtraction (colour scale chosen so that full range of dose can be seen).

Once the calibration curves are formulated, the OD signal from each pixel in the image can be converted to dose. A MATLAB routine modified by the author was used to convert from OD to dose for each colour channel. Dose signal in regions of the film that had been exposed to the background radiation only, signified by the uniform light-blue region outside of the proton beam profile, was subtracted from each pixel of the dose profile map. This enables the user to convert the scanned image of the film piece into a spatially resolved proton dose map across the footprint of the beam, see figure 4.7. The dose recorded by each pixel represents the amount of energy deposited in that element of the active layer of the film divided by the mass of the element. The total energy deposited across the whole beam area in the active layer of the RCF piece is therefore recoverable by summing over each of the N pixels:

$$E_{dep} = \rho_{RCF}\, d_{RCF} \sum_{i=1}^{N} D_i\, A_i \tag{4.2}$$

where ρ_{RCF} and d_{RCF} are the density and thickness of the active layer, respectively, and D_i and A_i are the proton dose and pixel area of the ith pixel, respectively.

4.4.1.2. Proton beam analysis using RCF stacks

Deconvolving the proton spectrum from the RCF measurements

Stacks of dosimetry film record the proton dose deposited in the active layers of each film. An intitial estimate of the proton beam dose spectrum can be extracted by plotting the dose deposited in each layer as a function of the proton energy whose Bragg peak lies within the thin active layer. However, best practice for extracting a proton beam spectrum from a RCF stack is conducted by accounting for the contribution of all protons, with energy up to the maximum proton energy E_{pmax}, to the total dose recorded as they pass through the stack layers. For each active layer in the stack, the energy deposited as a function of proton energy, E_{dep} (E_p), for all proton energies that pass through can be formulated using the Bragg peak curves generated by the SRIM Monte Carlo simulation code. Combining E_{dep} (E_p) with the number density function of the proton beam, $\frac{dN(E_p)}{dE_p}$, and integrating from the minimum proton energy that deposits energy into the active layer E_{min} up to the maximum proton energy of the beam, equates to the total energy deposited, E_{dep}, in the active layer of the RCF piece.

$$E_{dep} = \int_{E_{\min}}^{E_{max}} \frac{dN(E_p)}{dE_p} \,.\, E_{dep}(E_p)\, dE_p \tag{4.3}$$

For each active layer in the RCF stack, the integral in equation 4.3 must equal the experimentally measured value of total energy deposited as given by equation 4.2. To obtain the proton energy spectra for the entire proton beam recorded by the RCF stack also requires equation 4.3 for every layer to be solved simultaneously. This can be done using an iterative algorithm and by assuming that the exponentially decreasing proton number density function of a laser-driven sheath accelerated proton beam follows a Maxwell-Boltzmann distribution:

$$\frac{dN}{dE_p} = -\frac{N_0}{k_B T_p} \exp\left(-\frac{E_p}{k_B T_p}\right) \tag{4.4}$$

An efficient PV-WAVE code written by S. Kar and P. T. Simpson was used to carry out the deconvolution described above to extract the proton spectra recorded by the RCF stacks used in chapter 7. The code begins with the last layer, the *n*th layer, in the stack that has recorded signal. E_{pmax} is estimated to be between the nominal energy of the *n*th layer and the (n + 1)th layer and a proton number representing the noise floor of the film is assigned to this proton energy. Keeping this point fixed, the code varies the temperature of the proton number distribution function until the integral value of E_{dep} is within 5 % of the measured value of E_{dep} for the *n*th layer. The (n – 1)th layer is then considered by iteratively generating the proton spectrum between the minimum energy that deposits energy in the (n – 1)th layer and minimum energy that deposits energy in the *n*th layer. Having already defined the spectrum between the nominal energies of the *n*th and (n + 1)th layer in the previous cycle of the code, the energy deposited in the *n*th layer is included as a constant in the iteration for the (n – 1)th layer. When the process is complete, the output of the code is the proton energy spectra as a function of the proton energy, $\frac{dN(E_p)}{dE_p}$.

Beam divergence and angular distribution of proton dose

Not only do RCF stacks enable one to extract the proton energy spectrum, they also provide the angular distribution of the proton beam at a given distance from the source. Further still, the beam divergence angle as a function of the nominal proton energy of the active layer can be easily extracted by calculating the half-cone angle subtended at the outer radius of the approximately circular beam. In most cases, an RCF stack is positioned close enough to the target so that it samples the entire solid angle subtended by the proton beam. For example, the RCF stack employed to record the forward propagating proton beams generated in the experimental campaign presented in chapter 7 was positioned 40 ± 1 mm from the rear surface of the target. A proton beam intensity profile for the energy bin sampled by the active layer of an RCF piece can be quickly extracted with high spatial resolution using the dose map of a converted scanned image of the film.

4.4.2. Thomson parabola ion spectrometer

Another popular diagnostic among laser driven ion acceleration experiments is the Thomson parabola (TP) ion spectrometer. This diagnostic samples a very small fraction of the accelerated beam and separates the ions according to their charge-to-mass ratio and their energy. It thus provides signal that can be used to extract high resolution energy spectra for all ion species present, simultaneously in a single shot. It is therefore a complementary addition to the information that the RCF stacks deliver and the two are commonly used together in an experimental campaign if target chamber space allows.

The ions are sampled through a lead pinhole at the front of the spectrometer and enter a region of electric and magnetic fields provided by a pair of electrode plates and a pair of permanent magnets, respectively. The diameter of the pinhole is dependent on the expected ion flux and distance of the pinhole from the ion source, with typical diameters being in the region 50-100 μm. The electric and magnetic fields are parallel to each other and perpendicular to the initial direction of the motion of the particles. The ions are deflected by the applied electric and magnetic fields as they travel through this region, their trajectory being dependent on their energy and charge-to-mass ratio.

Under the influence of the magnetic field, the ion trajectories will be bent in the orthogonal direction to the field, whereas the electric field causes the ions to drift parallel to the field, as shown schematically in figure 4.10. The energy resolution and range of the diagnostic will therefore be dependent on how much dispersion the deflecting fields can induce, which in turn is affected by the detector size and the solid angle projected by the entrance pinhole. Using stronger electric fields however will cause the low energy ions to impact with the negative electrode plate, which can cause fluctuations in the applied electric field. The separation of the plates at the detector end therefore also dictates the range of detectable ion energies. The ions leave the dispersion region and propagate towards a detector at the back of the spectrometer. Separating out the ions as a function of their energy forms parabolic ion signal in the detector plane, with each parabola representing signal from an ion of a given charge-to-mass ratio.

In order to extend the energy range detectable by the TP spectrometer up to tens of MeV ion energies, without compromising the compactness of the diagnostic or causing low energy ions to impact with the electrode plates, the design of an spectrometer for use in laser driven ion acceleration experiments is modified slightly [20] from the typical parallel plate design. The electric field is provided by a pair of copper electrode plates connected to a 5 kV high voltage supply. The design is modified by making use of a wedged configuration for the electrode plates, whereby the negative plate is angled with respect to the positive plate. This configuration gives rise to an increasing separation between the plates, from 2 mm at the entrance of the spectrometer up to 22.5 mm at the detector side (see figure 4.10). The resulting electric field is therefore at a maximum at the entrance of the dispersion region and decreases as a function of the distance travelled through the spectrometer.

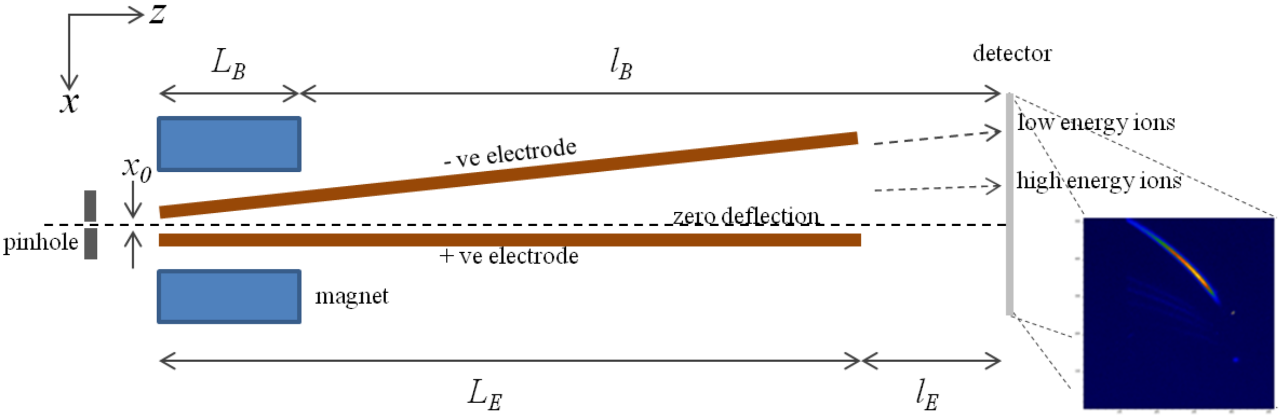

Figure 4.9: Schematic of the modified TP ion spectrometer. The image inserted was taken using an EMCCD camera and a scintillating medium for the detector and displays the resultant parabolic ion tracks formed in the detector plane.

The magnetic fields of the spectrometer employed in the work presented in chapter 5 are provided by a pair of 50 mm × 50 mm permanent ceramic magnets. With a pole separation of 20 mm the magnetic field peaks at ~ 0.2 T at the central point between the magnets.

By assuming that the magnetic field is constant in the 50 mm long region between the magnets and that the electric field is given by $\frac{V}{x_{plates}}$, where V is the potential difference and $x_{plates} = x_0 + Az$ is the distance between the plates at a point z along the plates, the particle deflection can be calculated. The dispersion, d, from the zero deflection point is caused as the ion travels with velocity υ_z through electric (E) and magnetic (B) fields is given by application of the Lorentz force equation (equation 2.18) as:

$$d_E = \frac{qE_0L_B}{m_i\upsilon_z^2}\left(\frac{1}{2}L_E + l_E\right) \tag{4.5}$$

$$d_B = \frac{qB_0L_B}{m_i\upsilon_z}\left(\frac{L_B}{2} + l_B\right) \tag{4.6}$$

where q, m_i are the ion charge and mass respectively. L_E and L_B are the lengths of the electric and magnetic fields along the direction of propagation and the distances of the electric and magnetic fields from the detector plane are given by l_E and l_B.

4.4.2.1. Proton beam spectra extraction from TP ion spectrometers

The ions can be detected using various types of particle track detector, such as CR39 plastic and photostimuable image plate, or microchannel plates. A scintillator was used as the detector plate for the TP ion spectrometers used in the work presented in chapter 5 to avoid the constrains of using passive media which can only be used once per shot and requires lengthy post-processing. When ions deposit their energy into the Anthracene-doped plastic, optical emission is given off due to a fluorescence process, therefore converting the ion signal into a light signal. Scintillators coupled to charge couple devices (CCD’s) are seen as an active detector medium, as once the fluorescence has finished (~ few ns) the detector is ready to be used again. The light signal can be captured using a camera imaging the back surface of the detector, therefore avoiding the need to post-process the detector before spectrum extraction.

A polyvinyltoluene-based scintillator of type BC-422Q was placed in the detector plane (shown in figure 4.10) and optically coupled to an Electron Multiplying Charge

Couple Device (EMCCD) to collect the light output. During earlier shots, the CCD counts were calibrated with a CR39 track detector for proton energy and proton fluence so that absolute proton numbers could be extracted from the signal counts. The calibration technique consisted of using pieces of machine-slotted CR39 that were placed on top of the scintillator detector at the back of the TP ion spectrometer (see figure 4.9). In the regions close to the edge of the slots the number of protons recorded by the CR39 detector across the width of the parabola track was compared to the CCD counts detected from the scintillation. The calibration was conducted over a proton range of 0.22-1.2 MeV. It was found that the CCD count/proton/MeV was roughly constant, at 0.13, in this energy range. Simulated parabolic ion tracks can be used alongside the real signal in order to identify the ions species that they belong to. The ion energy is then calculated by using the magnetic dispersion formula, d_B, and solving for v_z in incremental steps along the parabola. The proton spectra presented in chapter 5 were extracted by converting the CCD counts to proton numbers and plotting this as a function of the proton energy.

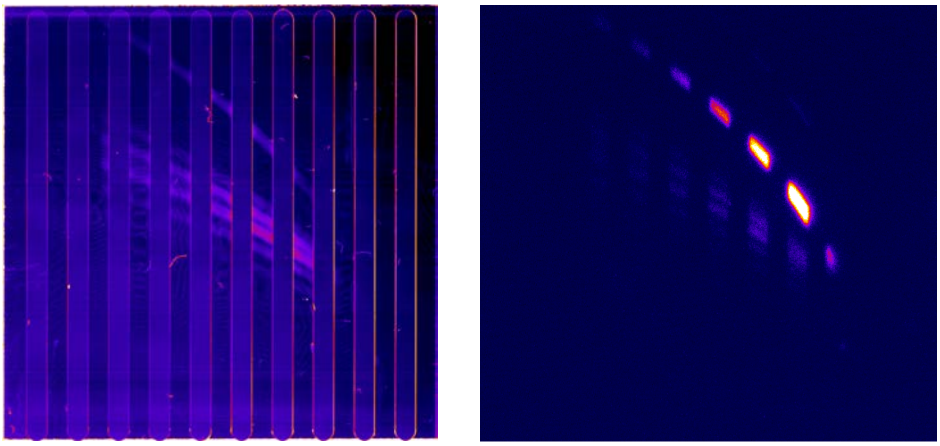

Figure 4.10: Example images of the CR39 detector (left) and scintillator detector (right) used for the TP ion spectrometer calibration

4.4.3. Reflectivity monitor

The implementation of a reflectivity monitor into the diagnostic suite provides a quick and easy measurement of the amount of light that is not absorbed into the plasma during the laser-plasma interaction. To first order therefore, this diagnostic enables one to quickly compare the amount of light energy absorption at the front surface relatively from shot-to-shot. This proved particularly useful during the two experimental campaigns discussed in this thesis as the absorption greatly affects the parameters of the hot electron population and subsequent ion acceleration and is therefore a key interaction parameter to monitor. It was useful to monitor the relative absorption during the double-pulse interactions used in the work presented in chapter 7 for example, so that one can identify whether the affect on the proton flux and conversion efficiency could be due in part to front surface absorption changes.

During every shot, imaging cameras are used to record the amount of incident ω light that is reflected, and frequency doubled 2ω light that is produced, at the critical surface of the interaction by placing a scattering screen of Polytetrafluoroethylene (PTFE) in the specular direction of the laser pulse. The imaging cameras are used together with a series of optical filters to insure that the camera chips are not over-exposed during the image capture duration. A measurement of relative reflectivity from the laser-plasma interaction is extracted from the images by accounting for differences in quantum efficiency of the cameras at the two wavelengths and then for shot-to-shot variation in laser energy delivered onto the target. The total amount of 1ω and 2ω signal recorded by the two cameras is then normalised to give an approximation of the relative reflectivity between the shots taken in the data set explored. In the case of the single and double-pulse shots taken during the experimental campaign described in chapter 7, the reflectivity measurements were normalised to the single pulse irradiation shot, to provide a comparison.

4.5. Numerical simulations using 1D Particle-In-Cell (PIC) codes

Numerical simulation codes are powerful and useful tools in the study of laser plasma interactions. They can be used alongside experimental data to give the user a better understanding of the physics underlying the interaction and subsequent observation or to probe parameters that cannot be directly measured. Naturally, there are different types of codes depending on the plasma conditions under which the interaction takes place. For example, long pulse (ns) laser interactions with under-dense plasmas are well described by modelling the plasma as a fluid and employing the magnetohydrodynamic equations in order to solve for macroscopic parameters such as mass density, pressure and temperature.

By contrast, in the interaction regime of short pulse (< ps), intense laser irradiation of a solid density target, an electron oscillating in the fields of the laser pulse will be accelerated to relativistic energies. The collision rate between particles is inversely related to the particle velocity, υ_i, going as υ_i^{-3}. Consequently, as the electrons are accelerated toward relativistic velocities during the rising edge of the laser pulse, the collision rate quickly decreases substantially. Therefore, a kinetic description of the plasma dynamics is required as the collision-less nature of the hot electrons produced at the target front side means that particle distributions cannot be assumed to be Maxwellian. A fully kinetic approach, in which the distribution function is solved with self-consistent electromagnetic (EM) fields, via Maxwell's equations, is a more suitable approach in this case. Each particle species in the plasma, with mass m_j and charge q_j, can be assigned to a distribution function, $f(\boldsymbol{r},\boldsymbol{\upsilon},t)$, which describes the number of particles with velocity $\boldsymbol{\upsilon_j}$, spatial coordinate $\boldsymbol{r_j}$ at a time t. A fully ionized plasma under the influence of external and internal EM forces is a good description of the interaction for ultra-short (< 100 fs) pulse irradiation wherein the particle distribution function is modelled as evolving in accordance to the kinetic equation:

$$\frac{\partial f_j}{\partial t} + \boldsymbol{v_j}.\frac{\partial f_j}{\partial \boldsymbol{r_j}} + q_j\left(\boldsymbol{E} + \frac{\boldsymbol{v}_j}{c} \times \boldsymbol{B}\right).\frac{\partial f_j}{\partial(\gamma m_j \boldsymbol{v_j})} = \frac{\partial f}{\partial t}_{coll} \qquad (4.7)$$

where c is the speed of light, γ is the relativistic factor, $\boldsymbol{E}$ and $\boldsymbol{B}$ are the electric and magnetic fields respectively. Neglecting collisions means that the right-hand-side of equation 4.7 is zero, otherwise known as the Vlasov equation.

The Particle-In-Cell (PIC) method [21] is an efficient approach for determining the appropriate particle motion and coupling of the distribution to Maxwell's equations in order to derive the subsequent evolution of the plasma over spatial and temporal coordinates. The very large number of particles in a real plasma are represented by a much lower number of discrete 'macro-particles', of mass m_j and charge q_j, which are mapped to an Eulerian spatial grid. The individual trajectories of the macro particles are first determined by the Lorentz equation and then the charge, ***j*(*r*)**, and mass, *ρ*(***r***), densities needed to solve Maxwell's equations are extracted by mapping the macro particle positions and velocities onto the mesh grid. Once ***j*(*r*)** and *ρ*(***r***) are defined at the grid points, the solutions to Maxwell's equations can be used to obtain the resultant electric and magnetic fields. These can then be interpolated back onto the particle distributions and the cycle continues to the next time step by applying the Lorentz force to the macro particles (see figure 6.1). There are two ways in which the code can advance to the (n + 1)th time step from the nth time step; by using information from the nth time step only (an explicit method) or by using information from the both the current (n) and later (n + 1) time step (an implicit method). The former requires that the time step of the simulation is smaller than the shortest time period of the plasma interaction, which is ~ ω_p^{-1}, and while the latter is a more stable numerical approach it is also computationally demanding.

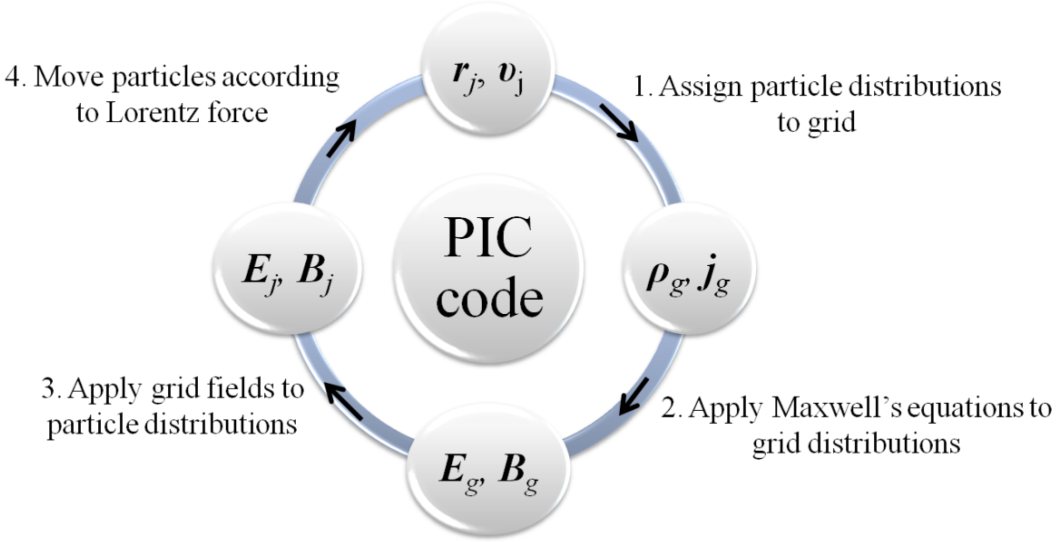

Figure 4.11: Schematic illustration of the PIC algorithm [22]**.**

The grid is divided into a number of cells, the width δx of which must be defined so that the Debye length of the plasma can be resolved in order to maintain stability within the code, implying the following condition must hold true throughout:

$$\delta x < \sqrt{\frac{\varepsilon_0 k_B T_e}{n_e e^2}} \tag{4.8}$$

where $k_B T_e$ is the temperature of the plasma in eV, n_e is the electron density and e is the electronic charge. The code assumes quasi-neutrality for the plasma and therefore assigns the initial electron density according to the particle densities and the charge state of any heavy ions defined by the user in the input file. Most descriptions of the electron density in simulations are given in terms of the critical density, n_{crit}, of the plasma as defined by the laser pulse parameters in order to quickly ascertain whether the laser fields are interacting with an under-dense ($n_e < n_{crit}$) or over-dense ($n_e > n_{crit}$) plasma. For a given initial electron density the Debye length resolution condition places a restriction on either the minimum initial temperature of the plasma or the maximum cell width of the grid, depending on which parameter the user is willing to compromise with. It is common practice however to initiate the plasma with an inflated temperature, in order for the code to run efficiently.

A basic PIC code algorithm will describe the evolution of a collision-less plasma since the plasma particles are interacting with the collective EM field rather than with each other, which is a reasonable approximation for the interaction of an intense, short pulse laser field with an ultra-thin foil. Furthermore, PIC codes self-consistently model the laser interaction at the front side of the plasma as well as the subsequent proton acceleration by hot electron generation.

Owing to their relative ease of implementation, PIC codes remain a popular choice for simulating a kinetic model description of the laser plasma interaction and are therefore important in the study of laser-driven electron and ion acceleration. The development of the code to run on parallel processors and vast improvements in computing power over the past two decades have led to the ability to run full 3D PIC simulations [23] [24], although these still require the use of a dedicated large cluster network and remain computationally expensive and time consuming. Therefore, for interactions that can be reduced to a 1D geometry, versions of the PIC technique that are run with one spatial dimension but retain three momentum components, so-called 1D3P PIC codes, are a viable and attractive alternative.

References

1. McClung, FJ and Hellwarth, RW. Giant optical pulsations from ruby. *Applied Optics*, 1, 101 (1962), 103--105.
2. Strickland, D. and Mourou, G. Compression of amplified chirped optical pulses. *Optics Communications*, 55, 6 (1985), 447--449.
3. Le Blanc, C., Curley, P., and Salin, F. Gain-narrowing and gain-shifting of ultra-short pulses in Ti: sapphire amplifiers. *Optics communications*, 131, 4-6 (1996), 391--398.
4. Ross, I.N., Matousek, P., Towrie, M., Langley, AJ, and Collier, JL. The prospects for ultrashort pulse duration and ultrahigh intensity using optical parametric chirped pulse amplifiers. *Optics communications*, 144, 1-3 (1997), 125--133.
5. Collier, J., Hernandez-Gomez, C., Ross, I.N., Matousek, P., Danson, C.N., and Walczak, J. Evaluation of an ultrabroadband high-gain amplification technique for chirped pulse amplification facilities. *Applied Optics*, 38, 36 (1999), 7486--7493.
6. Hernandez-Gomez, C., Brummitt, PA, Canny, DJ et al. Vulcan petawatt-operation and development. In *Journal de Physique IV (Proceedings)* (2006), 555--559.
7. Danson, CN, Brummitt, PA, Clarke, RJ et al. Vulcan petawatt: Design, operation and interactions at 5×10^{20} Wcm^{-2}. *Laser and Particle beams*, 23, 01 (2005), 87--93.
8. Hawkes, S., Collier, J., Hooker, C. et al. Adaptive optics trials on Vulcan. *Central Laser Facility Annual Rep*, 2001 (2000), 153.
9. Shaikh, W., Musgrave, I., Hernandez-Gomez, C., Parry, B., and Johnson, D. A High Contrast Dual OPCPA Pre-Amplifier System Using Both Picosecond and Nanosecond Pump Pulses for the Vulcan Petawatt Facility. In *Advanced Solid-State Photonics* (2010).
10. Musgrave, I. Pre-pulse generator for controllable picoseconds pre-pulses in TAP. *Central Laser Facility annual report* (2011).
11. Divall, EJ, Collier, JL, and Ross, IN. *Contrast enhancement using gating*

techniques. CLF Annual Report. 2006.

12. Musgrave, I.O., Hernandez-Gomez, C., Canny, D.J., Collier, J.L., and Heathcote, R. Detailed study of the impact of the Vulcan OPCPA pre-amplifier on contrast. In *Lasers and Electro-Optics, 2006 and 2006 Quantum Electronics and Laser Science Conference. CLEO/QELS 2006. Conference on* (2006), 1--2.
13. Langley, AJ, Ertel, K., Divall, EJ, Smith, JM, Chekhlov, O., Hooker, CJ, and Collier, JL. *New front-end for the Astra Gemini project*. CLF Annual Report. 2006.
14. Jullien, A., Albert, O., Burgy, F. et al. 10\^-10 temporal contrast for femtosecond ultraintense lasers by cross-polarized wave generation. *Optics letters*, 30, 8 (2005), 920--922.
15. Ziener, C., Foster, PS, Divall, EJ, Hooker, CJ, Hutchinson, MHR, Langley, AJ, and Neely, D. Specular reflectivity of plasma mirrors as a function of intensity, pulse duration, and angle of incidence. *Journal of applied physics*, 93 (2003), 768.
16. Doumy, G., Quéré, F., Gobert, O. et al. Complete characterization of a plasma mirror for the production of high-contrast ultraintense laser pulses. *Physical Review E*, 69, 2 (2004), 026402.
17. Dromey, B., Kar, S., Zepf, M., and Foster, P. The plasma mirror—A subpicosecond optical switch for ultrahigh power lasers. *Review of scientific instruments*, 75 (2004), 645.
18. http://www.srim.org/
19. Scott, GG., Green, JS., Fiorini, F. et al. Maximising the dynamic range of radiochromic film through novel scanning techniques. *Central Laser Facility annual report* (2010-2011).
20. Carroll, DC, Brummitt, P., Neely, D., Lindau, F., Lundh, O., Wahlström, C.G., and McKenna, P. A modified Thomson parabola spectrometer for high resolution multi-MeV ion measurements--Application to laser-driven ion acceleration. *Nuclear Instruments and Methods in Physics Research Section A: Accelerators, Spectrometers, Detectors and Associated Equipment*, 620, 1 (2010), 23--27.

21. Birdsall, C.K. and Langdon, A.B. *Plasma physics via computer simulation*. Egully. com, 2004.
22. Gibbon, P. *Short pulse laser interactions with matter*. Imperial College Press London, 2005.
23. Fonseca, R., Silva, L., Tsung, F. et al. OSIRIS: a three-dimensional, fully relativistic particle in cell code for modeling plasma based accelerators. *Computational Science—ICCS 2002* (2002), 342--351.
24. Pukhov, A. Three-dimensional simulations of ion acceleration from a foil irradiated by a short-pulse laser. *Physical review letters*, 86, 16 (2001), 3562--3565.

Chapter 5: Scaling of laser-driven sheath acceleration of protons following the interaction of intense, defocused laser pulses with ultra-thin foil targets

In this chapter the dependence of the fluence and maximum energy of laser accelerated protons on laser energy and focal spot size following the interaction of an intense laser pulse with an ultra-thin foil is explored. The scaling of the fluence and maximum energy of TNSA-protons has been investigated as a function of laser pulse energy in the range 20-350 mJ at intensities of 10^{16}-10^{18} W/cm^2. The pulse duration and target thickness were fixed at 40 fs and 25 nm respectively, while the laser focal spot size and drive energy were varied. The results indicate that whilst the maximum proton energy is strongly dependent on both the laser energy and laser spot size, the proton fluence is primarily related to the laser pulse energy under the conditions studied here.

5.1 Introduction

The study of how laser-driven ion acceleration scales with laser pulse parameters originates from a desire to quantify the effect that a change in the laser parameters has on the intermediary hot electron population and subsequently on the proton beam produced. In a practical sense, this is essential in order to determine how laser accelerated proton beams can be controlled through careful selection of the laser parameters. Furthermore, scaling relations can be used to extrapolate beyond the laser intensities currently available in order to predict what one might achieve with the advent of improved laser technology. It is common practice to present scaling relations in terms of laser intensity and to concentrate on the scaling of maximum proton energy. This motivates two areas of experimental enquiry: 1) does a given laser intensity scaling relation hold true independent of whether it is the laser energy, focal spot size or pulse duration that is varied? And 2) can other parameters, such as the fluence of accelerated protons, also be described using an intensity-based scaling relation?

There are many types of high-power lasers available for experimental investigation of ion acceleration. However, many of the applications of this novel ion source require high shot repetition rates (0.1 – 10 Hz) and the ability to tailor the proton beam to the desired application through laser parameter selection. Currently, the optimum laser technology that fulfils the high repetition rate requirement dictates that the laser energy is delivered in the form of very short pulse lengths, circa 40 fs, in order to reach the threshold intensities needed for MeV ion acceleration. Such laser systems are now affordable and readily available to many groups for table-top particle acceleration use. It is therefore important to have a good understanding of how the laser driven ion acceleration mechanism responds under these conditions. At the laser intensities of interest reported here (10^{16} - 3×10^{18} W/cm^2), Target Normal Sheath Acceleration [1] is the dominant ion acceleration mechanism (see chapter 3).

In this chapter proton acceleration is explored using a short pulse, high repetition rate laser operating at, and just below, the relativistic intensity regime (~ 10^{18} W/cm^2).

The objective of the study is to determine to what extent the proton beam properties (fluence as well as the maximum energy) depend on the laser pulse energy and focal spot size. Such control of the proton beam will be essential for many applications.

A handful of studies have been carried out to investigate how ion beam properties scale with laser intensity and laser pulse duration [2] [3] [4] [5] [6] [7]. However these have been obtained using very different interaction conditions to the ones presented here. Published material that is more relevant to this interaction regime is available [8] [9] [10] [11] in the literature, yet a dedicated study into the dependence of proton beam properties on the laser drive energy and focal spot size explicitly has yet to be reported in the regime of laser plasma interaction studied here, thus acting as motivation for the present work.

5.2 Experimental method

The experiment was conducted using the Astra Ti:Sapphire laser system (described in chapter 4), which is capable of producing 40 fs laser pulses and delivering up to 650 mJ of energy onto a target. The maximum intensity of the ASE pedestal and of any pre-pulses was characterised by measuring the laser intensity contrast; defined as the ratio between the intensity of the main pulse and of the laser prepulse that precedes it. When operated normally, a contrast ratio of 2×10^6 at 1 ns before the main pulse was measured. A higher contrast ratio was achieved with the use of a single plasma mirror system (described in chapter 3), which enhanced the contrast to 10^8 at 1 ns before the main pulse. The plasma mirror system [12] consisted of an anti-reflection coated, glass substrate that was positioned in the beam so that it was irradiated with p-polarised laser light at an intensity of 5×10^{15} W/cm^2, chosen so as to optimise the reflectivity at the highest laser energy. The plasma mirror efficiency was characterised for each laser energy that was incident on the plasma mirror, peaking at 56 % reflectivity. Two F/8 off-axis parabolas were used to focus the beam onto the plasma mirror and then re-collimate it after reflection (see figure 5.1). The plasma mirror substrate was moved after every shot, so that only undamaged areas of the substrate were exposed to the incoming laser pulse. The quality of the reflected beam was confirmed regularly using an equivalent plane monitor which measured a leakage from the last turning mirror. The beam was then focused onto a 25 nm thick plastic film target at an incident angle of 45 degrees, in p-polarised geometry, using an F/2.5 off-axis parabola capable of delivering a peak intensity of ~2×10^{19} W/cm^2 with a spot size of 4 x 6 μm^2 at the best focus position. The optimal distance of the target relative to the focusing parabola for producing the smallest laser spot diameter was achieved to within an accuracy of ± 6 μm and was defined by using a retro-focus system diagnostic [8].

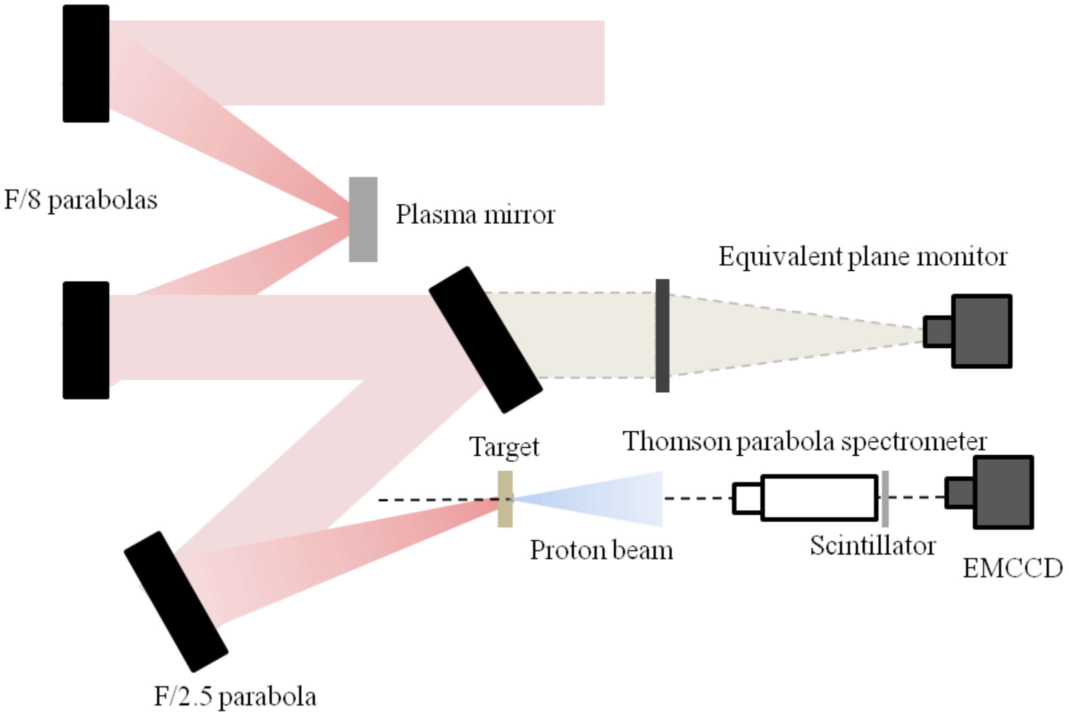

Figure 5.1: Schematic of the experimental arrangement with the inclusion of the plasma mirror system

The size of the focal spot was measured using an absolutely calibrated equivalent plane monitor and obtained by moving the target towards the focusing parabola along the laser axis. The laser spot intensity distribution away from best focus was measured at lower power using a camera lens objective and was found to have a relatively unstructured spatial distribution. To avoid any pre-plasma formation prior to the leading edge of the main pulse interacting with the front surface of the target, the pre-pulse intensity was confined to a maximum of ~ 3×10^{10} W/cm^2, which is well below the plasma formation threshold for a dielectric [12]. To achieve this, in addition to the 10^8 contrast provided by the plasma mirror system, a minimum laser spot size of diameter 20 μm was adopted in this campaign, yielding an effective maximum laser intensity of 3.2×10^{18} W/cm^2 at the highest laser energy (380 mJ). The use of an ultra-thin target implies that recirculation [13] within the target will play a significant role during the laser interaction; a process which has been used to explain enhanced proton signals compared to thicker targets [14]. The target thickness and laser pulse duration were held constant, with the former chosen for being close to optimal values for maximum proton fluence determined from earlier studies [15] so that scaling could be studied in this region of highest possible fluence delivery. In order to study the response of the proton beam fluence and maximum energy to changing laser energy, the energy delivered to the target was varied from ~ 20 mJ up to ~350 mJ for two focal spot size diameters, 20 μm and 60 μm. To study the effect of changing the focal spot size, the laser energy was then held constant whilst the focal spot size diameter was varied from 20 μm to 140 μm.

The primary diagnostic used for this study was a Thomson parabola ion spectrometer [16] positioned so as to sample the protons accelerated in the target normal direction through a pinhole that subtended a solid angle of 1.1 ± 0.2 μsr. The proton signal was detected using an absolutely calibrated scintillator (see section 4.4.2.1.) that was optically coupled to an Electron Multiplying Charge Couple Device (EMCCD) to give instantaneous spectra measurement over the range 0.12 – 5 MeV for protons.

5.3. Fluence of accelerated protons as a function of laser energy and focal spot size

5.3.1. Experimental results

The proton spectra obtained by varying laser drive energies are plotted in figures 5.2(a) and 5.2(b), for a laser spot size of 20 μm and 60 μm respectively. Figure 5.2(a) shows that both the proton flux and maximum proton energy reduce with decreasing laser intensity. Using similar drive laser energies, the scan was repeated but with an approximately nine times larger area of laser irradiation and the resulting spectra plotted in figure 5.2(b). It should be noted that for the lowest laser energy using a 60 μm spot size (where the laser intensity is 1.9 x 10^{16} W/cm^2), despite operating very close to the 0.15 MeV proton detection threshold of the spectrometer, resolvable data are still produceable.

Comparing the features of figure 5.2(a) to those of figure 5.2(b), we find that the spectra exhibit broadly similar behaviour. The absolute numbers of protons sampled through the pinhole are comparable, if not higher at lower proton energies (< 0.75 MeV), for the larger laser spot size despite the intensities on target being an order of magnitude lower. In the paper by Green *et al* [18], a similar observation was attributed to the competing effects of a larger rear surface source size and a lower drive intensity, resulting in the optimised proton fluence not being obtained with the smallest focal spot size. Another feature common to all spectra shown in figure 5.2 is that the peak in proton flux is not at the minimum energy detected, as one might expect with an exponentially decaying system.

Deviation from the ubiquitous quasi-exponential spectra of TNSA proton beams for sub-micron thick target foils has been explained by Robinson et al [19] as a result of the generation of a strong, focussing magnetic field close to the target axis on the rear surface of the foil. This self-generated magnetic field acts on a proton population within a small angle (< 0.5 mrad) to the target normal, the result of which is observed as peaks at the lower end (< 1 MeV) of the proton energy spectrum accompanied by a depleted area of proton signal at even lower energies where the protons have been deflected away from the axis by ‘over-focussing’. This effect is not normally detectable if the proton signal has been collected from the full solid angle of emission as it affects such a small percentage of the beam. However considering that the Thomson ion spectrometer only samples a very small part of the solid angle (1.1 ± 0.2 μsr) along the target normal axis, this spectral modification is observable.

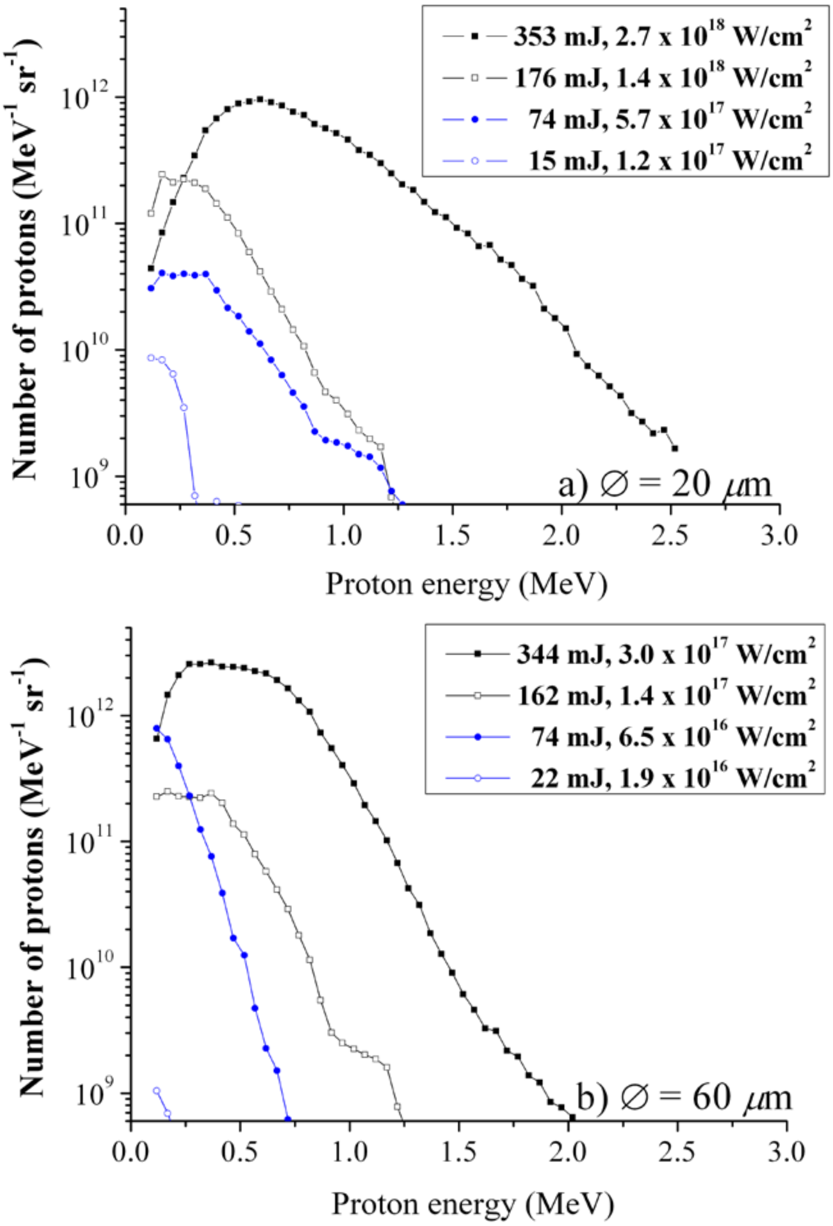

Figure 5.2: Experimentally measured proton energy spectra with varying laser energy for a laser spot diameter of a) 20 μm and b) 60 μm.

Examining our results in search of underlying trends, the maximum proton energy detectable above the level of the background (produced by scattered ions) of the Thomson ion spectrometer, E_{pmax}, and the proton fluence sampled through the pinhole (integrated over all detected proton energies, E_p, where $0.12 < E_p < E_{pmax}$) were plotted as functions of both laser intensity, I_L, and laser energy, E_L (see figures 5.3 (a-d)). For clarity, changes in the laser intensity brought about by changing the laser energy for a fixed laser spot size will be referred to as ‘varying laser energy’ and changes in the laser intensity brought about by changing the laser spot size at fixed energy will be referred to as ‘varying laser spot size’.

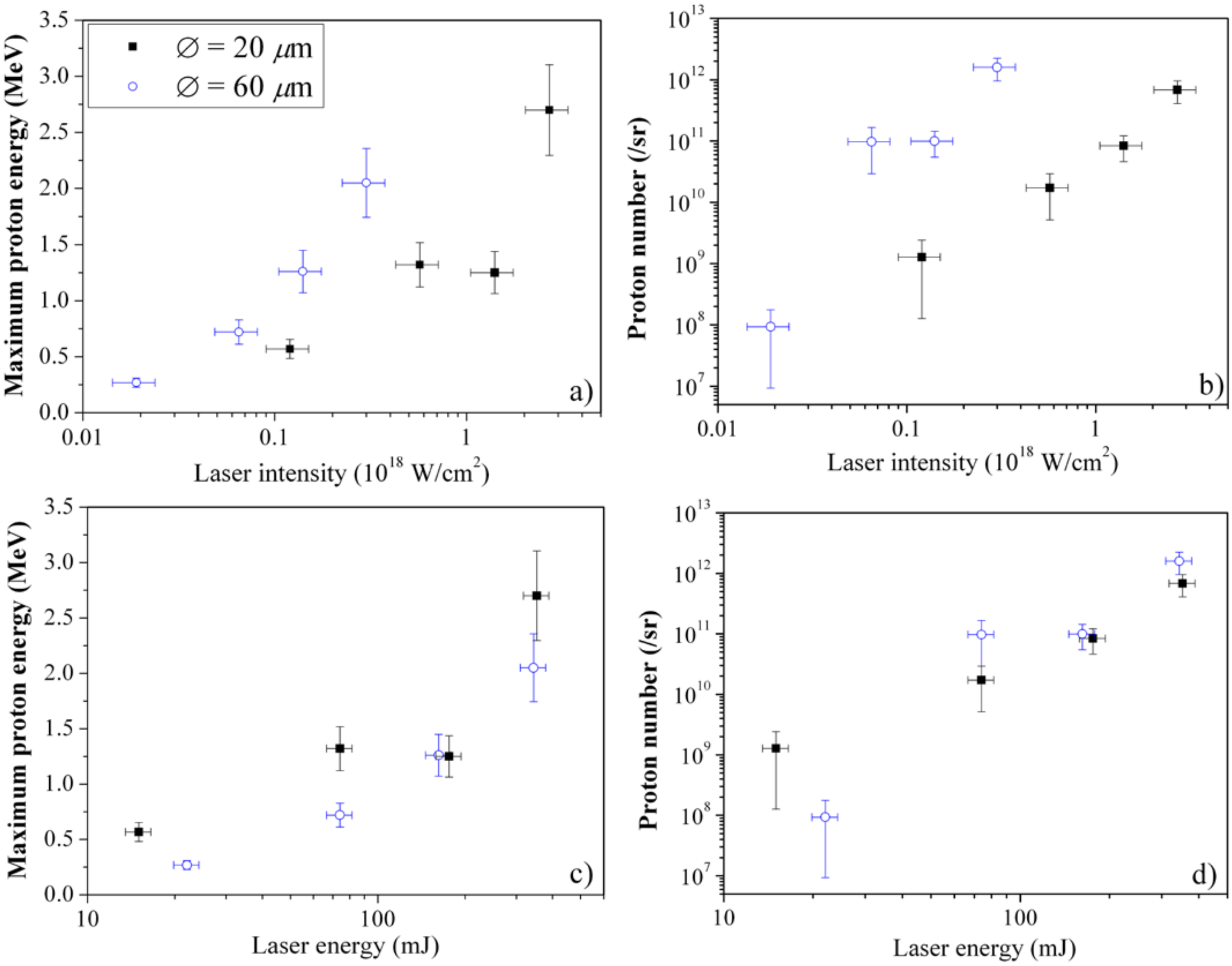

Figure 5.3 (a-d): Maximum proton energy (a,c) and integrated proton fluence (b,d) as a function of laser intensity and laser energy, for two laser spot size diameters 20 μm (filled black squares) and 60 μm (hollow blue circles).

When plotting these experimentally obtained values as a function of laser intensity (figures 5.3(a) and (b)), it is noticeable that, within each graph, the increase of the proton beam property with increasing laser intensity is similar for the two laser focal spot size data sets. Importantly however, data points accumulated for a spot size of 20 μm appear to lie on a separate trend line to those accumulated at a spot size of 60 μm when plotted as a function of laser intensity. Interestingly, there are also data points in figures 5.3(a) and 5.3(b) for which the calculated laser intensity is similar, yet it seems as though with a larger spot size the values are higher. However, it is vital to add that even though the laser intensity is similar for these points, the laser energy is not. Therefore, a more appropriate way in which we can examine the underlying trends is to also plot the proton beam properties as a function of laser energy. Figure 5.3(c) reveals a clear trend between maximum proton energy and laser energy and that for a given laser energy a higher value for E_{pmax} is obtained at a smaller focal spot size.

Figure 5.3(c) is a good illustration of the different scaling relations for maximum proton energy that can be obtained depending on whether one changes the laser energy or focal spot size. There is an order of magnitude difference in laser intensity between the data points for 20 μm and 60 μm focal spot size, yet the resulting rise in E_{pmax} is approximately half that which occurs when the laser intensity is increased by increasing the laser energy instead.

In comparison, the proton fluence from both illumination conditions demonstrates an increase of almost one-thousand times for an increase in laser energy of only twenty times, with both data sets overlapping in figure 5.3(d) despite there being almost an order of magnitude difference in intensity between the shots taken with the 20 μm and 60 μm focal spot diameter. It is significant to note that of the four figures 5.3(a-d), only figure 5.3(d) shows close matching of the two data sets, indicating a weak dependence of the proton fluence on the laser spot size compared with the effect of varying the laser energy.

In order to further investigate the effect of increasing the laser spot size on the proton beam produced, additional proton spectra were obtained using maximum laser energy but varying the laser spot size between 20 μm and 140 μm diameter (see figure 5.4). Again, the proton numbers and maximum energy reduce with decreasing laser intensity. However this time, with the laser energy held constant, there is a noticeable shift within the proton distribution as the focal spot size is increased; the number of high energy protons reduces, yet the number of lower energy (< 1 MeV) protons remains high, if not increases, as the laser intensity decreases.

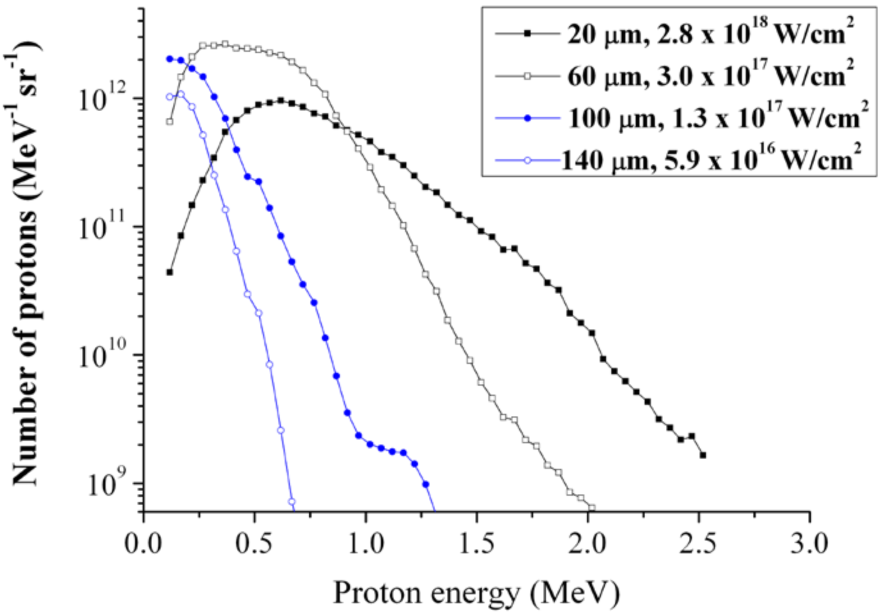

Figure 5.4: Measured proton spectra for constant laser energy (380 ± 40 mJ) at varying laser spot size, indicated in the figure legend.

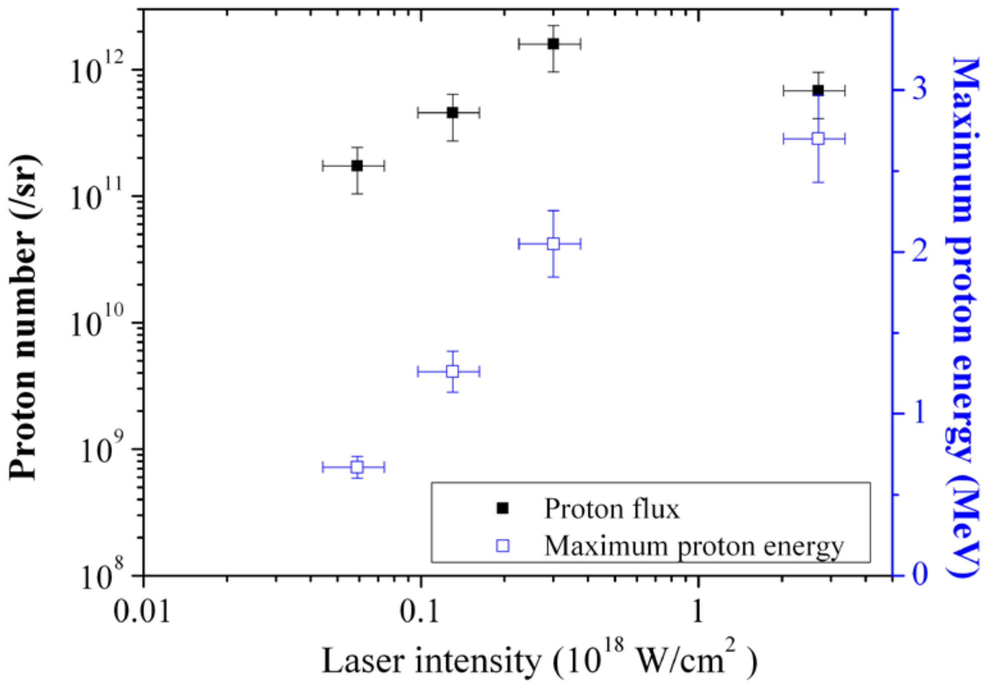

Figure 5.5: Maximum proton energy (hollow blue squares) and integrated proton number (filled black squares) plotted as a function of laser intensity for constant laser energy (380 ± 40 mJ) at varying laser spot size, from 20 to 140 *μ*m.

The proton fluence as a function of laser intensity is plotted in figure 5.5. For constant laser energy, one can see the effect of the laser spot size on the proton signal and how the proton fluence is not maximised at the smallest illumination size (20 μm) studied here, which is in good agreement with the results of Green *et al* [18]. This result will be discussed further in section 5.3.2. It is also apparent that even though the intensity has increased by approximately fifty times, the proton fluence has only increased by an order of magnitude, which is in stark contrast to when the laser energy is varied (see figure 5.3(b)). It should also be noted that the apparent drop in proton fluence in figure 5.5 at the lowest intensities is in fact a decrease in the number of protons with energy above the minimum detectable value of 150 keV.

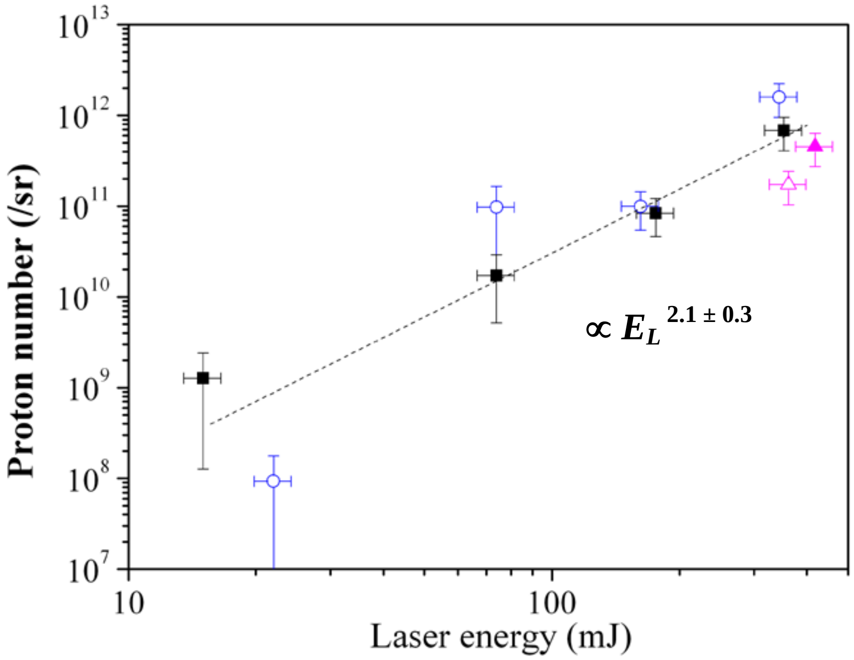

Figure 5.6: Proton fluence plotted as a function of laser energy for a laser spot size of diameter 20 μm (filled black squares), 60 μm (hollow blue circles), 100 μm (filled magenta triangle) and 140 μm (hollow magenta triangle), highlighting the significant role that laser energy plays in determining the proton flux obtained.

Finally, figure 5.6 shows the proton flux plotted as a function of laser energy with the inclusion of the integrated proton flux measured at laser spot sizes of 100 μm and 140 μm. The proton fluence scales with laser energy as $E_L{}^{2.1 \pm 0.3}$. The clear scaling relation between proton fluence and laser energy, across a range of laser spot sizes and over such a large intensity range serves to validate that the proton fluence is primarily dependent on the laser energy for the parameter range investigated here.

5.3.2. Discussion: dependence of proton fluence on laser energy

The dependency of TNSA-proton fluence on laser intensity by variation of laser energy has been investigated by other groups using femtosecond laser pulses [9] and longer [6] [7]. Similar experimental observations to those discussed here are reported by Oishi *et al* [9] whereby scaling relations for maximum proton energy are determined as a function of driving pulse duration using short pulses (55 fs to 400 fs) in the intensity range 10^{17} – 10^{19} W/cm^2. The proton spectra in that study are remarkably similar to the spectra that have been discussed above, despite there being a significant difference in the laser contrast conditions and target thickness (5 μm). It is also interesting to note that similar proton fluence scaling to that reported here has been observed by others despite there being a wide range of interaction conditions. Robson *et al* [7] made observations of the scaling of the proton-induced activity of copper with laser energy, finding it to scale with an exponent of 2, which compares well with the scaling reported here of 2.1 ± 0.3 (see figure 5.6). Robson *et al* studied the interaction of picosecond, high energy (~20-400 J) laser pulses with several microns thick foil targets at best focus under the intensity regime of 10^{19}-10^{20} W/cm^2, whereas the present study has been conducted using ultra-short (40 fs), lower energy (0.4 J), thin (25 nm) foil targets in a defocused geometry.

The results in this chapter together with those of Oishi *et al* [9] and Robson *et al* [7] show that the scaling of the proton fluence with laser energy appears to be similar whether there is a significant pre-plasma or not and also whether the target is ultrathin or not. However, that is not to say that the absolute value of proton fluence is weakly dependent on plasma scale length, as indeed absorption of the laser's energy at the front surface is highly dependent on plasma scale length [20]. By displaying a very similar pattern of behaviour over the two interaction conditions, this serves to highlight the robust and global nature of the strong dependence of the proton fluence on the laser energy, for TNSA-proton beams.

In attempting to explain the relation between total proton fluence and laser energy, it is useful to recall the underlying acceleration mechanism. The TNSA mechanism is directly affected by the population of suprathermal (so called ‘hot’) electrons originating from the front side of the target and the subsequent electrostatic sheath field that they generate on the rear surface. The parameters that describe this ‘hot’ electron population, such as the number density and the temperature, determine the properties of the beam of accelerated protons. The amount of laser energy coupled into the hot electron population and the transport of this population through to the rear surface are thus key determinants of the accelerating sheath field. The maximum proton energy is related to the hot electron temperature, density and sheath acceleration time at the rear of the target [21] (see equation 3.3), whereas the total number of protons accelerated is likely to also be affected by the subsequent temporal and spatial evolution of the sheath field once it has maximised.

Figures 5.4 and 5.5 together provide an insight into the effect of changing the laser focal spot size on the proton beam produced (while maintaining constant laser energy) that goes some way to explore the relationship between laser energy and proton fluence. As already identified, a decrease in the laser intensity produced by increasing the spot size appears to result in a spectral shift whereby a decrease in the number, and maximum energy, of higher energy protons is balanced by an increase in the number of low energy protons. This shift in the fluence from high to low energy results in a very slowly varying total proton fluence, when integrating across the entire spectrum, for constant laser energy delivered to the target. Using this hypothesis, the fast fall-off in total proton fluence measured at the two largest focal spot sizes in figure 5.5 is consistent with, as mentioned earlier, the diagnostic being unable to detect protons with energy below 150 keV rather than an indication of the real decrease in total proton fluence. However a decrease in the proton fluence at very large focal spot sizes is to be expected as the quality of the focal spot distribution and the uniformity of the intensity of irradiation will decrease substantially, thus degrading the electron sheath charge separation field developing on the rear surface and decreasing the number of ions accelerated.

A similar spectral shift with increasing laser focal spot size was also measured by Green *et al* [18]. They examined two effects on the proton acceleration that arise when the laser spot size is increased; the increase in the area of the rear surface over which acceleration is driven and the changes in the proton spectra with intensity (at constant laser energy and pulse duration). The analytical model described by Green *et al* sufficiently describes the competition between these two effects and is used to reproduce the response of the spectral flux to a change in laser focal spot size.

In considering the case in which laser energy is varied, it is useful to identify the stages of energy transfer that occur in laser-solid interactions.

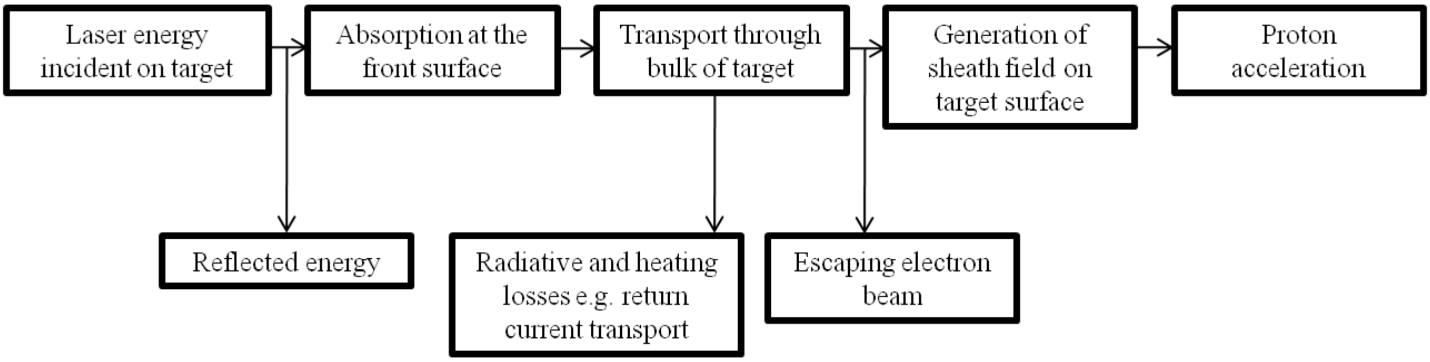

Figure 5.7: Flow diagram of energy transfer and loss in a solid target irradiated by a high power laser pulse.

The flow diagram presented in figure 5.7 is a very basic approximation to the energy transfer processes that occur giving rise to the TNSA mechanism, it does however illustrate the key sources of energy transfer and loss. After absorption of the laser energy into a population of hot electrons at the target front side, it is assumed that, for thin targets, energy losses in the hot electron transport represent a small fraction of energy contained in the hot electron beam. The energy contained within the hot electron beam that reaches the rear surface would therefore be proportional to the energy absorbed.

It has been found experimentally [22] [23] that under ultra-high intensity contrast conditions, where pre-expansion of the front surface prior to the pulse arriving is negligible, the laser energy absorption efficiency is almost constant across the intensity range of interest here. The conditions in this experimental study were carefully controlled so as to ensure a steep plasma gradient interaction, implying that the amount of energy absorbed was directly proportional to the laser energy delivered on to the target. Together with the results of figures 5.4 and 5.5, what this energy transfer discussion shows is that a constant laser energy, and hence energy coupled into the target, gives rise to an almost constant total proton fluence in the beam accelerated along target normal with the proton spectral distribution defined by the effective laser intensity. An increase in laser energy therefore not only expands the proton spectrum out to higher maximum proton energies but also gives rise to a proportional increase in the energy available for proton acceleration across the spectrum. Through careful control of the laser parameters, varying one parameter at a time, the experimental study carried out here clearly demonstrates this effect of laser energy on the spectra in figure 5.2.

The numerical value of the exponent in the proton fluence scaling law that goes as $E_L^{2.1\pm0.3}$ primarily results from a function of electron temperature and density that changes over temporal and spatial domains as the plasma sheath expands at the rear surface. One explanation could be that an increase in laser energy at constant focal spot size (therefore equivalent to an increase in laser intensity), delivers a population of hot electrons to the rear surface with a higher temperature (an intensity dependent function that has a less than linear relation) as well as higher energy content (proportional to the increase in laser energy, leading to higher electron number) resulting in higher electron density, which generates an accelerating sheath that exists for longer times and evolves slower so that the net result is a more than proportional increase in the total proton fluence. This follows if one recalls that acceleration occurs up until the point at which the sheath electrons have expanded significantly or cooled sufficiently (by transferring their energy predominately to the protons) so that the charge separation potential decreases to below the threshold for significant acceleration; a higher density of electrons of higher energy will take longer to do this.

It is worth noting that the measurements made here are of protons emitted from the centre of the beam in the target normal direction and it is not trivial to apply this scaling to the proton emission as a function of angle. Mora [21] shows that the number of accelerated protons is proportional to the number of hot electrons. The net fluence of hot electrons that contribute to the central region of the sheath field on the rear surface is made up of electrons that have made a single pass through the target as well as those that are refluxing, whereas the net electron fluence far from the injection region is a result of transverse spreading of electrons in thin targets alone. Therefore, it is possible that the dynamics of the sheath properties and the subsequent effect on the proton fluence are slightly different away from target normal.

5.4. Maximum proton energy as a function of laser energy and focal spot size

5.4.1. Experimental results

The maximum proton energy has been plotted as a function of intensity in the case of changing laser energy (reproduced in figure 5.8) and then as a function of intensity in the case of changing focal spot size (reproduced in figure 5.9(a)).

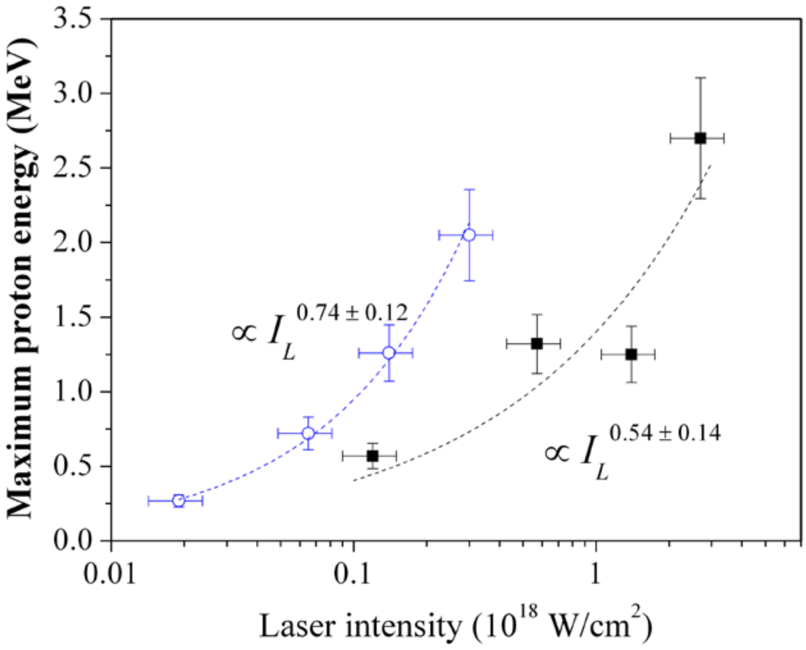

Figure 5.8: Maximum proton energy plotted as a function of laser intensity obtained with a laser focal spot size of 20 μm (black filled squares) and 60 μm (blue hollow circles) with the addition of trend lines fitted to the data.

Plotting E_{pmax} as a function of I_L for both laser spot sizes (see figure 5.8.) demonstrates a slowly varying relation, whereby a gain in E_{pmax} of almost 10 times is achieved for an increase in laser intensity of approximately 20 times. From figure 5.9(a), where E_{pmax} is plotted as a function of laser energy, it is also clear that the absolute value of E_{pmax} increases with smaller laser focal spot size for constant laser pulse energy.

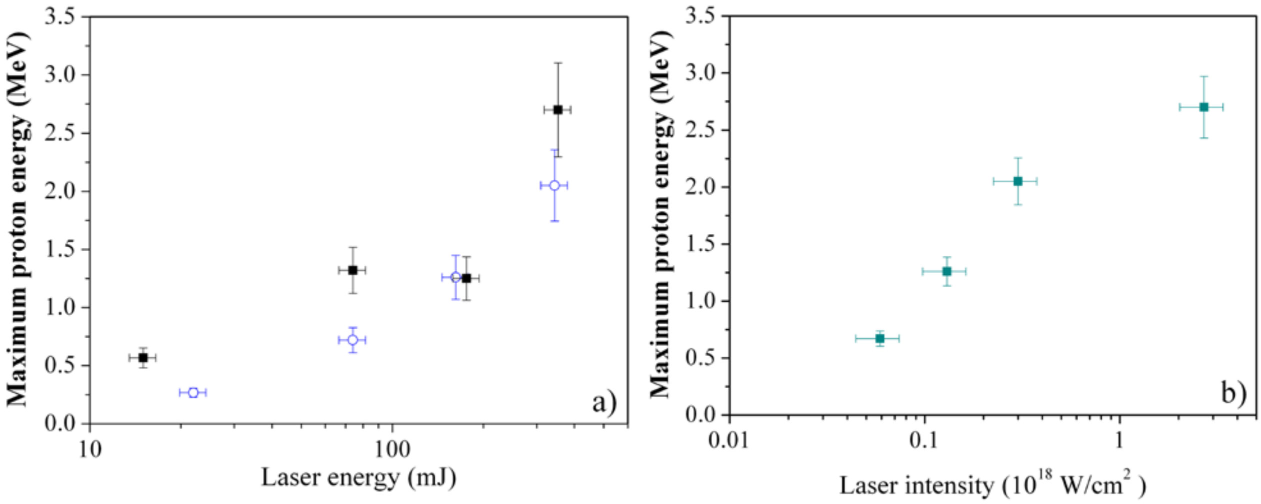

Figure 5.9: a) Maximum proton energy as a function of laser energy in the case of varying laser energy obtained with a laser focal spot size of 20 μm (black filled squares) and 60 μm (blue hollow circles) and b) Maximum proton energy as a function of laser intensity in the case of varying laser spot size, 20 μm to 140 μm, for a fixed laser energy.

For constant laser energy (see figure 5.9(b), a repeat of figure 5.5), the maximum proton energy increases more slowly, from 0.7 MeV up to 2.7 MeV, over an increase in the intensity of approximately 50 times when the focal spot size is varied, which is a weaker relation compared to when the laser energy is varied.

5.4.2. Discussion: dependence of maximum proton energy on laser energy and focal spot size

An interesting observation can be made of the scaling of the maximum proton energy with laser energy and focal spot size. Figure 5.3(c) demonstrates that the laser focal spot size is a factor in determining the maximum proton energy, but suggests that this is a weaker relation compared to the scaling of E_{pmax} with laser energy. The scaling relation for changing laser energy can be quantitatively described by making power fits to the data. Figure 5.8 shows how the scaling of E_{pmax} with laser energy increases as $I_L^{0.54\text{-}0.74\ \pm\ 0.10}$, whereby the upper value of the exponent represents the scaling obtained when using the larger of the two focal spot sizes (60 μm diameter).

Even taking into account the uncertainty in the exponent, the scaling relation for E_{pmax} with varying laser energy is quite different to that with laser focal spot size. The results reported here suggest that, for a given change in laser intensity, the maximum proton energy is twice as sensitive to a change in laser energy as it is to a change in laser focal spot size. It therefore seems imperative that scaling laws given in terms of intensity need to be accompanied with a definition of how the change in laser intensity is brought about.

A more promising approach to the origin of the scaling of maximum proton energy with laser energy can be found in the numerical work of Lefebvre *et al* [24] and the experimental work of Mordovanakis *et al* [25]. In both of these papers the temperature of a population of hot electrons produced by the laser interaction on the front surface of the target was investigated with respect to changes in laser intensity brought about by varying the laser energy. Lefebvre *et al* used a 2D PIC code to simulate the interaction of a 30 fs, pulse at 30° incidence with a 100 nm over-dense target, while Mordovanakis *et al* extracted the temperature of backward propagating hot electrons accelerated by the interaction of a 32 fs laser pulse at 45° incidence with a thick Al target. Both laser pulses were of moderate intensity (10^{17} – 10^{19} W/cm^2) and high contrast, which reflects the present experimental arrangement well. Interestingly, the results of Lefebvre *et al* and Mordovanakis *et al* are in very close agreement with the scaling presented here, with the former scaling as $I_L^{0.6}$ and the latter scaling as $I_L^{0.64}$.

An observed difference in the scaling of maximum proton energies, depending on whether one changes the laser energy or the focal spot size, has also been reported in analytical parametric investigations of target normal sheath accelerated proton beams carried out by Passoni *et al* [26] wherein ultra-short pulse (25 fs) interactions were investigated in the intensity range 10^{18}-10^{20} W/cm^2. Passoni *et al* used their theoretical model of target normal sheath acceleration [27] to predict values of E_{pmax} as a function of laser intensity in the interval 10^{18} – 10^{20} W/cm^2. The resultant scaling relations were found to be higher in the case of varying laser energy than in the case of varying laser pulse duration and/or focal spot size. It is not trivial to apply the absolute values of the exponent in the scaling relations reported in Passoni *et al*'s work to those reported here, since the Passoni *et al* scaling was derived from the interaction of a relatively low contrast laser pulse interacting with a thick target. However the underlying result that was obtained from comparing a change in laser energy to a change in focal spot size is similar and should also be considered in this discussion.

5.5. An analytical approach to modelling the laser-plasma interaction

5.5.1. Maximum proton energy, E_{pmax}, as a function of laser intensity, I_L

There have been many attempts at quantitatively describing the hot electron temperature and maximum proton energy in terms of laser intensity following the interaction of intense laser pulses with thin foils and the subsequent TNSA mechanism that is initiated. These include contributions from, among others, Mora [21] [28], Schreiber *et al* [4], Wilks *et al* [1] and more recently Passoni *et al* [26], Ziel *et al* [10] and Lefebvre *et al* [24]. Many of the descriptions have derived the maximum proton energy, E_{pmax}, as a function of the hot electron temperature, T_{hot}, whereas Shreiber *et al* derived E_{pmax} as a function of the laser power and the radius of the rear surface charge. Ziel *et al* used the Shreiber *et al* model to describe their experimental results and deduced that E_{pmax} scales linearly with laser power in the case of ultra-short laser pulses.

In previous scaling studies, the hot electron temperature and maximum proton energy have been presented as fitting a single trend line as a function of laser intensity however this is not an adequate approach to describe the trends in the data presented in this study wherein the intensity has been varied using both the laser energy and laser focal spot size as variables. It is very noticeable in figures 5.8 and 5.9(a) that the present experimental data cannot be fitted to one single trend line as a function of laser intensity. Figure 5.8 exemplifies this observation with the data points extracted at a laser intensity of approximately 1.3 × 10^{17} W/cm^2, for which there is a difference of a factor of 2; the reason for the difference being that the laser energy and laser focal spot sizes are different. Even when one presents the data points as a function of laser energy, as in figure 5.9(a), the trend lines are separated because of differences in the laser focal spot size. The data presented so far are leading to the conclusion that a simple scaling law for the relationship between E_{pmax} and laser intensity should be expressed in two forms that are dependent on whether one changes the laser intensity by varying the laser energy or by varying the laser focal spot size.

Even though Shreiber *et al* and Ziel *et al* incorporate the laser focal spot size into their derivation of E_{pmax} through the use of a reference time related to the protons in the vicinity of a surface charge, so far the analytical modelling used for TNSA has been developed for laser energy scaling at tight focus (< 10 μm) only. For ultra-thin targets the initial lateral extent of the hot electron population on the rear surface will be of the order of the laser focal spot size, in the absence of transport effects within the target and charge spreading on the surfaces. Therefore, defocusing the laser to larger spot sizes will give rise to a proportional increase in the lateral size of the hot electron source at the rear surface.

The effect of a large focal spot size in combination with ultra-thin targets will become relevant to the proton acceleration as one increases the focal spot radius, R_L, to the point at which the time taken for a relativistic electron travelling from the centre of the sheath on the rear surface with average velocity, $\bar{u}_e$, to reach the edge of the initial surface charge area is more than the laser pulse duration, τ_L:

$$\frac{R_L}{\bar{u}_e} > \tau_L \qquad (5.1)$$

For the experimental results presented here where ultra-thin foil targets have been employed, using T_{hot} ~ 100 keV as an estimate of the hot electron temperature at ~ 10^{18} W/cm^2 using the Lefebvre *et al* scaling and a laser pulse duration of 40 fs, the minimum diameter that satisfies this condition is ~ 14 μm which is smaller than the minimum spot size of 20 μm employed in the campaign. Therefore, it is believed that the inclusion of dimensional effects, owing to the initial lateral extension of the hot electron population on the rear surface of the target, by way of a modification to the acceleration time is necessary if one is to model the laser interaction under the conditions studied here.

It is worth noting that the validity of this approximation is limited to the case of large focal spot size irradiation of ultra-thin foils, whereby target thickness << focal spot size. Under these conditions, a uniform distribution of the hot electron population is a valid approximation for modelling the hot electron propagation from the front to the rear surface and the hot electron escape time will contribute significantly to the maximum proton energy obtainable. However, Coury *et al* [29] have demonstrated that in the case of defocused laser spot irradiation of thicker foils, where ballistic electron transport is approximated for diverging sources of hot electrons at the target front side, the resultant electron sheath distribution at the target rear surface is strongly peaked on the laser axis compared to tight focus.

5.5.2. Modelling the effect of a large focal spot size on the maximum proton energy

In light of the interesting results that have been presented here, it is useful to evaluate how the experimentally obtained values compare with those that can be deduced from an analytical study of laser-plasma interactions. For a simple, 1D description of sheath field generation and plasma expansion, one can make reference to the Mora isothermal model of ion acceleration [30] (see chapter 3). The maximum ion energy derived from this approach can be expressed as:

$$E_{pmax} \sim 2\, Z\, T_{hot}\, \left[\ln\left(\tau_{eff} + \sqrt{(1+\left(\tau_{eff}\right)^2}\right)\right]^2 \qquad (5.2)$$

where $\tau_{eff} = \frac{\omega_{pi}\tau_{acc}}{\sqrt{2\exp(1)}}$ with $\omega_{pi} = \sqrt{\frac{n_{hot}Ze^2}{m_i\varepsilon_0}}$ as the plasma ion frequency and τ_{acc} as the acceleration time.

The discrepancy between the two trend lines for the two different focal spot sizes observed here can be accounted for if one explores the properties in the sheath acceleration process that are directly relevant in determining the maximum proton energy as seen from the Mora equation; those being the hot electron temperature, T_{hot}, hot electron density, n_{hot}, (derived from the number of hot electrons, N_{hot}) and the acceleration time, t_{acc}. Here the acceleration time can be briefly described as being made up of the laser pulse duration, τ_L, with the addition of the time taken for significant expansion of the hot electron population to occur and for transfer of energy from the electrons to the protons to cease, $\tau_{transfer}$, as described by Robson *et al* [7] and Buffechoux *et al* [31]. Buffechoux *et al* [31] combined experimental results and simulation data over a wide range of parameters and found a simple relation to describe this time as being $\tau_{transfer} \sim 6\ \omega_{pi}^{-1}$. In order to incorporate the dimensional effects in the case of large defocused spot irradiation, a modification to the acceleration time, τ_{escape}, can be assigned as a function of the initial radius, R_L, and the average velocity of the hot electrons, $\bar{u}_e$:

$$t_{acc} \sim \sqrt{\tau_L^2 + \tau_{transfer}^2 + \left(\frac{R_L}{\bar{u}_e}\right)^2} \tag{5.3}$$

For the case of ultra-short laser pulse duration ($\tau_L < \sim 100$ fs), an increase in either T_{hot}, n_{hot} or τ_{acc} in isolation will lead to an increase in the maximum proton energy. Of the three hot electron sheath properties, T_{hot} will be the dominant contributor in determining the maximum proton energy and so there will always be a positive correlation between the two when one laser parameter is varied at a time, however the value of the exponent in the scaling relation will also be affected by changes in n_{hot} and τ_{acc}.

Using the modified definition of the acceleration time, along with the equations that follow, it is possible to examine how the sheath properties respond to an increase in laser intensity caused by either a change in laser energy at constant spot size or a change in laser focal spot size at constant laser energy. The Mora equation for maximum proton energy can then be used as a first approximation in order to determine the relative scaling in maximum proton energy one might expect as a result.

Total number of hot electrons, N_{hot}, and hot electron density, n_{hot}:

$$N_{hot} = \frac{\eta E_L}{T_{hot}} \text{ and } n_{hot} = \frac{N_{hot}}{\pi (R_L)^2\,(2\lambda_D + d_t)}\,,\ \lambda_D = \sqrt{\frac{\varepsilon_0 T_{hot}}{n_{hot} e^2}}$$

where η is the conversion efficiency of laser energy into hot electrons and λ_D is the Debye length of the electron sheath plasma. The effect of recirculation between the surfaces of the target has been incorporated by noting that the effective target thickness used to determine the hot electron density is equal to the initial target thickness with the addition of the lateral extension of the hot electron population (the Debye length) from both the front and rear target surface.

There are many studies that offer predictions, based on their numerical and experimental findings, of the hot electron temperature that can be calculated simply from the laser intensity. For this investigation the hot electron temperatures were calculated using the following scaling relations:

Lefebvre *et al* scaling [24]

$$T_{hot}\,(\text{keV}) = 126\left(\frac{I_L {\lambda_L}^2}{1.37\ x\ 10^{18}}\right)^{0.6}$$

Ponderomotive scaling [1]
$I_L > 1.6$ x 10^{18} W/cm^2

$$T_{hot}\,(\text{keV}) = \frac{m_e c^2}{1.6\ x\ 10^{-16}}\left[\sqrt{1 + \left(\frac{I_L {\lambda_L}^2}{1.37 \times 10^{18}}\right)} - 1\right]$$

Beg *et al* scaling [32]
$I_L < 10^{19}$ W/cm^2

$$T_{hot}\,(\text{keV}) = 0.215\ x\ 10^{-3}\left(I_L {\lambda_L}^2\right)^{\frac{1}{3}}$$

where I_L is the laser intensity in units of W/cm^2, λ_L is the laser wavelength in microns, m_e is the electron mass and c is the speed of light.

In the graphs that follow the Mora equation for maximum proton energy has been used along with the equations for T_{hot}, n_{hot} and τ_{acc} as given above with the input parameters being the values of laser intensity and laser energy used to obtain the experimental results with $\eta = 0.3$ and $\tau_L = 40$ fs.

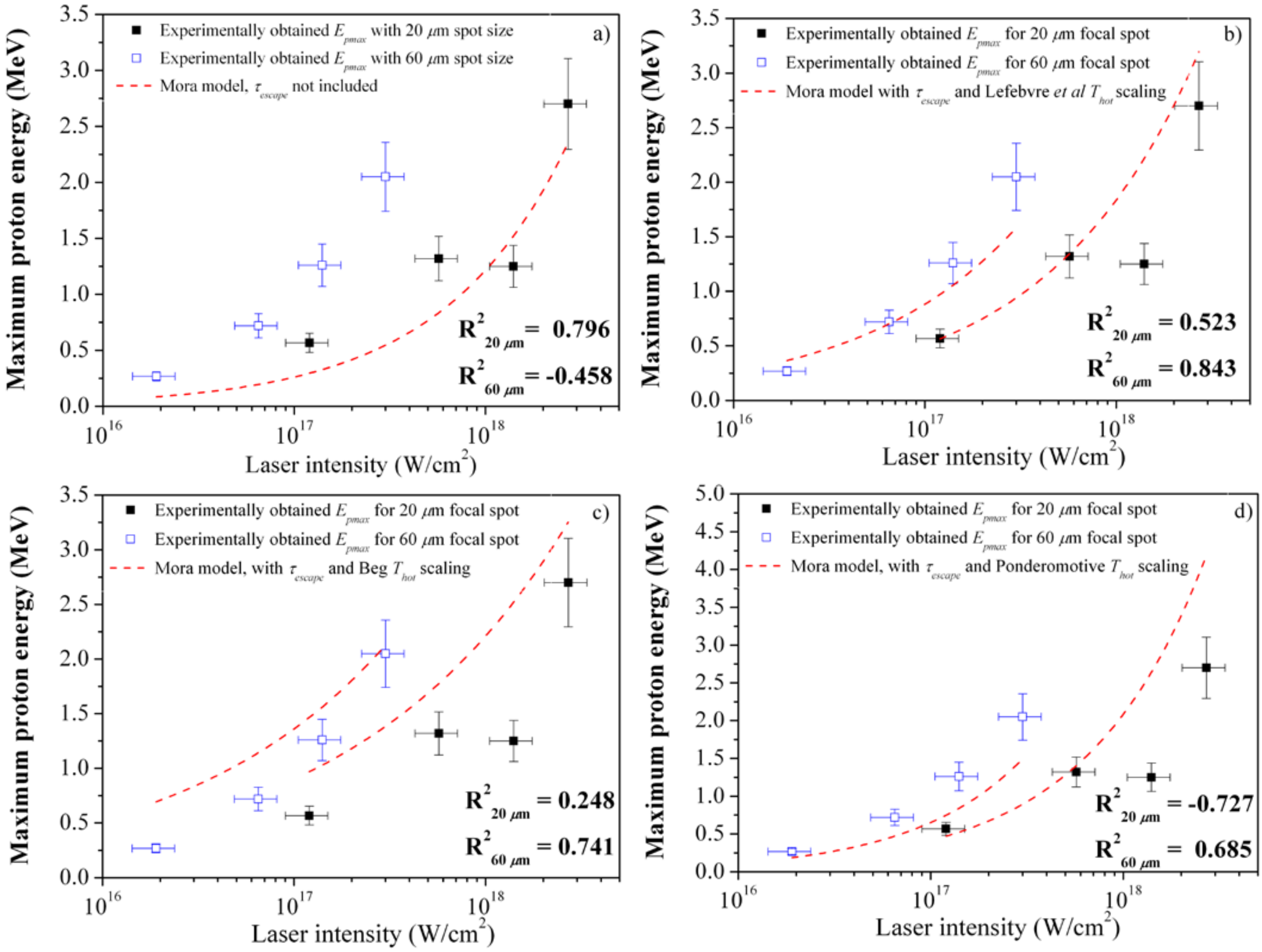

Figure 5.10(a-d): Experimentally obtained values of E_{pmax} plotted as a function of laser intensity compared to the values obtained by using a) the standard Mora model for ion acceleration and b) the modified version with T_{hot} given by the Lefebvre scaling and c) the Beg and d) Ponderomotive scalings.

Initially, the maximum proton energy was determined without the temporal modification using the Lefebvre relation for the hot electron temperature (see figure 5.10(a)). Despite appearances, the model actually predicts two trend lines for maximum proton energy as a function of laser intensity because of the different focal spot size. With the larger focal spot size (60 μm), the increase in effective τ_{acc} without the modification is small, ~ factor 3, whereas there is a ~ factor of 1.5 decrease in effective rear surface n_{hot}. Further still, the logarithmic dependence of

E_{pmax} with n_{hot} and τ_{acc}, compared to the direct correlation with T_{hot}, results in very little deviation between the trend lines, leading to an underestimate of the maximum proton energy achievable at the larger (60 μm) focal spot size when no temporal modification is considered. However, as figures 5.10(b-d) clearly demonstrate, by incorporating the escape time, τ_{escape}, into the equation for the acceleration time the model predicts two, resolvable trend lines for maximum proton energy as a function of laser intensity that can be associated with the two different focal spot sizes employed.

For an increase in laser energy at constant defocused spot size all of the variables, apart from $\tau_{escape,}$ will also increase. Whereas for a change in defocused spot size at constant laser energy the change in the parameters that contribute to the maximum proton energy is not as simply described, as the change in the focal spot size has a significant effect on both n_{hot} and τ_{escape}. For example increasing the focal spot size at constant laser energy will decrease T_{hot} and lead to a decrease in n_{hot}, despite an increase N_{hot}, while significantly increasing τ_{escape}. Varying the laser focal spot size is expected to result in a slower scaling relation compared to varying the laser energy as the effect on the acceleration time becomes important and therefore must also be considered in addition to the change in T_{hot}.

Figure 5.10 also provides a useful comparison of the effect on the model of using the three different T_{hot} scaling relations given above. The R^2 value is an indicator of how much of the variance of the modelled values is shared with the measured values with $R^2=1$ defining a perfect overlap between the two data sets. The ponderomotive scaling relation with laser intensity is commonly used to predict the hot electron temperature for relativistic laser plasma interactions at or very near to the critical surface, however figure 5.10(d) and a negative R^2 value suggests that it is also not a suitable description for the hot electron temperature under the conditions studied here. Both the Beg and Lefebvre *et al* scaling lead to a better approximation of the scaling of the measured values, particularly for the larger focal spot size. Figure 5.10(b) clearly demonstrates the Lefebvre *et al* scaling relation as being a suitable description of the hot electron temperature for the laser-plasma interaction conditions studied here. A high R^2 value of ~ 0.5-0.8 for both focal spot conditions indicates a close relationship between the modelled and experimentally obtained results. In addition to reproducing the T_{hot} scaling for the experimental results presented in this study, the Lefebvre relation can also be used to reproduce the absolute values of the experimental measurements of T_{hot} made by Mordovanakis et al [25] under very similar conditions to those employed here, indicating the high predictive ability of the 2D PIC simulations that were employed.

5.6. Conclusion and summary

The proton fluence data presented in this chapter is strongly dependent on the laser energy ($E_L{}^{2.1\pm0.3}$) and these findings are in agreement with the experimental data of others under a wide range of pulse durations and target parameters. This work points towards a method of controlling the proton dose delivered by a laser-driven proton beam through careful control of the laser energy and illumination conditions employed. This observation merits further investigation if we are to succeed in optimising laser driven ion acceleration for applications.

The maximum proton energies achieved appear to follow a slow scaling with laser intensity, in line with what is expected from a TNSA-driven system and as has been observed by other groups. When the laser energy is varied for a fixed laser spot size the maximum proton energy is observed to increase as $I_L{}^{0.54\text{-}0.74\pm0.1}$, with the dependence being weaker still when changing the focal spot size at fixed laser energy. The difference in scaling brought about by varying the different laser pulse properties is likely due to a modification in the acceleration time that becomes significant when operating with a defocused laser spot. A more suitable scaling law for the relationship between E_{pmax} and I_L would distinguish between the effect of changing laser energy, E_L, and laser focal spot radius, R_L. For example, for the data presented here under the interaction conditions of high laser contrast, moderate laser intensity, constant laser pulse duration and ultra-thin targets an appropriate scaling law might appear as:

$$E_{pmax}\left(f(T_{hot},\ n_{hot}), f(\tau_{acc})\right) \propto \begin{cases} I_L^{0.6}, varying\ E_L only \\ I_L^{0.3}, varying\ R_L only \end{cases}$$

Development of this function into a full predictive relation is beyond the scope of the present discussion, however it is a good illustration of the key findings of this study; namely that a model and scaling relation that can account for the effect of changes in both the laser energy and laser focal spot size explicitly is required to appropriately describe the TNSA process.

The investigation presented here sought to determine the scaling relation between the proton fluence and laser energy and how, or if, this relation is affected by laser spot geometry. In doing so, the need to differentiate between changes in laser intensity produced by either a change in laser energy or laser focal spot conditions has been highlighted, as evidently the two should not be combined under simple scaling laws. However it is hoped that based on the studies carried out here and by others, models can be developed with full predictive capability.

References

1. Wilks, SC, Langdon, AB, Cowan, TE et al. Energetic proton generation in ultra-intense laser--solid interactions. *Physics of Plasmas*, 8 (2001), 542.
2. Clark, EL, Krushelnick, K., Zepf, M. et al. Energetic heavy-ion and proton generation from ultraintense laser-plasma interactions with solids. *Physical review letters*, 85, 8 (2000), 1654--1657.
3. Allen, M., Sentoku, Y., Audebert, P. et al. Proton spectra from ultraintense laser--plasma interaction with thin foils: Experiments, theory, and simulation. *Physics of Plasmas*, 10 (2003), 3283.
4. Schreiber, J., Bell, F., Grüner, F. et al. Analytical model for ion acceleration by high-intensity laser pulses. *Physical review letters*, 97, 4 (2006), 45005.
5. Esirkepov, T., Yamagiwa, M., and Tajima, T. Laser ion-acceleration scaling laws seen in multiparametric particle-in-cell simulations. *Physical review letters*, 96, 10 (2006), 105001.
6. Fuchs, J., Antici, P., d'Humieres, E. et al. Laser-driven proton scaling laws and

new paths towards energy increase. *Nature Physics*, 2, 1 (2006), 48--54.

7. Robson, L., Simpson, PT, Clarke, RJ et al. Scaling of proton acceleration driven by petawatt-laser--plasma interactions. *Nature Physics*, 3, 1 (2007), 58--62.
8. McKenna, P., Ledingham, KWD, Spencer, I. et al. Characterization of multiterawatt laser-solid interactions for proton acceleration. *Review of scientific instruments*, 73 (2002), 4176.
9. Oishi, Y., Nayuki, T., Fujii, T. et al. Dependence on laser intensity and pulse duration in proton acceleration by irradiation of ultrashort laser pulses on a Cu foil target. *Physics of plasmas*, 12 (2005), 073102.
10. Zeil, K., Kraft, SD, Bock, S. et al. The scaling of proton energies in ultrashort pulse laser plasma acceleration. *New Journal of Physics*, 12 (2010), 045015.
11. Schnürer, M., Andreev, AA, Steinke, S. et al. Comparison of femtosecond laser-driven proton acceleration using nanometer and micrometer thick target foils. *Laser and Particle Beams*, 29, 4 (2011), 437.
12. Ziener, C., Foster, PS, Divall, EJ, Hooker, CJ, Hutchinson, MHR, Langley, AJ, and Neely, D. Specular reflectivity of plasma mirrors as a function of intensity, pulse duration, and angle of incidence. *Journal of applied physics*, 93 (2003), 768.
13. Sentoku, Y., Cowan, TE, Kemp, A., and Ruhl, H. High energy proton acceleration in interaction of short laser pulse with dense plasma target. *Physics of Plasmas*, 10 (2003), 2009.
14. Mackinnon, A.J., Sentoku, Y., Patel, PK et al. Enhancement of proton acceleration by hot-electron recirculation in thin foils irradiated by ultraintense laser pulses. *Physical review letters*, 88, 21 (2002), 215006.
15. Neely, D., Foster, P., Robinson, A. et al. Enhanced proton beams from ultrathin targets driven by high contrast laser pulses. *Applied physics letters*, 89 (2006), 021502.
16. Carroll, DC, Brummitt, P., Neely, D., Lindau, F., Lundh, O., Wahlström, C.G., and McKenna, P. A modified Thomson parabola spectrometer for high resolution multi-MeV ion measurements--Application to laser-driven ion acceleration.

Nuclear Instruments and Methods in Physics Research Section A: Accelerators, Spectrometers, Detectors and Associated Equipment, 620, 1 (2010), 23--27.

17. Green, JS, Borghesi, M., Brenner, CM et al. Scintillator-based ion beam profiler for diagnosing laser-accelerated ion beams. In *Proceedings of SPIE* (2011), 807919.
18. Green, JS, Carroll, DC, Brenner, C. et al. Enhanced proton flux in the MeV range by defocused laser irradiation. *New Journal of Physics*, 12 (2010), 085012.
19. Robinson, APL, Foster, P., Adams, D. et al. Spectral modification of laser-accelerated proton beams by self-generated magnetic fields. *New Journal of Physics*, 11 (2009), 083018.
20. McKenna, P., Carroll, DC, Lundh, O. et al. Effects of front surface plasma expansion on proton acceleration in ultraintense laser irradiation of foil targets. *Laser and Particle Beams*, 26 (2008), 591--596.
21. Mora, P. Plasma expansion into a vacuum. *Physical review letters*, 90, 18 (2003), 185002.
22. Pirozhkov, AS, Choi, IW, Sung, JH et al. Diagnostic of laser contrast using target reflectivity. *Applied Physics Letters*, 94 (2009), 241102.
23. Streeter, MJV, Foster, PS, Cameron, FH et al. Relativistic plasma surfaces as an efficient second harmonic generator. *New Journal of Physics*, 13 (2011), 023041.
24. Lefebvre, E., Gremillet, L., Lévy, A. et al. Proton acceleration by moderately relativistic laser pulses interacting with solid density targets. *New Journal of Physics*, 12 (2010), 045017.
25. Mordovanakis, A.G., Masson-Laborde, P.E., Easter, J. et al. Temperature scaling of hot electrons produced by a tightly focused relativistic-intensity laser at 0.5 kHz repetition rate. *Applied Physics Letters*, 96, 7 (2010), 071109--071109.
26. Passoni, M., Bertagna, L., and Zani, A. Energetic ions from next generation ultraintense ultrashort lasers: Scaling laws for Target Normal Sheath Acceleration. *Nuclear Instruments and Methods in Physics Research Section A: Accelerators, Spectrometers, Detectors and Associated Equipment*, 620, 1 (2010), 46--50.

27. Passoni, M. and Lontano, M. Theory of light-ion acceleration driven by a strong charge separation. *Physical review letters*, 101, 11 (2008), 115001.
28. Mora, P. Thin-foil expansion into a vacuum. *Physical Review E*, 72, 5 (2005), 056401.
29. Coury, M., Carroll, DC, Robinson, APL et al. Influence of laser irradiated spot size on energetic electron injection and proton acceleration in foil targets. *Applied Physics Letters*, 100, 7 (2012), 074105--074105.
30. Mora, P. Plasma expansion into a vacuum. *Physical review letters*, 90, 18 (2003), 185002.
31. Buffechoux, S., Psikal, J., Nakatsutsumi, M. et al. Hot Electrons Transverse Refluxing in Ultraintense Laser-Solid Interactions. *Physical review letters*, 105, 1 (2010), 15005.
32. Beg, FN, Bell, AR, Dangor, AE et al. A study of picosecond laser-solid interactions up to 1019 W cm-2. *Physics of Plasmas*, 4, 2 (1996), 447--457.

Chapter 6: 1D simulations of a moderately intense laser plasma interaction

In this chapter, a 1D particle-in-cell code is employed to simulate the interaction of an ultra short, moderately intense laser pulse with a thin film target in order to investigate the scaling results presented in chapter 5. Realistic hot electron temperatures, compared with those measured under similar interactions, are predicted by the code, with the scaling of the values obtained with a step-life density profile in very good agreement. However, a disparity between the measured and simulated proton beam properties as a function of intensity is observed. The absorption fraction modelled in the 1D simulations is therefore investigated to explore this interesting result.

6.1. Simulating laser driven ion acceleration using a PIC code

In light of the interesting results presented in chapter 5 of the scaling of total flux and maximum energy of sheath accelerated protons as a function of laser intensity at constant focal spot size, a 1D PIC code (see chapter 4.5) was used to simulate the interaction of a 40 fs laser pulse with a 25 nm-thick, CH (parylene) film target in an attempt to investigate the underlying physics. Away from a best focus position, the laser spot loses its characteristic Gaussian profile and the intensity of laser light initially becomes much more uniform across the irradiated area. Defocusing to large areas will eventually introduce significant modulations. Furthermore, the use of an ultra-thin target foil, whereby the target thickness << focal spot size means that a uniform distribution for the cross-section of the hot electron population is a valid approximation for modelling the hot electron propagation from the front to the rear surface. The laser-plasma interactions at the front surface in this case can therefore be approximated as being 1D natured, in that the experiment was not conducted using a tightly focussed beam. The results presented in chapter 5 on the scaling of the proton flux with laser intensity also indicate that the total proton number is primarily driven by the laser energy absorbed at the front surface. It is therefore considered appropriate to model the interaction using a 1D simulation in order to conduct an initial investigation into the effect on the hot electron population and subsequently the accelerated proton population in the intensity regime of 10^{16}-10^{19} W/cm^2.

6.2. Proton spectra obtained with varying laser intensity

A convenient and computationally efficient version of an explicit 1D3P PIC code [1] that can be run on a single desktop PC node was employed in this study. A series of simulations were initiated using input files that were built upon a grid of size 72 μm, comprised of 125000 cells of width 0.4 nm. The 25 nm-thick Parylene (C_8H_8) target was comprised of a uniform distribution of C^{3+} ions and protons, giving rise to an initial electron density of ~ 120 n_{crit}. A step-like density gradient on the front surface was initially employed to reflect the high contrast laser conditions of the experiment.

To simulate the laser pulse the code uses an input file describing the electric field in the spatial grid at *t* = 0 that has been created by defining the amplitude of the electric vector potential, a_0, the laser pulse duration and the laser wavelength. The laser intensity region of interest was chosen to include the values used in the experimental campaign described in chapter 5 and extended up to ~ 1×10^{19} W/cm^2 to observe the transition into the relativistic ($a_o \geq 1$) regime. The laser intensity values for a laser of wavelength 800 nm were defined in terms of a_o given by:

$$a_0 = \frac{eE_0}{\omega_L m_e c} = \sqrt{\frac{I_L \lambda_L^2}{1.37 \times 10^{18}}} \tag{6.1}$$

in which the laser intensity, I_L, is calculated in units of W/cm^2 and the wavelength of the laser, λ_L, is given in units of μm. In order to be able to resolve the Debye length over cells of width 0.4 nm the simulation was initiated with an electron temperature of 2 keV. The target was placed at the foot of the rising edge of the laser pulse at *t* = 0, to ensure that the laser interacted with a sharp edged plasma profile.

Proton spectra were obtained at a time of 300 fs into the simulation, which is 260 fs after the peak of the pulse interacts with the front surface. Beyond *t* = 300 fs there was a marked decrease in the gradient of increasing maximum proton energy as a function of time, signifying a decrease in the rate of energy transfer to the protons and the onset of numerical heating. Using protons travelling away from the rear surface only, the kinetic energy of each proton macro particle is extracted and a proton spectrum is produced by plotting the number of macro particles within a certain energy-bin as a function of proton energy, $\frac{dN_p(E_p)}{dE_p}$. An example set of simulated spectra can be found in figure 6.2 alongside the experimentally measured spectra obtained at equivalent laser intensities.

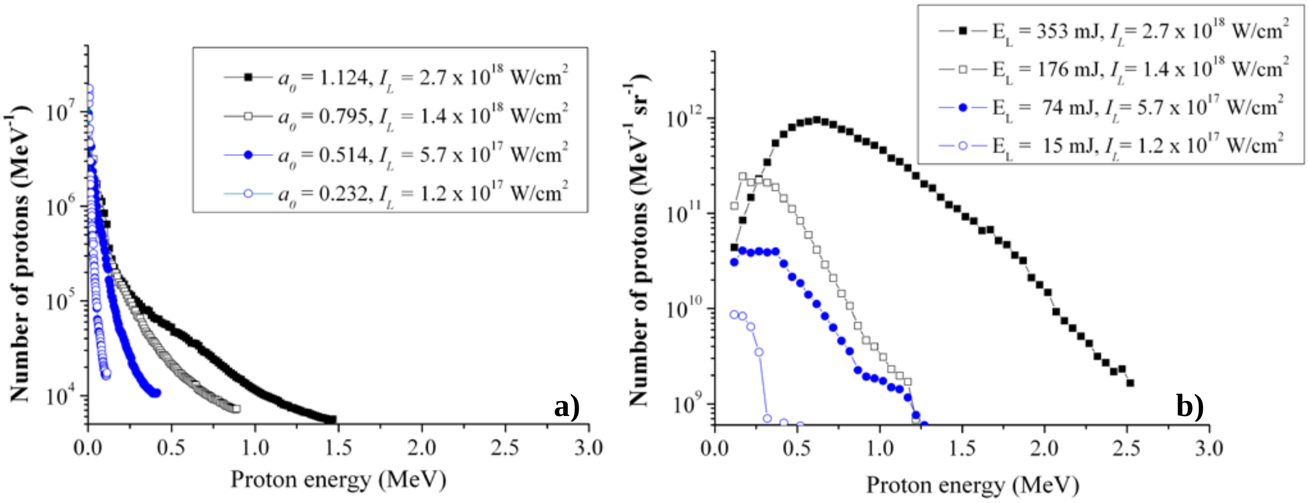

Figure 6.1: a) Simulated and b) measured proton energy spectra for values of laser intensity that are equivalent to those used in chapter 5.

6.2.1. Comparison of 1D PIC simulation with experimental results

The spectra presented in figure 6.1 demonstrate how the code has predicted an exponentially decreasing spectrum as a function of proton energy and that the maximum energy calculated by the code and slope of the spectra change with laser intensity. However on closer inspection, a comparison between the features of the numerical and experimental proton spectra suggests that the simulations have not fully reproduced the conditions for proton acceleration that were achieved in the experiment. For example, the measured maximum proton energies are all higher for the various laser intensities than those predicted in the simulated data. Despite a difference in the absolute values between the simulation and measured maximum proton energies, it is still useful to examine the laser intensity dependencies of the proton beam parameters predicted by the code.

The simulated proton number flux and maximum proton energy have been plotted with respect to laser intensity in figure 6.2. For an appropriate comparison with the measured values, only proton macro particles with kinetic energy more than 150 keV have been included in the values for proton number flux, as this was the minimum detectable proton energy of the diagnostic used in the experiment. Using the results of chapter 5 the scaling of the numerically predicted values of maximum proton energy and proton number flux with laser intensity can be compared to the scaling of the experimental values.

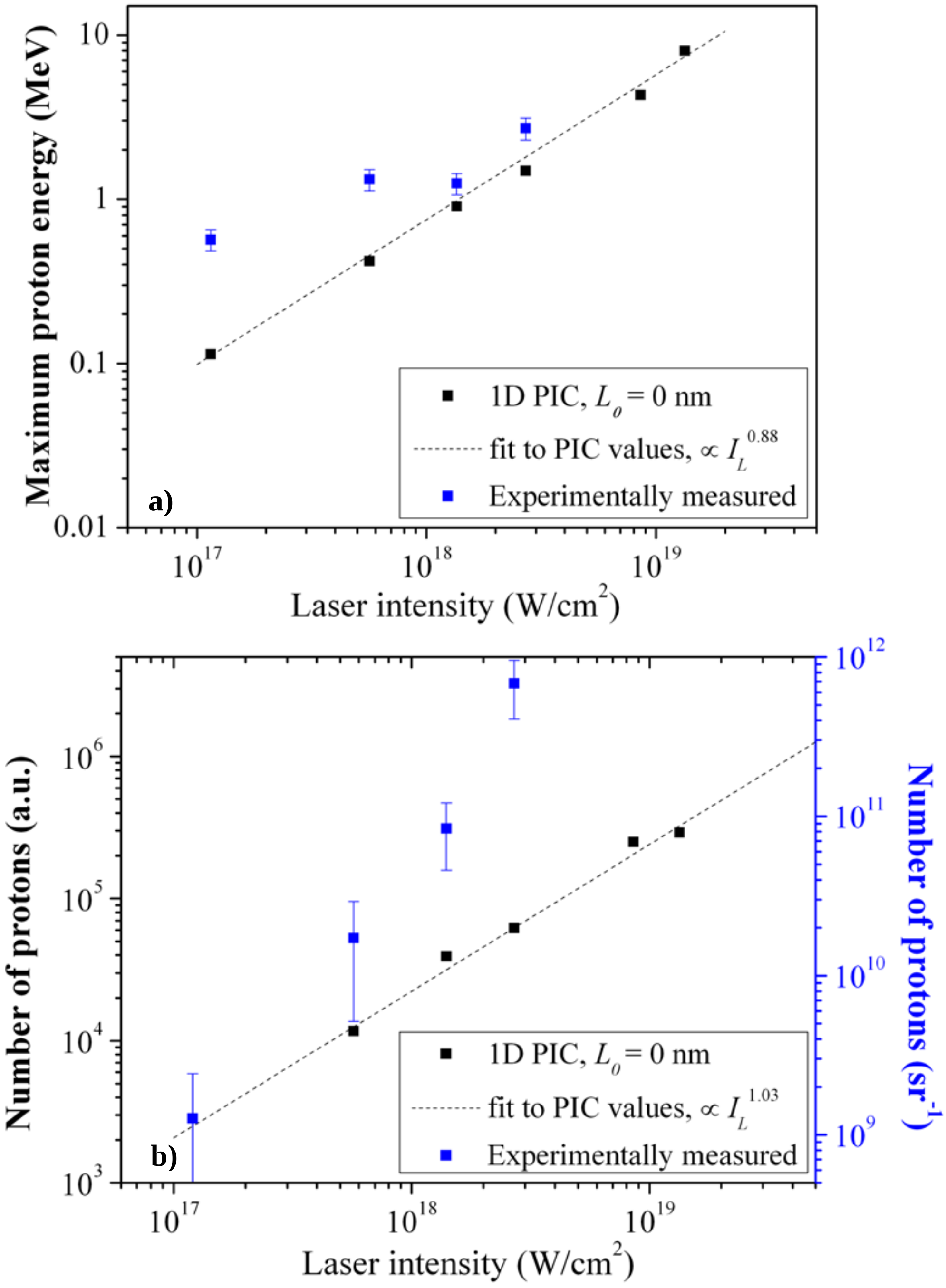

Figure 6.2: a) Maximum proton energy and b) total number of protons with energy more than 0.12 MeV plotted as a function of laser intensity for experimentally and numerically obtained proton spectra.

The simulated maximum proton energy values lie close to the measured values for laser intensities above 1 × 10^{18} W/cm^2, while the scaling of the values across the intensity range is faster, increasing as ~ $I_L^{0.9}$, when compared to the measured trend which increases as $I_L^{0.6 \pm 0.1}$. There are two possible interpretations that arise from making this comparison: 1) the hot electron escape time (see chapter 5), which is a 2D effect, becomes significant at laser intensities below 10^{18} W/cm^2 and therefore the measured values are expected to be above the simulated results which cannot incorporate this effect, or 2) the hot electron temperatures or densities in the simulation are incorrect. The first interpretation would support the findings of chapter 5 of the significance of the hot electron escape time in determining the maximum proton energy at large focal spot diameters. The second interpretation is discussed in more detail in section 6.2.3.

The increase in the simulated proton number flux with laser intensity is slow relative to the experimental observation, scaling as ~ $I_L^{1.0}$ compared to a measured scaling of $I_L^{2.1 \pm 0.3}$ (varying laser energy). It is interesting that the code has not predicted a similar scaling of the flux with laser intensity. A key conclusion of the experimental scaling in chapter 5 is that the combination of constant absorption fraction and a slow scaling of the hot electron temperature with laser intensity, leads to a fast scaling of the proton number with laser energy. In the 1D simulation the pulse duration and focus are fixed and therefore the pulse energy varies directly with laser intensity. One might therefore expect a similar result for the measured and simulated proton number flux scaling. By neglecting collisions and energy loss due to lateral motion, the dimensional restrictions imparted by working in 1D imply that maximum transfer of the energy carried away by the hot electrons from the interaction on the front surface to the accelerated protons is expected. It is therefore required that the laser energy absorption fraction as a function of laser intensity is examined for the simulated interactions (see section 6.2.3).

6.2.2. Introduction of an ultra-short plasma scale length at the target front surface

The experiment described in chapter 5 was designed so that plasma expansion did not occur until the main pulse interaction. Therefore, a step-like density gradient was initially employed in order to replicate experimental conditions. However, in an attempt to reproduce the experimentally obtained spectra, a series of simulations were carried out with the inclusion of an ultra-short plasma density ramp on the front surface. A plasma density scale length of $L_0 = \lambda_L/8$ was chosen as this is still considered to be short compared to the wavelength, thus imitating a high contrast laser interaction. The scaling of the proton beam properties with laser intensity was then revisited. In order to compensate for multi dimensional absorption processes that the code cannot replicate, such as resonance absorption for example (see chapter 2), it is common for 1D simulations to be initiated with a plasma density scale length profile, part of which will include an under-dense region, on the front surface to result in better coupling of the laser light into the fully ionized medium.

As before, the code was used to simulate the interaction of a 40 fs, 800 nm laser pulse with a 25 nm-thick CH target foil at solid density (~ 120 n_{crit}). The grid was of size 72 μm, comprised of 125000 cells, and the plasma density was modelled as rising exponentially, with a scale length of 100 nm at the front surface of the target. The resultant spectra for intensity values matched to those used in the experiment (figure 6.2), extracted 300 fs into the simulation, can be seen in figure 6.3.

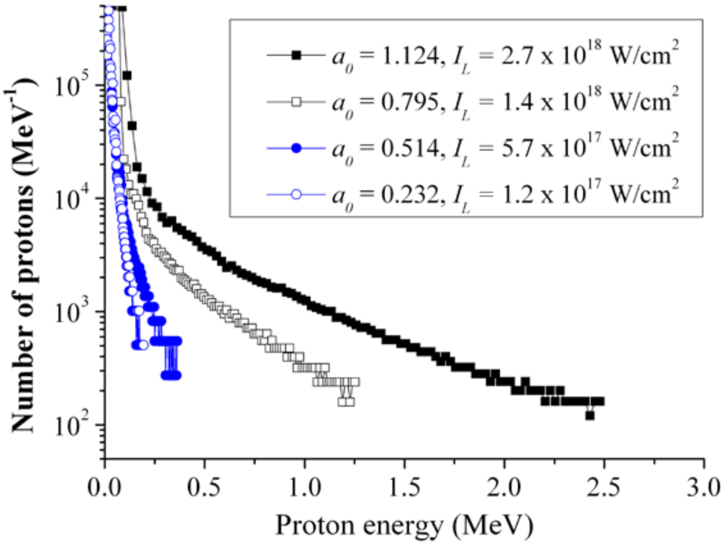

Figure 6.3: Simulated proton energy spectra for values of a_0 that are equivalent to those in chapter 5, with the inclusion of an exponential plasma density ramp of scale length $\lambda_L/8$.

With the implementation of a short density scale length on the front surface, the measured maximum proton energies for a laser intensity more than 1 × 10^{18} W/cm^2 have been reproduced by the PIC code. The maximum proton energy at lower intensities has again been underestimated. It is also noticeable that the number of (macro particle) protons in the spectra above are considerably lower (at least an order of magnitude decrease across the whole spectrum) as compared to the simulated spectra obtained with a step-like density gradient. In order to explain this result, it is worth recalling the 1D plasma expansion model described by Mora [2], in which the maximum proton energy, E_{pmax}, was found to be a function of hot electron temperature, T_{hot}, density, n_{hot}, and acceleration time, τ_{acc}.

$$E_{pmax} = 2Zk_BT_{hot}\left[\ln\left(\tau + \sqrt{\tau^2 + 1}\right)\right]^2 \tag{6.2}$$

where $\tau = \frac{\omega_{pi}\tau_{acc}}{2\exp(1)}$ is the acceleration time, τ_{acc}, normalised to the ion plasma frequency, $\omega_{pi} = \sqrt{\frac{Zn_{hot}e^2}{\varepsilon_o m_i}}$. While the maximum proton energy is linearly dependent on the hot electron temperature, it has a weaker dependence on hot electron density in comparison, whereas the number of protons is directly correlated to the hot electron density [2].

The decrease in proton numbers, while maintaining realistic values of maximum energy, is therefore likely to be caused by a decrease in the hot electron density, which is a result of the thickness of plasma above the critical density, and therefore effective target thickness, substantially increasing when a pre-plasma density profile is implemented. Electron refluxing (see chapter 2) is expected to occur under the conditions simulated here; an increase in the target thickness leads to a longer time between reflections between the two surfaces, therefore resulting in a lower effective electron density at the rear surface compared to a thinner foil.

Despite the reduction in electron circulation, the increased maximum proton energies for laser intensity above 1×10^{18} W/cm^2 compared to the step-like profile case suggests that the simulated hot electron populations have been enhanced. Considering that the proton numbers in figure 6.3 suggest that the electron density has been reduced in the scale length density profile simulations, this indicates that the hot electron temperature is the enhanced parameter compared to the step-like density simulations. Plotting the simulated results as a function of the laser intensity (figure 6.4) reveals that the scaling of simulated maximum proton energy with laser intensity is similar to that observed with the step-like density profile. Whereas, the scaling of the proton number with laser intensity is marginally faster than with the step-like profile, increasing as $\sim I_L^{1.1}$. It is also interesting to note that not all of the simulated data points are reproduced exactly by the trend line, which suggests that scaling of hot electron parameters with laser intensity in these simulations is not simply described with a single scaling.

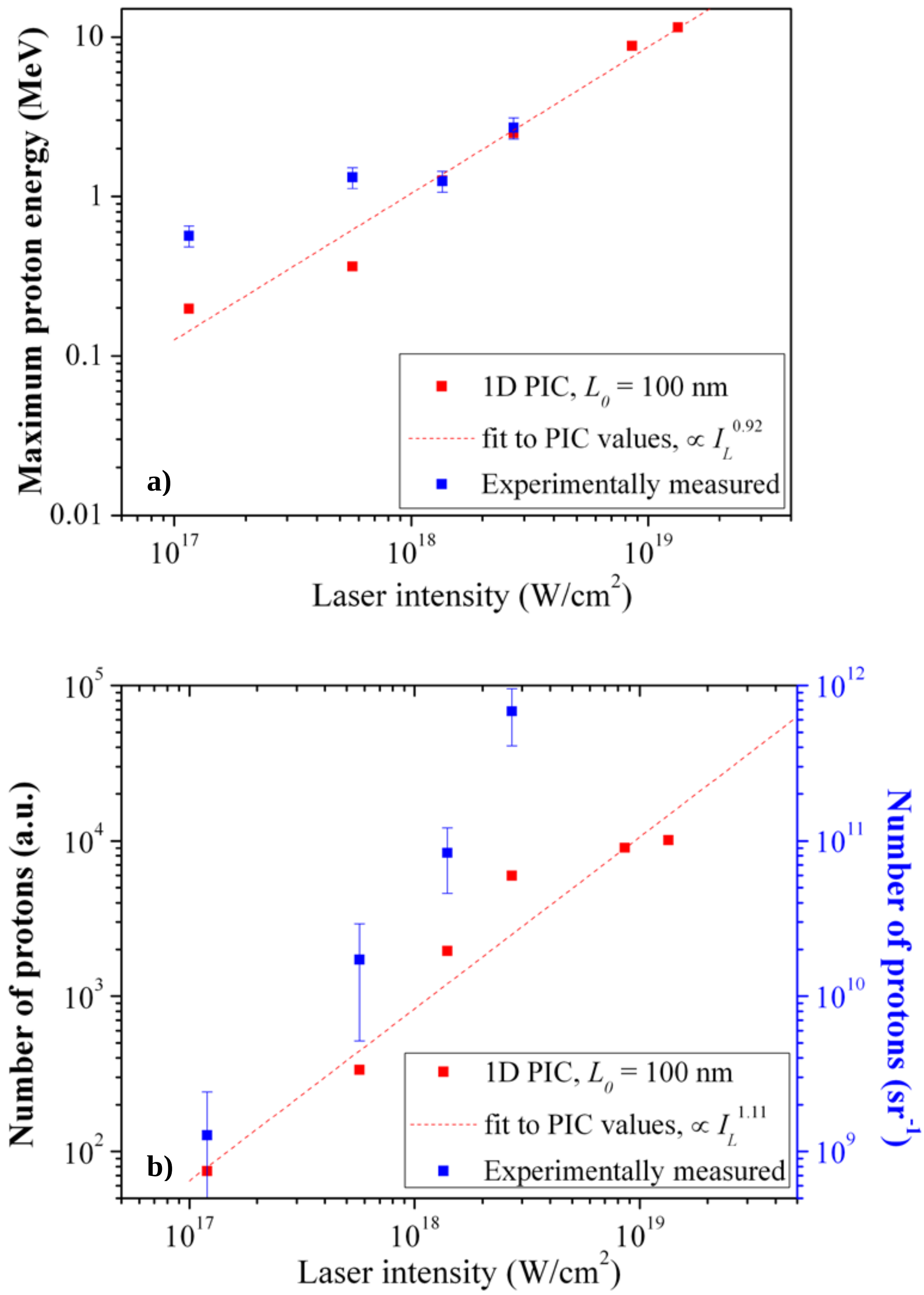

Figure 6.4: a) Maximum proton energy and b) total number of protons with energy more than 0.12 MeV plotted as a function of laser intensity for experimentally and numerically obtained proton spectra with the inclusion of an exponential plasma density ramp of scale length $\lambda_L/8$.

6.2.3. Simulated laser-plasma absorption and hot electron temperature as a function of laser intensity

To understand the significant differences identified between the simulated and the measured proton beam values, and even between the simulations with different front surface density profiles, further investigation into the parameters of the simulated interaction is required. The absorbed fraction of the laser pulse energy and the hot electron temperature parameters directly result from the interaction at the front surface and are key parameters to monitor, especially as they can easily be compared to experimental values under very similar conditions.

The energy density, u, of the laser pulse was calculated by integrating the Poynting vector of the propagating laser fields across the grid with cell width, dx, these being the E_y and B_z components of the electric and magnetic field respectively.

$$u = \int \frac{1}{2}\left(\varepsilon_0 \left|E_y\right|^2 + \frac{1}{\mu_0}\left|B_z\right|^2\right) dx \tag{6.3}$$

The absorbed fraction of the laser pulse energy into the plasma can be extracted by comparing this value at time t_0, where t_0 corresponds to the start of the simulation, to the value extracted after the wave had reflected from the front surface of the target and had propagated a distance away from the target, at time t = 110 fs. Figure 6.5 shows energy absorption into the plasma for the different density profiles used in the simulations as a function of laser intensity, I_L, alongside experimental values [3] measured under similar interaction conditions for comparison.

In work first published by Pirozkov *et al* [4] the Astra laser pulse (40 fs, 800 nm) was employed in conjunction with a single plasma mirror to produce high contrast laser pulses for interaction with thin (50 nm) target foils. The specular reflectivity from the front surface of the target was monitored as a function of laser intensity under high contrast interaction conditions and then compared to measurements made under low contrast conditions. It was found that when a high contrast laser pulse was used, the reflectivity remained high and approximately constant at around 70 % across two orders of magnitude of laser intensity, in the region 1 x 10^{17} – 1.5 x 10^{19}

W/cm^2. This result was reproduced by the experimental investigations of Streeter *et al* [3] in which the Astra Gemini laser, which has the same front end as the Astra laser, was employed in conjunction with a double plasma mirror system, to produce ultra-high contrast laser pulses for interaction with 100 nm foil targets. Streeter *et al* also extended the laser range from 10^{17} – 10^{21} W/cm^2 whilst measuring the total specular reflectivity (both ω_0 and $2\omega_0$ components) and found that even at laser intensities above 10^{19} W/cm^2, the reflectivity only decreased by 8% across the broad intensity range.

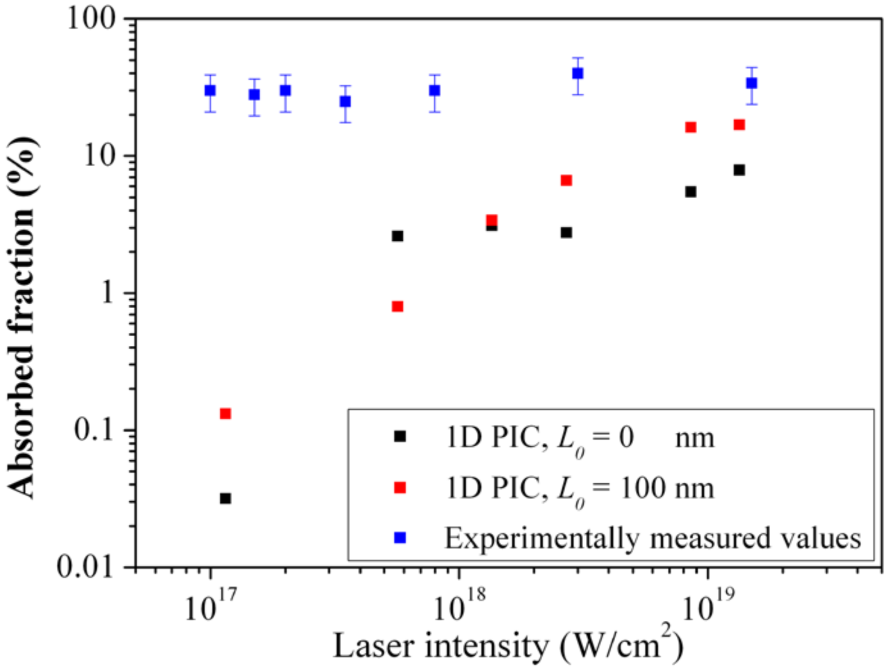

Figure 6.5: Laser pulse absorption at the front surface of the target plotted as a function of laser intensity. Experimental measurements made using similar conditions are shown for comparison [3]**.**

As is clearly evident in figure 6.5, the simulated total absorption values are well below that of the experimental values. For the step-like density profile simulations, the absorption fraction is ~ 3% for laser intensities around 10^{18} W/cm^2 before increasing up to ~ 8% with higher intensity. While the introduction of an exponentially increasing density gradient does seem to encourage slightly more of the laser to be absorbed, giving ~ 11% for I_L ~ 10^{19} W/cm^2, the absorbed fraction increases considerably with increasing laser intensity across the entire range which is different to the experimental observation.

There are two ways in which this will affect the sheath acceleration physics at the target rear surface modelled by the code. Firstly, a lower-than-expected absorbed fraction indicates that the code might not be able to correctly predict the number and average energy of the hot electrons and thus the hot electron density at the target rear surface. For a 1D model of plasma expansion [2], the sheath field generated by a population of hot electrons that reach the target rear surface is a function of both the hot electron temperature and density (see equation 6.2). A lower value of either of these parameters leads to a weaker sheath field and thus lower energy protons. Secondly, the fact that that the simulated absorption fraction changes with laser intensity implies that the amount of energy transferred to the hot electron population at the front surface will not be a linear function of the energy density of the incoming laser pulse, as is the case experimentally. Therefore, the simulated scaling of the electron density with laser intensity will differ from the experimental scaling and will thus result in a different scaling of the proton beam parameters.

In order to decipher how the hot electron population is affected by the low and varying laser absorption fraction, it is useful to examine how the hot electron temperature is changing as a function of laser intensity and compare this to the scaling measured directly under similar interaction conditions in the experimental work of Mordovankis *et al* [5] (see figure 6.6). When plotting the simulated electron spectra, dual-temperature electron populations were observed; made up of a high number of electrons at temperature T_{cold} and an exponentially decaying tail with temperature T_{hot}. A Maxwell-Boltzmann temperature for the hot electron population, $k_B T_{hot}$, was extracted by calculating the average kinetic energy, $<KE_e>$, of electrons in the high energy tail of the spectrum and using:

$$k_B T_{hot} = \frac{2}{3} < KE_e > \tag{6.4}$$

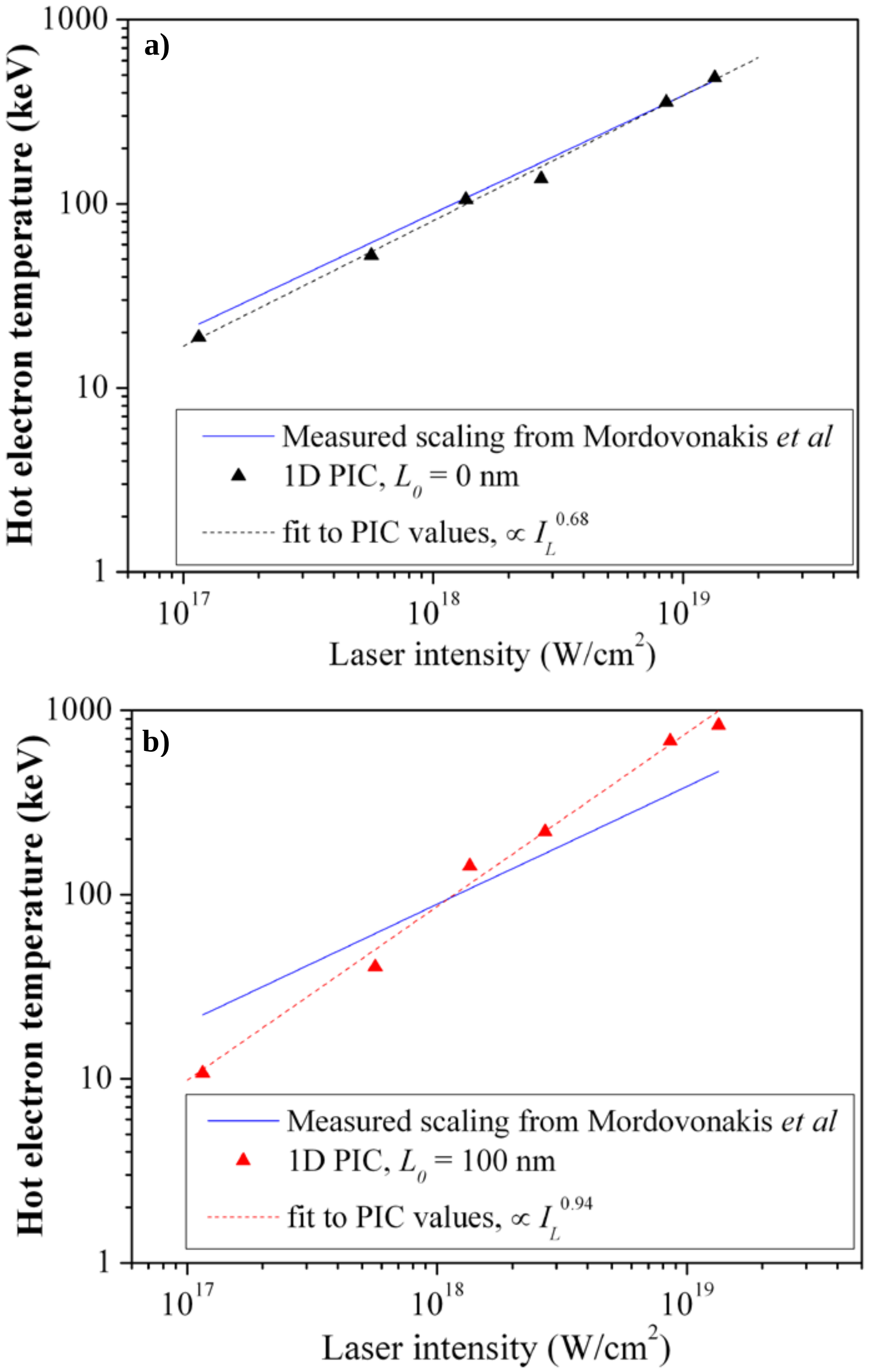

Figure 6.6: Expected values of hot electron temperature taken from experimental results of Mordovanakis *et al* as a function of laser intensity [5] **compared to the hot electron temperature simulated by the code using a) a step-like density profile on the front surface and b) an exponentially rising profile with scale length $L_0 = \lambda_L/8$.**

For the step-like density profile, the hot electron temperatures given by the simulated data are in close agreement with the values measured experimentally by Mordovonakis *et al.* while For the lowest intensities simulated the code slightly underestimates the absolute values for the hot electron temperature, whereas for intensities beyond 10^{19} W/cm^2 the simulation predicts the measured value, which is likely to be due to the fact that the simulated absorption fraction is approaching 10 % in this intensity region. The scaling across the intensity range explored indicates that the hot electron temperature increases as ~ $I_L^{0.7}$ which is in good agreement with the Mordovonakis *et al* scaling of ~ $I_L^{0.64}$ [5].

As with the proton beam properties explored earlier, the hot electron temperature values as given by the exponential density profile simulations show more deviation from the trend line that has been fit to the data range. Only for laser intensities at around 10^{18} W/cm^2 is the code shown to almost reproduce the measured values of hot electron temperature. The simulated values are shown to scale faster than for the step-like profile case, increasing with laser intensity as ~ $I_L^{0.9}$ which is not a good representation of what has been measured experimentally under conditions of high contrast laser irradiation. It is possible that the hot electron temperature scaling has not been well predicted by the code in this case due to the laser energy absorbed into the plasma being modelled as a stronger function of laser intensity (absorbed fraction increasing with I_L) than experimentally measured (absorbed fraction constant with increasing I_L). It could also be that the absorption mechanisms that give rise to the measured hot electron temperature scaling are not being fully modelled when the scale length density profile is included, as discussed below.

6.3. Discussion

In search of the underlying reason for the difference in the scaling of the measured proton beam parameters and the simulated proton beam parameters, it is found that the simulated absorption fraction as a function of laser intensity does not agree with the measured trend. For an ultra-short laser pulse interacting with an over-dense target, the laser energy can be absorbed into the plasma via processes such as resonance absorption, vacuum heating, $\boldsymbol{j} \times \boldsymbol{B}$ heating or by surface affects such as the anomalous skin effect and sheath inverse bremsstrahlung. In the 1D3V PIC simulations used in this study, resonance and vacuum absorption are not incorporated as these processes rely on there being a component of the electric acting parallel to the density gradient to directly drive longitudinal oscillations. However the inclusion of a multi-dimensional momentum space means that the $\boldsymbol{j} \times \boldsymbol{B}$ mechanism can be modelled effectively. An external field acting in the y direction, E_y, on surface electrons will result in a v_y component which in turn results in a Lorentz force component acting along the x direction, $F_x = -qv_yB_z$. Sheath inverse bremsstrahlung [6] [7] is a collision-less absorption process that occurs when a surface electron within the laser skin depth is driven by the laser field and then reflected from a sheath field at the vacuum-plasma interface. The energy transfer between the laser and the electron is thus one way resulting in net energy gain by the electron. In early work presented by Lefebvre and Bonnaud [8] 1.5D PIC simulations were used to demonstrate that surface absorption mechanisms were effective in the case of step-like density profiles with normal incidence and moderate laser intensities ($a_0 << 1$), leading to a low absorption of < 10% which is in good agreement with the simulation results reported here. For exponentially rising density profiles, they also observed a contribution to the absorption made by a small amount of volume heating that exists where the laser penetrates up to the critical density and the incoming and reflected waves form a standing wave. In the absence of angular-dependent absorption mechanisms and 2D/3D ion motion, the absorption fraction is therefore not fully reproduced by the 1D3V numerical model at the laser intensities explored here. It is also worth considering that at low intensities ($I_L \sim 10^{16}$ W/cm^2) the contribution of collisional mechanisms to the absorption fraction might also need to be included, as noted by Ping *et al* [9] .

Hence for the step-like density profile simulations conducted here, whereby only surface absorption mechanisms are effective, the absorption fraction will begin to increase with laser irradiance as soon as the ponderomotive $\boldsymbol{j} \times \boldsymbol{B}$ motion becomes dominant over the sheath inverse bremmstrahlung mechanism, shown here to occur at the expected value of I_L ~ 10^{18} W/cm^2. Whereas for the scale length density simulations the addition of a small amount of volume heating, which has an intensity dependent absorption rate, in combination with the surface mechanisms that are effective means that the absorption fraction increases across the entire intensity range.

Despite the small number of absorption processes included in the PIC code employed in this study, realistic hot electron temperatures were predicted for the case of a step-like density profile and furthermore their scaling with laser intensity was in close agreement with the scaling measured experimentally under similar short pulse, high contrast laser conditions [5]. It is interesting to note that in the step-like density profile case for the three laser intensities at which the absorption is roughly constant at ~ 3%, the hot electron temperature scales as ~ $I_L^{0.6}$. This is in very good agreement with the measured scaling and supports the choice of hot electron scaling employed in the 1D plasma expansion model used at the end of chapter 5.

6.4. Summary

The study presented here made use of a computationally efficient 1D3V PIC code to simulate the interaction of an ultra-short, moderate intensity, high contrast laser pulse with an ultra-thin target. The scaling of the proton beam parameters, maximum proton energy and number of protons (with energy more than 120 keV), are investigated with respect to laser intensity and compared to the measurements made in chapter 5. For both 1) a step-like density profile and 2) an ultra-short scale length density profile, the numerical model did not full reproduce the beam properties observed experimentally. Therefore the scaling of the hot electron temperature and absorption fraction were also investigated with respect to laser intensity.

For the case of a step-like density profile, the code predicts a scaling for the hot electron temperature with laser intensity which is in close agreement with the experimental measurements. However, the inferred number of hot electrons simulated by the code is underestimated as the absorption physics is not fully modelled in this version of the code. When an ultra-short plasma scale length was introduced, the absorption fraction varied considerably with laser intensity and the hot electron temperatures increased faster-than-expected with laser intensity. Therefore, a more detailed simulation of the scaling of proton beam properties with intensity requires access to multi-dimensional PIC codes in which the angular-dependent absorption mechanisms are included.

References

1. Robinson, APL, Neely, D., McKenna, P., and Evans, RG. Spectral control in proton acceleration with multiple laser pulses. *Plasma Physics and Controlled Fusion*, 49 (2007), 373.
2. Mora, P. Plasma expansion into a vacuum. *Physical review letters*, 90, 18 (2003), 185002.
3. Streeter, MJV, Foster, PS, Cameron, FH et al. Relativistic plasma surfaces as an efficient second harmonic generator. *New Journal of Physics*, 13 (2011), 023041.
4. Pirozhkov, AS, Choi, IW, Sung, JH et al. Diagnostic of laser contrast using target reflectivity. *Applied Physics Letters*, 94 (2009), 241102.
5. Mordovanakis, A.G., Masson-Laborde, P.E., Easter, J. et al. Temperature scaling of hot electrons produced by a tightly focused relativistic-intensity laser at 0.5 kHz repetition rate. *Applied Physics Letters*, 96, 7 (2010), 071109--071109.
6. Catto, PJ and More, R.M. Sheath inverse bremsstrahlung in laser produced plasmas. *Physics of Fluids*, 20 (1977), 704.
7. Yang, T.Y.B., Kruer, W.L., More, R.M., and Langdon, A.B. Absorption of laser light in overdense plasmas by sheath inverse bremsstrahlung. *Physics of Plasmas*, 2 (1995), 3146.
8. Lefebvre, E. and Bonnaud, G. Nonlinear electron heating in ultrahigh-intensity-laser--plasma interaction. *Physical Review E*, 55, 1 (1997), 1011.
9. Ping, Y., Shepherd, R., Lasinski, BF et al. Absorption of short laser pulses on solid targets in the ultrarelativistic regime. *Physical review letters*, 100, 8 (2008), 085004.

Chapter 7: Development of the Multiple Pulse Sheath Acceleration technique

A laser-driven sheath acceleration technique using the interaction of two ultra-intense laser pulses, narrowly separated in time, incident on a Au, foil target is investigated experimentally. The ‘double-pulse’ sheath acceleration mechanism is used to enhance the production of protons beams from the rear surface of thick (~ 125 μm) and thin (~ 5 μm) planar targets. ‘Thin’ targets are defined here as having a thickness for which refluxing of hot electrons between the surfaces of the target is significant during the laser duration. When the temporal separation of the pulses is optimised, a significant improvement in the laser-to-proton conversion efficiency is observed. The enhancement in the laser-to-proton energy conversion efficiency is measured along with a change in the proton beam angular distribution.

7.1. Multiple pulse sheath acceleration

Numerical [1] and experimental [2] investigations have shown that, for a given laser energy a multi-pulse sheath acceleration technique can be employed to significantly increase the laser-to-proton conversion efficiency. For the study presented here, a double-pulse sheath acceleration (DPSA) technique was employed. DPSA makes use of a single seed pulse from the laser that has been divided into two during the laser amplification chain [3] (see chapter 4.2.2.1), such that the initial pulse has an intensity that is only a fraction of the second pulse intensity. The two pulses overlap spatially but the temporal separation between the pulses can be varied.

This variation of the TNSA scheme relies on a pre-accelerated population of protons and ions existing at the rear surface of the target before and during the main pulse interaction at the front surface. The double-pulse interaction satisfies this condition as the initial pulse is sufficiently intense to initiate TNSA from the rear surface of the target foil. In the presence of the ionising sheath field generated by the initial pulse, a multi-species plasma made up of protons as well as heavier ions is formed. The effect of more than one ion species present in the expanding plasma on the longitudinal phase space of a population of accelerated protons is well described by Tikhonchuk *et al* [4]. Using a simplified analytical approach, Tikhonchuk *et al* demonstrated that a population of accelerated protons in the vicinity of a front of accelerated heavy ions will experience a boosted electrostatic potential. For ultra-short interactions times (< 500fs) this has been shown to lead to the creation of spectral peaks and over longer times these peaks evolve into plateau regions in the proton spectrum. For the interaction times of interest in the present study, a multi-species plasma expansion leads to a bunching of the lower energy protons that are in close proximity to the heavy ion front with an exponentially decreasing distribution of the more energetic protons ahead of this, thus leading to a modified distribution of accelerated protons.

The arrival of the second, higher intensity laser pulse leads to the generation of an increase in the hot electron temperature. 1D PIC simulations carried out by Markey *et al* [2] show, that following the interaction of the second laser pulse, an enhanced accelerating field is found at the interface between the layers of the modified proton distribution, as opposed to the plasma-vacuum interface as in the single pulse case. This enhanced electrostatic field potential is experienced primarily by the high density, lower energy population of protons in the aforementioned modified distribution. As they are accelerated further and begin to expand away from the target surface, a rarefaction wave is initiated as the high density population of protons surge forward ahead of the less dense population of protons. As the delay between the two pulses increases, the expansion of the proton population will increase and act to smooth out the steep density step at the interface of the two proton layers in the modulated distribution. Therefore, an optimum time delay exists for proton flux enhancement.

7.1.2. Development of the double-pulse acceleration technique

Markey *et al* used 100 µm thick foil targets in the first experimental investigation of DPSA so as to greatly reduce the effect of hot electron recirculation between the target surfaces on the proton flux. This ensured that any proton flux enhancements observed would be due to the double-pulse technique only. It also enabled a controlled interaction in which the refluxing of hot electrons between the two pulses arriving would have minimum effect on the generation of the modulated proton distribution and subsequent enhanced field on the rear surface. However, in order to achieve optimum conversion of laser energy into proton energy in the sheath acceleration mechanism, it is worth investigating whether one can exploit the proton flux enhancement that can be achieved when using ‘thin’ foils that are in the refluxing regime (thickness << $\frac{\tau_{laser}c}{2}$) together with the double-pulse technique, i.e. using both effects to enhance the energy coupling to protons. For Vulcan Petawatt laser pulses of duration ~ 800 fs, this translates to using foils that are less than 120 μm in thickness. ‘Thin’ foils also benefit from a decrease in the losses associated with electron transport and scattering through a high Z solid material, enabling greater efficiency of transfer of energy between the laser and the accelerated protons. For applications where high laser-to-proton conversion efficiency is required, such as the proton induced fast-ignition fusion [5], isotope production [6] or warm dense matter production [7], enhancement in the number of medium energy protons (5 – 20 MeV) is of particular interest.

Since protons will be accelerated normal to the sheath field that they experience on the rear surface, any perturbation of the rear surface conditions or modification in the sheath spatial distribution will have a direct effect on the angular distribution of the beam of accelerated protons. This has been explored previously with the introduction of a low intensity, nanosecond pulse before the main pulse interaction in order to enhance the proton beam profile [8] and the introduction of laser-driven shock waves to perturb the rear surface and steer the proton beam [9]. However, this has not yet been explored in the realm of DPSA. The first experimental investigation of double-pulse laser acceleration [2] revealed that the proton flux enhancement measured by the Thomson spectrometers was more pronounced at 12° to target normal, compared to on-axis measurements. This suggests that the double-pulse proton acceleration technique could have a substantial effect on the off-axis distribution of the proton flux. Encouraged by this initial observation, it is therefore of interest to explore the effect that preformed plasma expansion of the rear surface will have on the angular distribution of the resultant proton beam.

Commonly, sheath accelerated protons beams are characterised as having a centrally peaked dose distribution, with an almost Gaussian-like drop off in proton flux in the wings of the beam [10] [11], thus leading to strong variations in proton dose across the delivered beam. Some applications would benefit from a top-hat spatial-intensity profile similar to that used in conventionally sourced proton beams. The effect on the spatial-intensity distribution of the proton beam in the detector plane of employing the DPSA technique will therefore also be explored.

The data presented herein has been obtained during two experimental campaigns, both of which were carried out with the objective to study double pulse sheath acceleration. The initial experimental observations of proton flux enhancement from the first campaign using the double pulse technique are reported by Markey *et al* [2].

This chapter specifically explores the enhancement opportunity within the refluxing regime and the effect on the angular distribution of the proton beam.

7.2 Experimental arrangement

The experiments were both performed using the 1054 nm, petawatt arm of the Vulcan laser system at the Central Laser Facility, Rutherford Appleton Laboratory (see chapter 4.2.2). The general experimental set-up for both campaigns was very similar, apart from the use of a plasma mirror in the first campaign in order to increase the nanosecond laser contrast from 10^7 to 10^9. The recent addition of a new picosecond OPCPA front-end meant that the nanosecond ASE laser contrast was ~ 10^{10} for the second campaign and so a plasma mirror wasn't necessary to ensure that pre-plasma formation on the front surface of the target was negligible before the arrival of the first pulse. The Vulcan laser system was set-up to generate double pulses with temporal separations of a few picoseconds, as described in chapter 4.2.3 and [3]. Laser pulses of FWHM duration ~800 fs and intensity ratio, $I_{initial}$: I_{main}, of 1:10 were delivered onto the target containing a total energy (regardless of the time delay) of ~130 J in the first campaign (accounting for plasma mirror reflectivity) and ~180 J in the second campaign. The double pulse intensity ratio was chosen using the results of previous experimental and simulation studies that have shown that this ratio delivers a significant enhancement in the proton acceleration, compared to other combinations. The pulse duration in the first campaign was slightly shorter at ~ 700 fs and so the intensities that were incident on to the target were calculated as being very similar for both campaigns, despite the difference in laser energy. The beam was focussed onto the target at 45° incidence, in p-polarised geometry. The area of irradiation was increased to ~ 30 μm so as to lower the effective intensity on target with the intention of decreasing the maximum energy of the accelerated proton beam to within the energy region of interest (5-25 MeV) whilst maintaining the maximum laser energy available for absorption. Therefore, the intensity of the initial pulse was ~ 3.2×10^{18} W/cm^2, yielding a peak intensity of ~ 2.9×10^{19} W/cm^2 in the main drive pulse.

Planar, gold foil targets of thickness 125 μm and 100 μm (‘thick’) as well as 5 μm (‘thin’) were irradiated using a temporally shaped (double-pulse) laser intensity profile with delays (t_{delay}) of 0 ps - 2.5 ps between the pulses in the first campaign and 0 ps - 4 ps between the pulses in the second campaign. During the first campaign, radiochromic film (RCF) stacks and Thomson parabola spectrometers were used to measure the proton beam properties. The 50 mm x 50 mm RCF stacks were centered along the target normal axis and positioned 35 ± 1 mm from the target. The laser-plasma interactions and beams of accelerated protons were compared during the second campaign using a similar suite of diagnostics. This included Thomson parabola ion spectrometers positioned along, and at 15° to, the target normal direction and a reflectivity monitor to record the 1ω and 2ω reflected light in the specular direction from the target front surface. The main diagnostic employed to record the dose delivered by forward accelerated proton beams was a stack of RCF dosimetry film. The 25 mm x 50 mm layers of film were placed 40 ± 1 mm from the rear surface of the target, just below the laser axis height so as to capture the lower half of the beam. This diagnostic was designed to provide information on the angular and energy distribution of the proton beam within the energy region of interest and as such, the majority of the results reported here have been obtained using the RCF stacks.

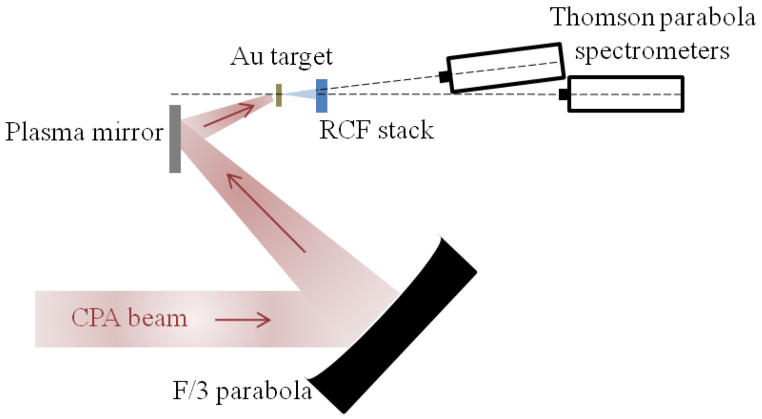

Figure 7.1: Schematic of the experimental arrangement for the first campaign, showing the main diagnostics used. A plasma mirror was incorporated into the setup in order to produce a high contrast laser pulse. The incident angle of the laser onto the target was 40° to the target normal and the RCF stack was positioned 35 ± 1 mm from the target foil, centered to the laser axis height.

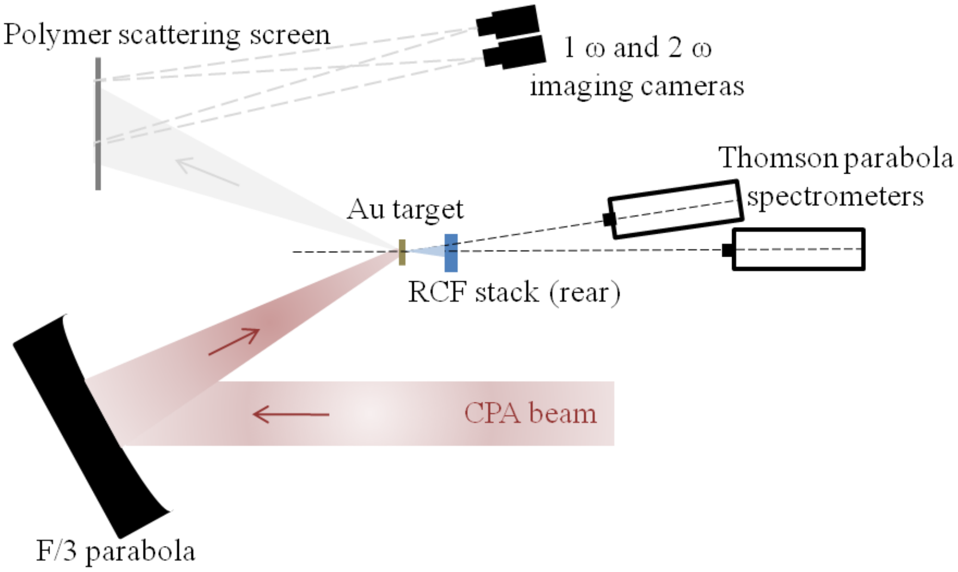

Figure 7.2: Schematic of the experimental arrangement for the second campaign, showing the main diagnostics used. The incident angle of the laser onto the target was 45° to the target normal and the RCF stack was positioned 40 ± 1 mm from the target foil, just below the laser axis height.

7.3 Results

7.3.1. Proton flux enhancement using thin foils

‘Thin’, 5 μm Au target foils were irradiated with a single pulse and then separately with double pulses at temporal separations of 1 ps, 2 ps and 4 ps. The proton beams obtained under these conditions were compared to those obtained under the same interactions conditions with ‘thick’, 125 μm Au target foils where the effects of refluxing hot electrons are negligible. An example of the spatial-intensity of the accelerated proton beams at energies ~ 9 MeV can be seen in radiochromic dosimetry films shown in figure 7.3. It is quite apparent that the use of a thin foil has both increased the proton beam width in the detector plane and substantially increased the dose for all temporal delays employed. The increase in proton beam width in the detector plane is likely due to a change in the spatial gradient of the sheath field caused by the significant enhancement in the amount of refluxing between the target surfaces, and therefore lateral spreading of the hot electron population, that occurs during the laser interaction when thin foils are employed.

However, it appears that proton dose enhancement has come at the cost of dose distribution uniformity. The proton beams accelerated from thick targets are circular, with well-defined edges and smooth dose profiles, whereas the thin targets have produced slightly irregular beam distributions which exhibit central ‘hotspots’. This is typical of many experiments using thin foils and is thought to be because the distribution of hot electrons at the rear side of the target is sensitive to the focal spot intensity distribution when scattering and electron beam divergence is negligible [12]. It could also be a result of non-uniform effects on electron transport associated with significant refluxing, such as electron beam break-up, as the hot electrons make many passes between the target surfaces and spread from the laser interaction region. The apparent increase in the irregularity of the thin foil, double pulse accelerated beams with increasing pulse delay further suggests that pre-expansion at the rear surface in the presence of refluxing electrons encourages beam deformation.

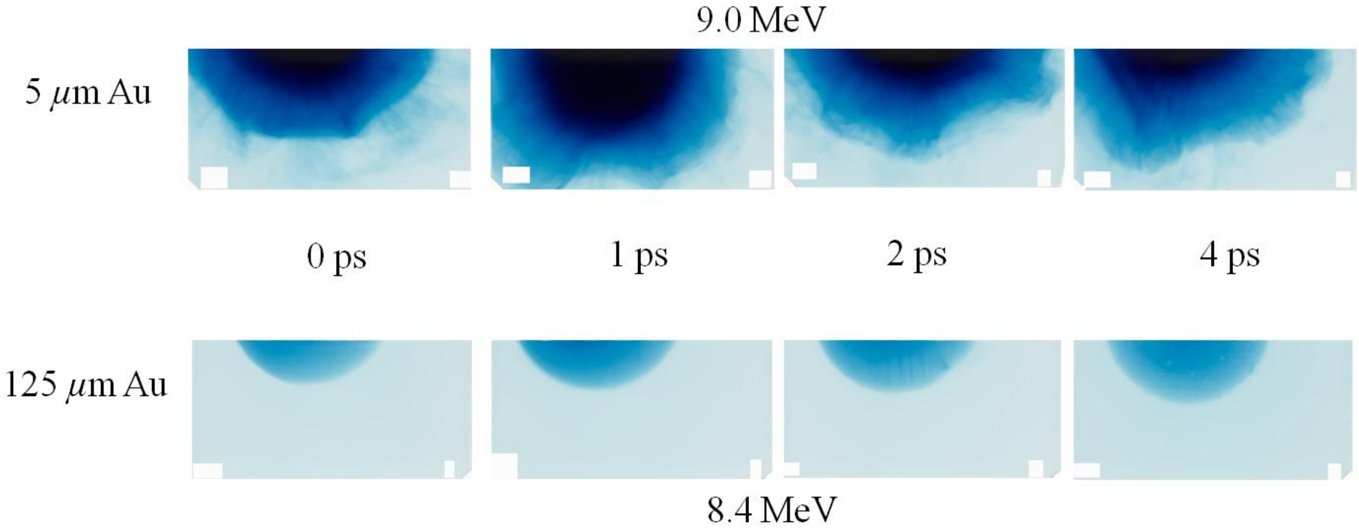

Figure 7.3: Example pieces of RCF exposed to forward propagating proton beams, accelerated using double pulse laser irradiation with increasing temporal delay. 9.0 MeV protons have been sampled here in the case of 5 μm thick foils (top) and 8.4 MeV in the case of 125 μm thick foils (bottom). The active medium in the RCF layers turns a darker blue with increasing proton energy deposition, therefore the optical density is correlated to the proton dose recorded.

Using the method described in chapter 4, the proton dose-energy spectrum was deconvolved to give the number of protons per MeV as a function of proton energy. For each shot, the percentage of the beam captured by the 25 mm × 50 mm RCF stack was calculated by fitting ellipses to outer and inner dose contours of the beam at various layers in the stack and calculating the portion of the beam detected on the film. The proton energy spectra were extracted for both the 5 μm and 125 μm-thick foils and can be seen in figure 7.4. During the 5 μm double pulse shots, the first three layers of RCF recorded a significant proportion of extremely high proton dose in the central region of the beam, above the maximum dose that the film had initially been calibrated to (32 kGy). The dynamic range of the RCF calibration was increased by employing the UV scanning technique developed by Scott *et al* [13] (see chapter 4), in order to extract the full dose measured by the films.

Comparing the double pulse spectra to the 0 ps delay proton spectrum in the case of thin foil irradiation (figure 7.4a) reveals that the high energy portions of the beams exhibit a similar temperature, indicated by the slope of the spectrum. While the 0 ps case appears to follow a single temperature slope, the double pulse spectra suggest a lower temperature to be effective in the lower energy end of the spectrum with the formation of spectral peaks for the 2 ps and 4 ps delays; the change in slope in the 1 ps beam highlighted with the use of dashed lines parallel to the spectrum in figure 7.4a. Interestingly, the onset of the spectral modification is at lower energy for increasing pulse delay, occurring at ~ 17 MeV for 1 ps delay, ~ 12.5 MeV for 2 ps delay (with a spectral peak at ~ 9 MeV) and ~ 10 MeV for 4 ps delay (with a spectral peak at ~ 7.5 MeV). This is consistent with the double pulse mechanism driving a boost in the potential experienced by the dense, low-energy proton population, accelerated by the initial pulse, at later times for increasing pulse delay. Increasing the delay implies that the proton front at the rear surface has more time to expand longitudinally. The higher energy protons, beyond the interface between the two proton populations, expand away from the region where the boosted potential driven by the main pulse is experienced, resulting in lower energy protons benefiting preferentially from the increased conversion efficiency. For the pulse delays used here the optimum enhancement is observed for 1 ps delay.

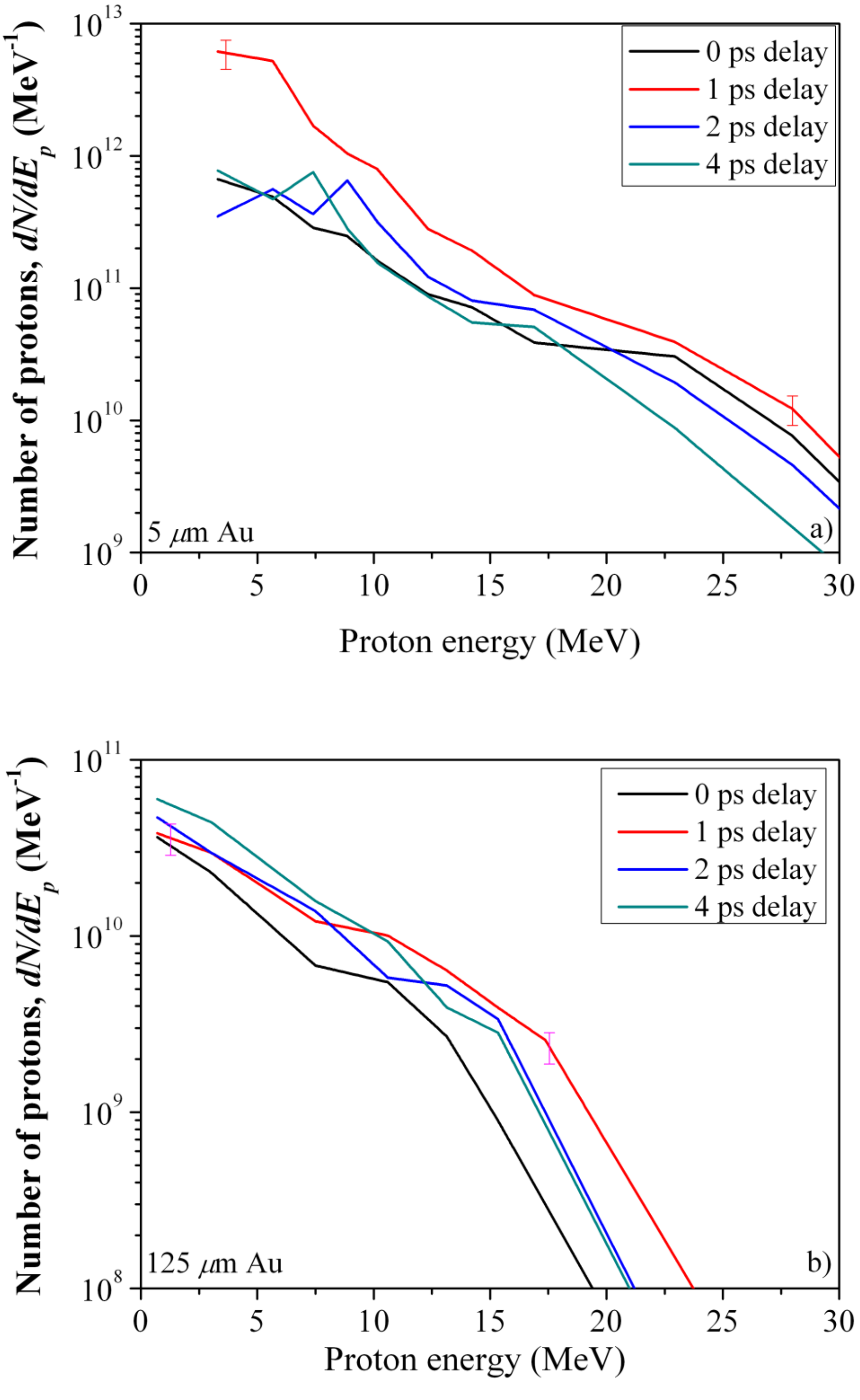

Figure 7.4: Proton energy spectra obtained from a) 5 μm and b) 125 μm thick targets with single pulse (0 ps) and double pulse (1, 2 and 4 ps) irradiation. Example errors bars are shown for the 1 ps delay proton spectrum and are representative of the error bars for all four plots in each figure.

Unfortunately, the amount of structure and deviation in the dose profiles for the proton beams accelerated from the 5 μm target foils means that Thomson parabola spectrometers are not a useful diagnostic in this case, compared to the information recorded by the RCF stacks. The solid angles subtended by the pinhole of the spectrometers (~ 1-7 × 10^{-10} sr) sampled a minute fraction of the beam, equivalent to a 0.4 ± 0.2 μm diameter area in the plane of the dosimetry film. For smooth profiled beams, the proton spectrum extracted by a Thomson parabola spectrometer is effective in providing information that can be converted to units of $(\mathrm{MeVsr})^{-1}$. However, over such a small area (~ 100 times smaller than the resolution of the scanned RCF images) the deviation in proton dose is expected to be considerable, resulting in the extracted proton spectra not being a true representative of the global beam properties. For reference, the proton spectra extracted from the Thomson parabola spectrometers at 0° and 15° can be found in Appendix A.1. It is clear however that for the proton beams produced under the conditions studied here, that one needs to sample the full solid angle subtended by the double pulse accelerated proton beams in order to extract reliable spectra to compare with the 0 ps delay case.

As expected, the proton spectra obtained with the thin, 5 μm targets are considerably higher in proton number compared with the thick target shots, whereas the maximum proton energies have increased by only a factor of ~ 2-3. This is characteristic of the enhancement obtainable when significant refluxing of the hot electrons between the surfaces of the target is occurring. For a 1D plasma expansion model of sheath acceleration [14] (see equation 3.3 in chapter 3), the maximum proton energy is linearly correlated with the hot electron temperature, with a logarithmic dependence on the hot electron density and acceleration time. Therefore, one expects that a considerable increase in the effective hot electron density at the rear surface, as is the case when using thin foils, will only lead to a moderate increase in the maximum proton energy. The number of protons accelerated during sheath acceleration, however, is much more sensitive to the rear surface hot electron density and therefore the effect of significant refluxing is more noticeable on this proton beam property.

The enhancement observed when using a double pulse drive with the thick, 125 μm targets is more subtle compared to the thin target shots. The 1 ps delay is optimal in terms of the maximum proton energy achieved and conversion efficiency into the high energy end of the proton spectrum, consistent with the results reported by Markey *et al*. However, for proton energies less than ~ 10 MeV, the 4 ps delay appears to drive a boost in the number of protons in this part of the spectrum, which is consistent with the energy at which the onset of a spectral enhancement is observed in the 4 ps delay, 5 μm shot. This interesting observation for the longest delay double-pulse acceleration could be the result of increased absorption at the front surface and/or effects on the hot electron transport leading to a modification in the sheath field dynamics on the rear surface. These two factors of the laser-plasma interaction are discussed in sections 7.3.4 and 7.4 respectively.

7.3.2. Laser energy to proton energy conversion efficiency

The total energy contained within the proton beam was extracted across the detected proton energy range from the proton energy spectra shown in figure 7.4. This was then compared to the laser energy incident on to the target for every shot, to give the conversion efficiency of laser energy into proton energy during the acceleration (see figure 7.5). For both target thicknesses, the double-pulse shots lead to an improvement in the conversion efficiency, with a peak conversion efficiency of ~ 14 % to protons with energy 3.3 MeV < E_p < 30.0 MeV achieved by combining a 5 μm-thick target with a 1 ps delay double-pulse drive. The conversion efficiencies increase by a factor of 6 and 2 between a 0 ps and 1ps delay for the thin and thick targets, respectively, and then decrease with a 2 ps delay. Interestingly, the conversion efficiency begins to increase for the thicker target with a delay of 4 ps. This is likely to be because of the boost, observed for the 4 ps delay shot in figure 7.4(b), in the lower energy portion of what is an exponentially decaying proton spectrum. It is the low energy protons which contribute most to the conversion efficiency.

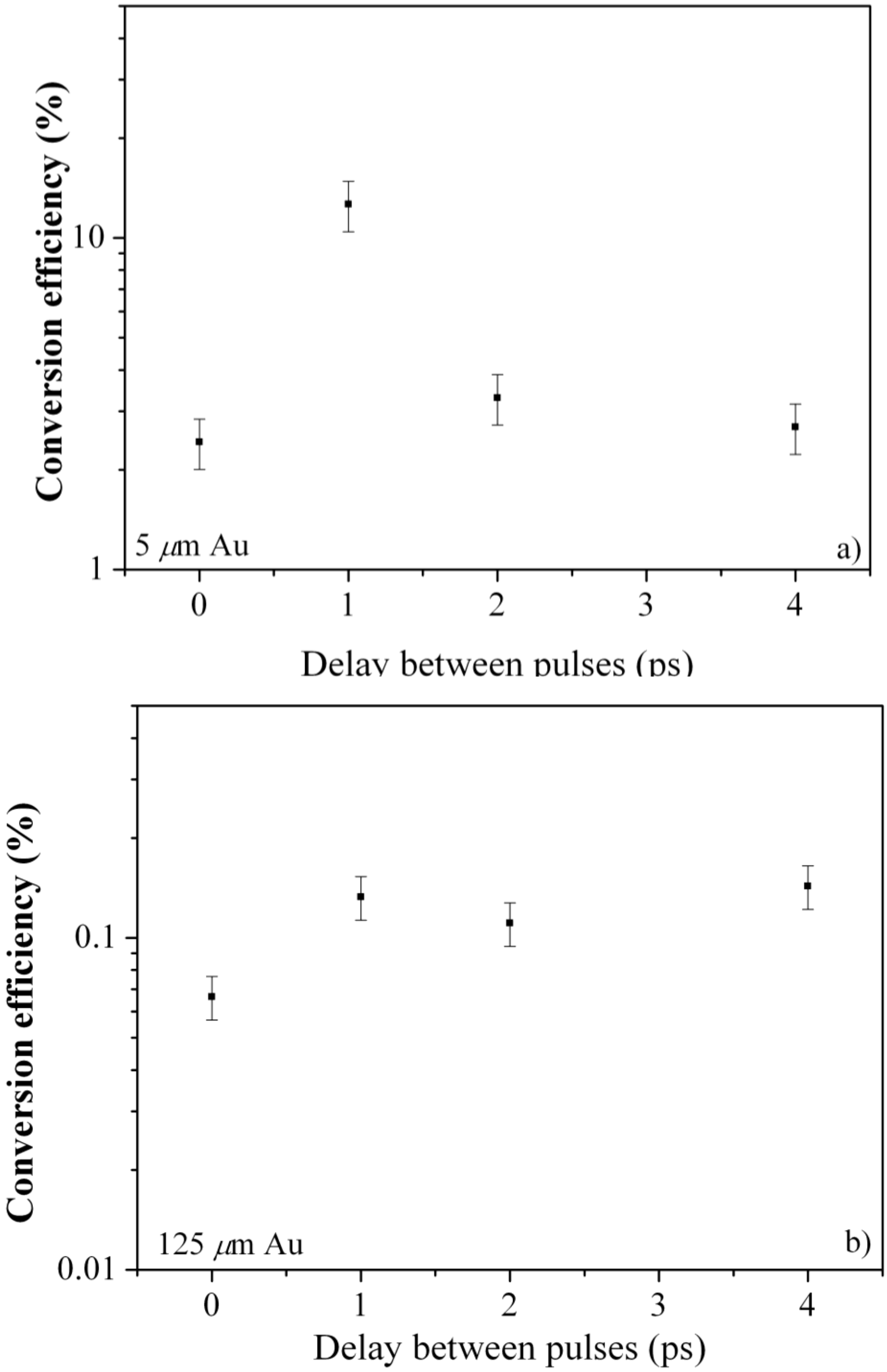

Figure 7.5: Laser-to-proton conversion efficiency obtained from a) 5 μm and b) 125 μm targets with single pulse (0 ps) and double pulse (1, 2 and 4 ps) irradiation.

7.3.3. Reflectivity monitor

During every shot, imaging cameras were used to record the amount of incident fundamental (ω) light reflected from, and frequency doubled (2ω) light generated at, the critical surface of the interaction and falling onto a scattering screen of Polytetrafluoroethylene (PTFE) that was positioned in the specular reflection direction of the laser beam [15]. As an initial estimate, this diagnostic enables the user to quickly compare the amount of light rejected during the interaction and therefore infer the amount of energy absorbed at the front surface relatively from shot-to-shot. It is useful to monitor the relative absorption during the double-pulse interaction so that one can identify whether the proton flux and conversion efficiency enhancement is due to front or rear surface effects. During the interaction of the first relativistically intense pulse, plasma expansion on the front surface is impeded by the radiation pressure of the laser, leading to ponderomotive steepening (see chapter 2.4). A steep plasma gradient is conserved and therefore a significant increase in absorption is not expected to occur compared to the single pulse.

The reflectivity monitor illustrated in the experimental arrangement in figure 7.2 was used together with a series of optical filters to insure that the camera chips were not over-exposed during the image capture duration. A measurement of relative reflectivity from the laser-plasma interaction was extracted from the images by accounting for differences in quantum efficiency of the cameras at the two wavelengths and then for shot-to-shot variation in laser energy delivered onto the target. The corrected 1ω and 2ω signal measured by the two cameras was then added together and normalised to the single pulse interaction value to give an approximation of the relative reflectivity between the shots taken with a single and double pulse profile. Plotting the relative reflectivity as a function of delay between the pulses (see figure 7.6) in the case of 5 μm-thick foil irradiation reveals that the reflectivity remains approximately constant. Using this measurement, it is deduced that there is no significant change in the fraction of laser energy absorbed at the front surface during double-pulse interactions with temporal separations up to, and including, 4 ps.

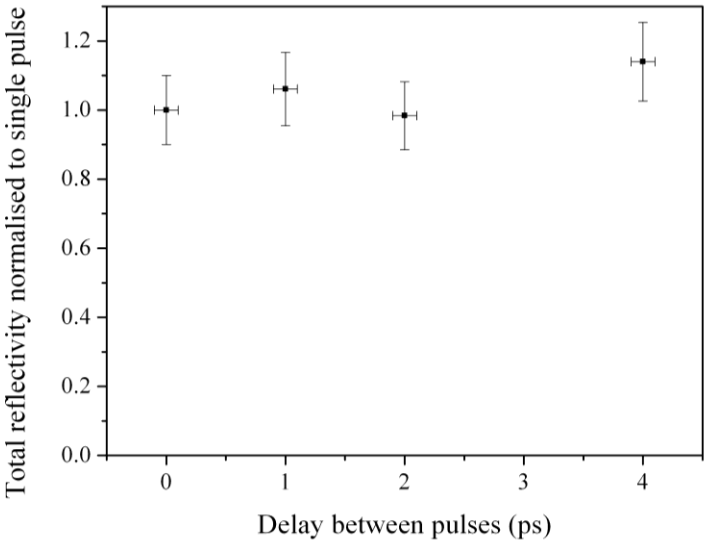

Figure 7.6: Total reflectivity normalised to that of a single pulse as a function of delay between the double pulses.

7.3.4. Angular distribution of the proton beam

To examine the angular profile of the proton beam in more detail, line-outs of the spatial-intensity distribution of the proton beams produced using a 100 μm-thick target were taken in order to compare the dose distribution across the beam that results from the single pulse acceleration technique and the double pulse acceleration technique (see figure 7.7). The shots taken with thick targets were considered only, as the effect on the angular distribution and divergence can be easily characterised in the case of smooth, round beams. Furthermore, echoing the argument used for thick foils by Markey *et al*, the effect of double pulse irradiation on the dose distribution can be isolated from the effects of refluxing and therefore more clearly identified.

For each energy band shown, the double pulse accelerated proton beam dose profiles contained at least twice as much proton dose, therefore normalised dose profiles have been presented, so that the distribution of the proton dose across the beam is more easily compared. The profiles were extracted from the top half of the beam and the 0° point was taken as being the centre of the beam as measured on the RCF (note that for these shots the RCF was machined with a horizontal slit in the middle of the film to allow field of view for the Thomson parabola spectrometers positioned behind the RCF stacks).

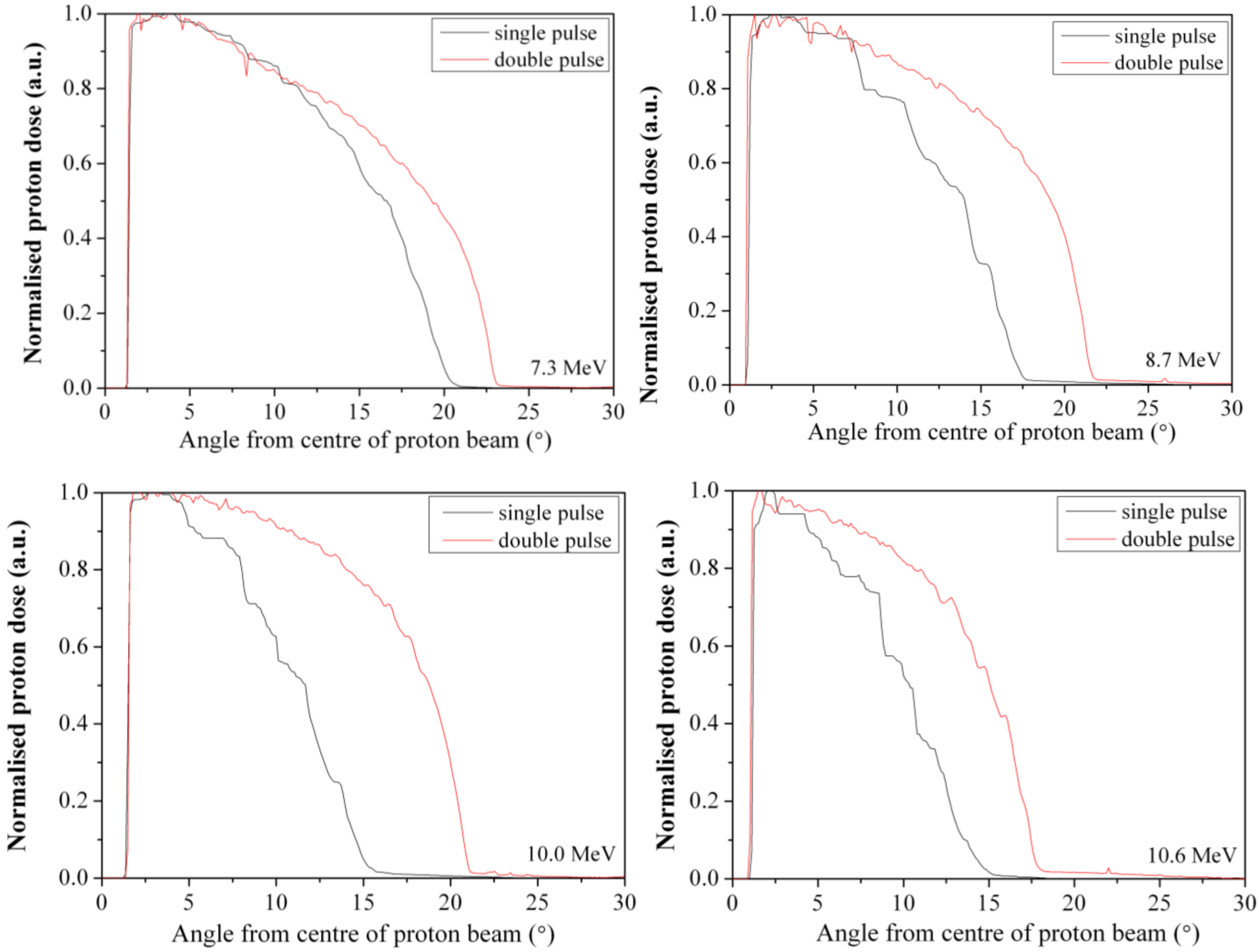

Figure 7.7: Dose profiles taken from the centre of the proton beam at various energy intervals for proton beams accelerated from a 100 μm thick target using a single pulse compared with using a double pulse (0.75 ps delay) at given proton energies.

It is interesting to note the change in the angular distribution of the proton flux when the double pulse mechanism is employed. The proton flux is more uniformly spread and a much larger proportion of the proton flux is found further from the centre of the beam compared to the single pulse accelerated proton beam. The shape of the dose profile for the double pulse accelerated proton beam begins to approach that of a more top-hat profile for the higher energy components of the beam, which is evident from the dose profiles for protons of energy ~ 10 MeV (see figure 7.7).

It was noted for these shots that the proton flux enhancement resulting from the double pulse technique, as observed experimentally by a Thomson parabola spectrometer, is more pronounced at 12° to the laser axis compared to the target normal axis. The spatial-intensity profiles in figure 7.7 go some way in explaining this observation, in that they show that the double pulse technique appears to have a significant effect not only on the integrated flux of protons, but also on how those protons are distributed across the beam. As can be seen in figure 7.7, for the double pulse accelerated beam, the proton dose remains above 80% of the maximum within angles up to 15° from the centre of the beam. This will be beneficial for proton heating and imaging applications where a more uniform dose profile is required.

7.3.5. Proton beam divergence

Initial observations of the angular distribution profiles in figure 7.7 suggest that the improvement in the total dosage in the beam is not the only effect of using the double pulse. For shots taken with a double pulse profile, the diameter of the beam in the RCF plane increases for equivalent energies as compared to the single pulse (t_{delay} = 0 ps) case.

Within a typical laser accelerated proton beam, the angular envelope of the protons tends to decrease with increasing proton energy. This is a consequence of, in the framework of the TNSA mechanism, the highest energy protons accelerated where and when the sheath field is strongest, which coincides with when the emission area is a minimum. However, because the protons are accelerated normal to the contours of the sheath, it also follows that the trajectory of the protons, and hence the global angular profile of the beam, is heavily dependent on the shape of the sheath and its evolution during the acceleration process. One can observe the effect of a change in the sheath shape by measurement of the proton beam divergence with proton energy. To illustrate the effect of using the double pulse technique on the divergence of the entire proton beam, a plot of the half-angle width of the proton beam as a function of proton energy has been produced for both thick target data sets (see figure 7.8).

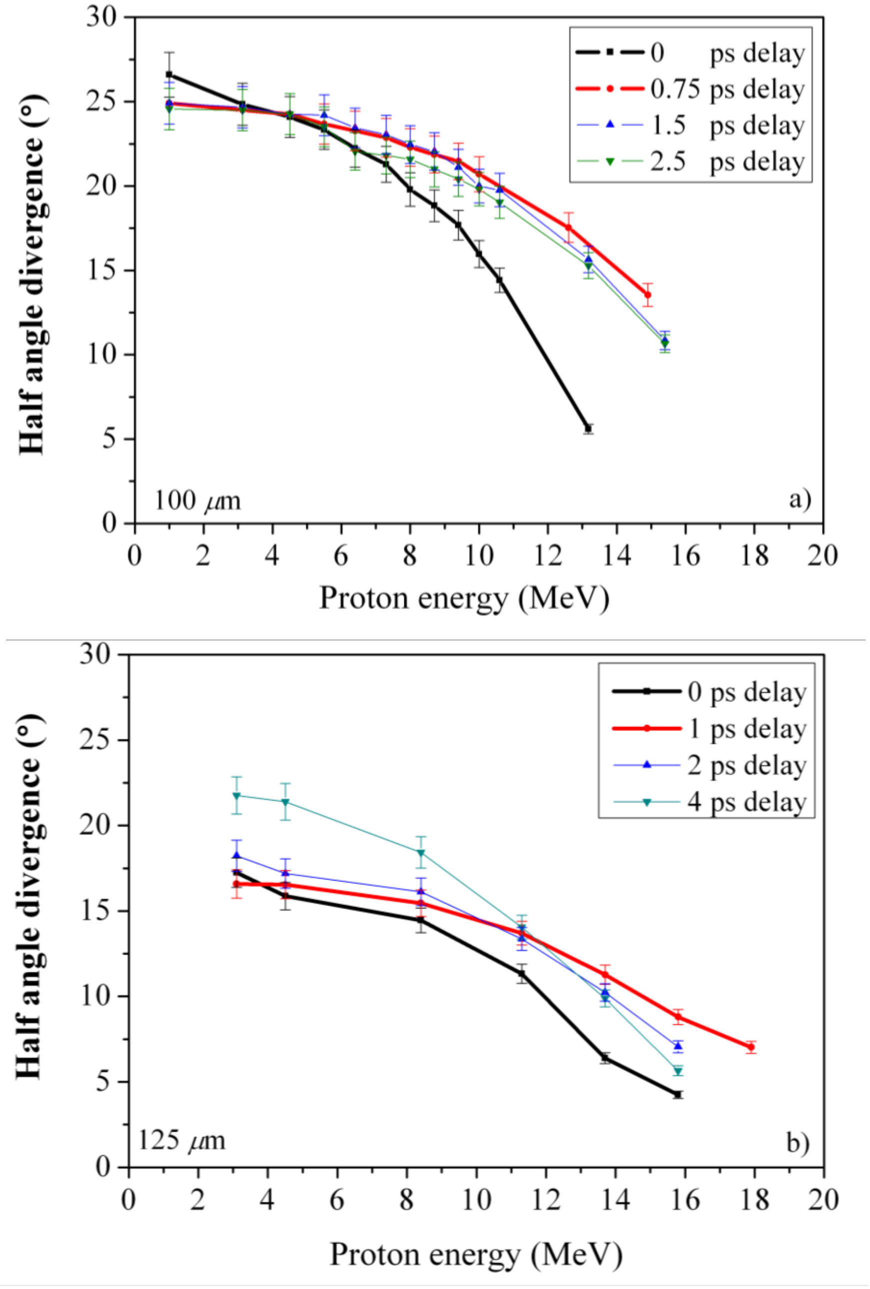

Figure 7.8: The vertical half-angle divergence of the beam plotted as a function of proton energy for beams produced using the double pulse mechanism interacting with a 100 μm thick target (top) and a 125 μm thick target (bottom).

Comparing the shape of the divergence graphs for that of a single pulse (highlighted in black) with the optimum double-pulse delay for angular distribution (highlighted in red), one can see that with a double pulse, the decrease in the half angle width of the beam with increasing proton energy is at a much slower rate. For proton energies up to 10 MeV, an almost plateau-like region emerges in the divergence when a double pulse is employed, before dropping off steadily, to approximately half the initial width of the beam. Between proton energies of 1 MeV < E_p < 10 MeV, the half-angle width decreases by 40 ± 5 % when a single pulse is employed. Whereas when a double pulse is employed, it only decreases by 17 ± 8.0 % at a pulse delay of 0.75 ps. Furthermore, the width of the higher energy component of the beam is significantly larger than when a single pulse is employed. In each instance of using a double pulse, the beam width has increased significantly for energies more than 10 MeV and has approximately doubled for proton energies more than 12 MeV. The trend is broken for the longest temporal delay employed (4 ps), with a noticeable increase in the divergence of the beam at lower proton energies compared to the other shots taken in that data set.

7.4. Modelling the divergence of the plasma expansion

Numerical investigations into the double pulse technique have already been conducted using 1D simulation codes [1]. They have been used to investigate the plasma expansion as a function of electron temperature and the consequence of this on the longitudinal phase space of the sheath accelerated proton beam distribution. Thus far, little attention has been given to examining the effect of a double pulse laser profile on the spatial evolution of the sheath field on the target rear surface and its multi-dimensional impact on the proton beam produced.

The experimental data presented in this chapter suggests that there is a notable effect on the angular distribution of the proton beams produced using the double-pulse technique. In particular, the proton beam divergence angle with proton energy exhibits a clear increase in half-angle width of the beam for the highest proton energies when the double-pulse configuration is employed. This observation can be interpreted as a result of a change in the electrostatic plasma sheath shape and/or a change in the area of proton emission on the rear surface of the target foil.

A useful insight into the rear-surface dynamics can be provided by relating the measured angular width of the proton beam to the contours of a sheath, of given spatial width and profile that is expanding from the rear surface. A simple sheath expansion model developed by Carroll *et al* [8] is used to reproduce the experimentally obtained proton divergence vs energy graphs in figure 7.8 by exploring possible sheath shapes and peak accelerating fields. The sheath expansion model is able to calculate the position of a front of protons as it expands away from the target rear surface. The energy and divergence of the protons along the front is then determined as a function of time for a sheath field that has a temporal and spatial profile that has been defined by the user. From these results one can deduce an approximation of the spatial distribution and size of the proton source that was effective during the single and double-pulse interactions.

The model is initiated with an electric field that has a Gaussian temporal profile with a FWHM equal to the laser pulse duration, τ_L, and a peak strength that is chosen so as to reproduce the measured maximum detected proton energy. The spatial profile and initial lateral width of the simulated sheath field is then varied to fit the experimental data. Example spatial profile functions that can be incorporated in the model include a Gaussian and inverse parabola, both of which have been reported in previous experimental campaigns [11] [10], hyperbola and ellipse. Assuming that the dominant ionisation mechanism in the TNSA process on the rear surface is field ionisation, the spatial extent of the proton source can then be defined by the model when and where the sheath field exceeds the threshold for ionisation of hydrogen. As the proton front expands away from the target rear surface, the proton energies are calculated as a function of radius from the centre of the sheath and the local normal at each point along the ion front is calculated in 0.1 ps intervals over a 4 ps timescale. The model is thus able to produce the proton emission angle as a function of proton energy which can be compared to the experimentally measured values.

Unlike a Particle-In-Cell (PIC) simulation, the sheath model cannot be used to investigate the double-pulse effect on the longitudinal phase space of the proton distribution that leads to the enhancement observed in the spectra. The model is used to simulate the expansion of a sheath field with a single temporal pulse profile only. For an initial approximation this is suitable as this is equivalent to modelling the interaction of the main pulse with the target. The PIC simulations have shown that the main pulse interaction leads to an enhanced electric field strength which acts on the already existing proton front, rather than initiating a second front. Therefore, it is expected that the peak field strength that is required to reproduce the double-pulse divergence data using the sheath model will be higher than for the single pulse data.

The temporal profile of the electric field was set to a FWHM of 700 fs or 800 fs to reflect the laser pulse duration during the first and second campaign respectively. The peak field strength required in the sheath model to reproduce the maximum detected proton energies using the thick (100 μm and 125 μm-thick) targets was in the range 0.58-0.68 TV/m. For each shot, the parameters used in the model (sheath shape and width) were varied until a good match was found with the experimental values of beam divergence as a function of proton energy.

By using the sheath model to investigate with various sheath shapes, the proton beam divergence as a function of proton energy for all shots has been very well reproduced (please refer to Appendix A.2 for results). An interesting initial result of using this model is that for both the single and double pulse shots a hyperbolic sheath distribution provided the best fit to the experimental values. The single pulse interaction with a 100 μm-thick foil produces a divergence graph that deviates slightly from the hyperbolic prediction of the sheath model, suggesting that the single pulse interaction does not deliver a pure hyperbolic sheath field function like in the case of the double-pulse interaction. This suggests that, within a 1D model of the plasma expansion, the envelope shape of the sheath produced on the rear surface is not significantly affected by the double-pulse interaction technique. The key differences between the single and double-pulse results are apparent when one compares the maximum peak field and width of the simulated sheath required to match the experimental values of maximum proton energy and divergence, respectively (see figure 7.9).

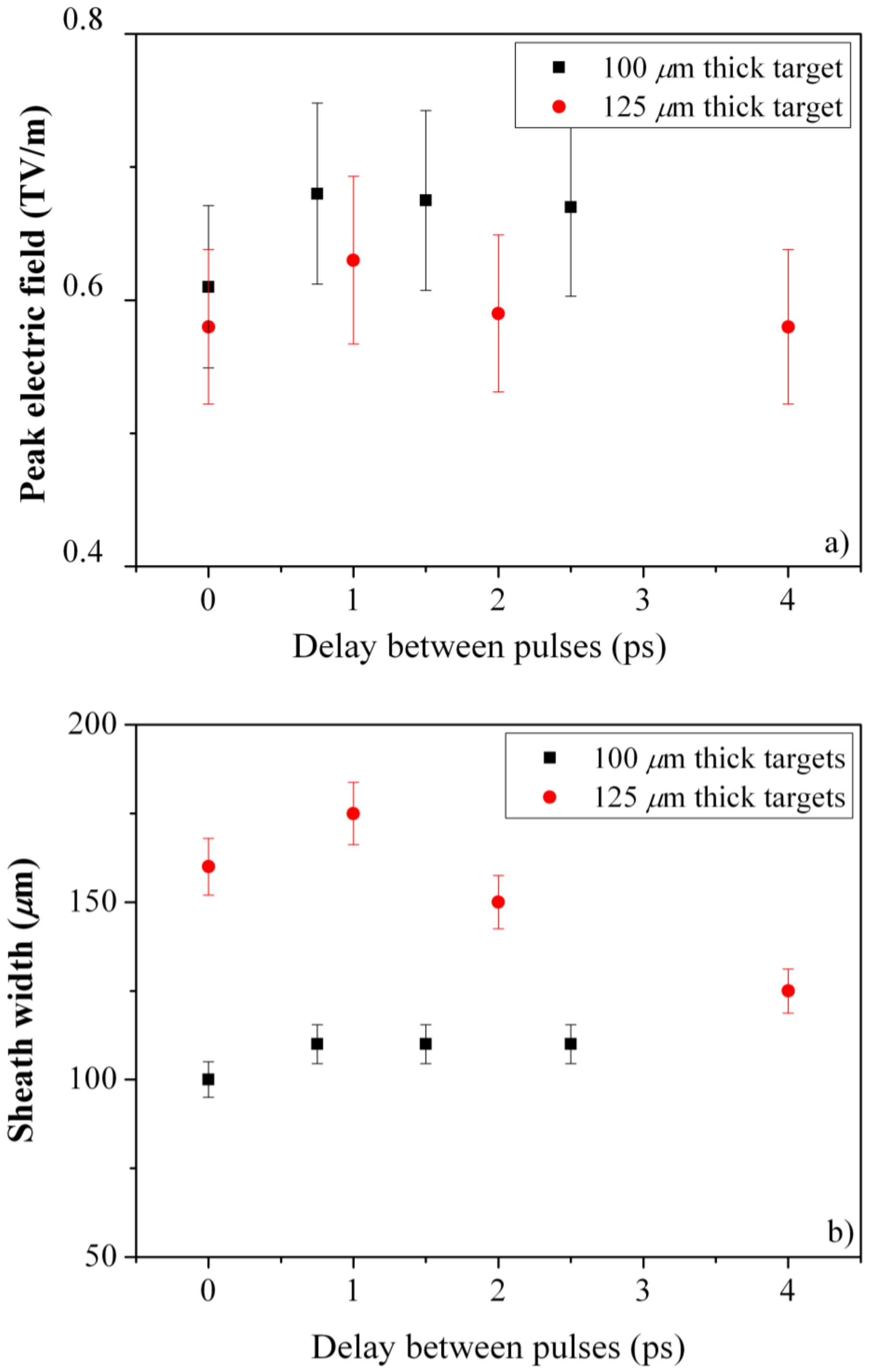

Figure 7.9: a) Peak electric field and b) width of the sheath used in the model to reproduce the experimental proton beam divergence data.

Changes to the properties of the sheath induced by the double-pulse technique are subtle, however there does exist a general trend in both sheath properties; an optimum is reached at a delay of around 1 ps before decreasing as the delay is increased further. As expected, the peak electric field of the sheath required to reproduce the maximum detected proton energies increases when the double-pulse acceleration technique is effective. This is also accompanied by a ~ 10 % increase in the width of the simulated sheath field. A small increase in the proton source size accompanied by an increase in peak field has led to the generation of proton beams that have very similar spatial distribution to that of the single pulse, albeit over a larger area. However, it is worth noting these are simplified approximations of the effect on the sheath field only.

Interestingly, the sheath properties deduced for the longest temporal delay, 4 ps, suggest that the peak electric field is very similar to that of the single pulse case, but that the proton source size is around 16 % smaller. This noticeable difference in the lateral width of the simulated sheath could be the result of an azimuthal magnetic field generated in the target, driven by the hot electron transport during the first interaction, which acts to guide the hot electrons accelerated by the main pulse towards the laser axis [16]. This observation can also be connected to the rise in conversion efficiency noted for the 4 ps double pulse shots. If the lateral spreading of the hot electron population has been suppressed then the effective electron density on the rear surface during the boosted phase will increase compared to the 2 ps delay shots, where the effect is neglible, and increase the number of low energy protons accelerated by the boosted field at the interface between the two proton populations.

7.5 Summary and conclusion

Combining the effect of refluxing hot electrons with the double-pulse sheath acceleration mechanism has resulted in significantly enhanced proton spectra obtained with pulse separations of 1 ps, 2 ps and 4 ps. The effect was found to be optimal with a temporal separation of 1 ps, for which the laser-to-proton conversion efficiency has been measured as ~ 10 %, compared to a conversion efficiency of ~ 3 % measured with a delay of 0 ps (i.e. single pulse).

The effect on the angular distribution of sheath accelerated proton beams when a double-pulse profile is introduced into the interacting laser pulse has been investigated. In particular, the results show that with the double-pulse configuration, the envelope divergence of the proton beam decreases much slower with proton energy compared to the single-pulse accelerated proton beam divergence. The measured values are compared to values deduced from a sheath expansion model, which indicate that the sheath shape does not change significantly when driven by a double-pulse laser profile. The model does however suggest that the peak field experienced by the protons along with the proton source size change when the double-pulse technique is employed, optimising at ~ 1ps. When the delay between the pulses increases to ~ 4 ps, the width of the hot electron population at the target rear decreases and thus increases the effective density. Such an effect enhances the proton spectrum, and increases the proton divergence, at lower energies (< 5 MeV). Furthermore, the distribution of the proton flux changes when a double pulse is employed with thick foils. There is an increased proportion of protons in the wings of the beam, giving the appearance of a more top-hat-like spatial-intensity profile. However combining DPSA with thin foils, where refluxing is significant, appears to be detrimental to the quality of the dose distribution, producing structure in the beam at the edges. Further work, in terms of producing large uniform defocused irradiation areas, may help to suppress this.

The double-pulse mechanism of laser-proton acceleration has been shown to be a simple but effective method for enhancing the properties of a sheath accelerated proton beam. The development work presented in this chapter has shown that it is highly effective in the ‘thin’ foil regime, where ultra-high proton flux is achievable. It is also found that secondary effects of the rear-surface pre-expansion can be favourable to the angular distribution of the beam when thick foils are employed. Finally, as it is an optically based method, rather than reliant on target engineering, it is much better suited for high repetition rate laser systems. This technique is very promising and suggests that temporal shaping of the laser pulse would be a useful feature in the design of a laser-proton source for applications.

References

1. Robinson, APL, Neely, D., McKenna, P., and Evans, RG. Spectral control in proton acceleration with multiple laser pulses. *Plasma Physics and Controlled Fusion*, 49 (2007), 373.
2. Markey, K., McKenna, P., Brenner, CM et al. Spectral Enhancement in the Double Pulse Regime of Laser Proton Acceleration. *Physical review letters*, 105, 19 (2010), 195008.
3. Musgrave, I. Pre-pulse generator for controllable picoseconds pre-pulses in TAP. *Central Laser Facility annual report* (2011).
4. Tikhonchuk, VT, Andreev, AA, Bochkarev, SG, and Bychenkov, V.Y. Ion acceleration in short-laser-pulse interaction with solid foils. *Plasma physics and controlled fusion*, 47 (2005), B869.
5. Roth, M., Cowan, TE, Key, MH et al. Fast ignition by intense laser-accelerated proton beams. *Physical review letters*, 86, 3 (2001), 436--439.
6. Fritzler, S., Malka, V., Grillon, G. et al. Proton beams generated with high-intensity lasers: Applications to medical isotope production. *Applied physics letters*, 83 (2003), 3039.
7. Patel, PK, Mackinnon, AJ, Key, MH et al. Isochoric heating of solid-density matter with an ultrafast proton beam. *Physical review letters*, 91, 12 (2003), 125004.
8. Carroll, DC, McKenna, P., Lundh, O. et al. Active manipulation of the spatial energy distribution of laser-accelerated proton beams. *Physical Review E*, 76, 6 (2007), 065401.
9. Lundh, O., Glinec, Y., Homann, C. et al. Active steering of laser-accelerated ion beams. *Applied Physics Letters*, 92, 1 (2008), 011504--011504.
10. Brambrink, E., Schreiber, J., Schlegel, T. et al. Transverse characteristics of short-pulse laser-produced ion beams: a study of the acceleration dynamics.

Physical review letters, 96, 15 (2006), 154801.

11. Romagnani, L., Fuchs, J., Borghesi, M. et al. Dynamics of electric fields driving the laser acceleration of multi-MeV protons. *Physical review letters*, 95, 19 (2005), 195001.
12. Schollmeier, M., Harres, K., Nürnberg, F. et al. Laser beam-profile impression and target thickness impact on laser-accelerated protons. *Physics of Plasmas*, 15 (2008), 053101.
13. Scott, GG., Green, JS., Fiorini, F. et al. Maximising the dynamic range of radiochromic film through novel scanning techniques. *Central Laser Facility annual report* (2010-2011).
14. Mora, P. Plasma expansion into a vacuum. *Physical review letters*, 90, 18 (2003), 185002.
15. Streeter, MJV, Foster, PS, Cameron, FH et al. Relativistic plasma surfaces as an efficient second harmonic generator. *New Journal of Physics*, 13 (2011), 023041.
16. Scott, RHH, Beaucourt, C., Schlenvoigt, HP et al. Controlling Fast-Electron-Beam Divergence Using Two Laser Pulses. *Physical Review Letters*, 109, 1 (2012), 015001.

Chapter 8: Conclusions & future outlook

A summary of the key findings of this PhD project is presented herein, accompanied by a discussion of potential further work. Suggestions for future directions in experimental investigations of laser-driven proton acceleration are also given, including ideas for laser beam distribution improvement and a novel ‘nanospoke’ target design for investigations of radiation pressure acceleration.

8.1. Thesis summary and further work

Laser-driven multi-MeV proton beams, generated by intense laser interaction with solid-density materials, have been investigated with a particular focus on spectral control by tuning of the laser parameters, as well as for efficiency enhancement by using a double-pulse mechanism. The work presented in this thesis has been based on proton acceleration resulting from a strong suprathermal (hot)-electron sheath field (of the order 10^{12}V/m) established on the rear surface of the target (the hot electrons being transported through the target from the laser-irradiated front surface). The mechanisms presented rely on optical techniques and have simple target fabrication demands, therefore facilitating the potential for high repetition rate operation for the applications outlined in chapter 1. The key findings, summarised below, have contributed new understanding in laser-driven proton acceleration, progressing the work of the LIBRA (Laser Induced Beams of Radiation and their Applications) project [1] and the HiPER (High Power laser Energy Research) project [2] consortia.

8.1.1. Spectral control

Proton beams accelerated as a result of the interaction of an ultra-short, moderately intense laser pulse with an ultra-thin foil target were used to distinguish the effects on proton beam spectral properties of changing laser pulse energy and focal spot size. The scalings of the maximum energy and number of protons were initially investigated by first varying the laser pulse energy delivered to the target at two defocused spot sizes, and secondly by varying the focal spot size at the maximum laser pulse energy available.

By plotting the maximum energy and proton number as a function of laser energy and then as a function of laser intensity, a number of interesting observations were made. The total number of protons across the full spectral range was found to be strongly dependent on the laser pulse energy, with a spectral distribution defined by the effective laser intensity. To expand on these findings, it would be useful to characterise the power scaling relation between laser energy and proton flux for different laser systems and target composition. With applications in mind, this result points towards a method of controlling the spectral features and integrated proton dose delivered by a laser-driven proton beam through careful control of the laser energy and illumination conditions employed.

Both the laser pulse energy and focal spot size were found to be significant factors in defining the maximum proton energy, E_{pmax}, as a function of laser intensity. For equivalent changes in laser intensity, the change in E_{pmax} is larger in the case of varying laser energy than when the laser focal spot size is varied. For ultra-thin target irradiation, the effects of hot electron divergence are negligible as the hot electron population makes the first pass through the target, therefore the initial sheath field area is comparable to the focal spot area. Using a large, uniform focal spot distribution in combination with ultra-thin targets, therefore results in a large initial sheath of hot electrons on the rear surface of the target. This condition will contribute to defining the subsequent maximum proton energy when the average time taken for the hot electrons at the centre of the initial sheath field to travel to the edge of the sheath is greater than the laser pulse duration. The role of large focal spot size on proton acceleration is therefore accounted for by a modification to the effective acceleration time. This modification was incorporated into a 1D plasma expansion model and the experimental results were well reproduced.

A 1D simulation code was used to investigate the underlying physics behind the energy and intensity scaling laws reported in chapter 5. The numerical model did not fully reproduce the measured spectra, which motivated an investigation of the scaling of the hot electron temperature and absorption fraction produced by the code using solid-density targets with a step-like density profile and a short scale length density profile. Realistic hot electron temperatures were predicted by the code, compared with those measured experimentally under similar interactions, and a similar scaling was determined for the case of the step-life density profile. However, due to the lack of absorption mechanisms modelled by the code in 1D, the inferred hot electron density was artificially low at non-relativistic intensities, leading to a disparity between the measured and simulated proton beam properties as a function of intensity. In order to continue with numerical modelling to study the scaling of the proton beam parameters as a function of laser parameters, it will therefore be necessary that multi-dimensional simulation codes are used in which the absorption mechanisms can be better simulated and realistic absorption fractions obtained. An open-access version of a 2D particle-in-cell code (EPOCH) [3] has recently been made available, which could be used to further investigate the findings reported in chapter 5.

8.1.2. Conversion efficiency enhancement

The double-pulse sheath acceleration (DPSA) mechanism is effective in increasing the coupling of laser pulse energy in to the resultant proton beam, compared to single pulse irradiation. Making use of the proton flux enhancement that can be achieved with thin foils, where refluxing of hot electrons leads to an increase in the effective hot electron density, a significantly higher laser-to-proton conversion efficiency was measured when the double-pulse technique was employed with a delay of 1 ps, under the conditions of these experiments. The demonstration of the double-pulse mechanism as being effective when employed in combination with thin foils suggests the potential for very high conversion efficiencies from sheath accelerated proton beams, if the mechanism can be further optimised for target thickness, composition or design. Such beams would be particularly useful for the applications described in chapter 1 and as such it is hoped that the experimental work on this mechanism will continue. This work would further benefit from detailed simulation investigations to determine the best routes worth exploring for further optimisation and control. Initial results of 1D PIC simulations carried out by the author indicate that employing the DPSA mechanism with ultra-short laser pulses (~ 40 fs), thin foils (~ 1 μm-thick) and ultra-short (< ps) temporal separation can result in the formation of significant spectral peaks, with the proton energy at which they occur decreasing with increasing the pulse delay. This is yet another route of investigation worth exploring in the near future.

Analysis of the angular distribution and divergence of DPSA proton beams from thick targets indicated that the double-pulse mechanism leads to both an increased proton dose far from the central axis of the beam and a change in the divergence as a function of proton energy, compared to the single pulse case. A sheath expansion model was used to demonstrate that the change in beam divergence can be attributed to a combination of increased peak field strength and source size driven by the DPSA mechanism. Multi-dimensional simulation investigations focusing primarily on the spatial and angular characteristics of double-pulse accelerated proton beams will be useful in confirming the underlying mechanisms behind the observations.

8.2. Future outlook for laser-driven proton acceleration

8.2.1. Proton beam delivery and laser intensity distribution

Harnessing the potential of laser-driven proton beams for imaging, heating and transmutation applications will require continued effort, not only on spectral control and optimisation but also with attention to proton beam delivery and spatial distribution. Techniques for beam handling, including collimation [4] [5], focusing [6] and energy selection [7], have been developed by a handful of groups and will become of greater importance as demand for laser-driven proton sources grows. Specialised target design for beam collimation [8] [9], focusing [10] and ‘pencil’ beam production [11] [12] [13] is a route worth considering to this end. However, as application-driven high-power laser systems progress towards [14] high repetition rates, complex target fabrication becomes a significant limiting factor. Therefore, it is imperative that the development of optical methods of control and enhancement, that can easily facilitate high repetition rate, are also considered.

As demonstrated in chapter 7, laser-driven proton beams accelerated from thin foils can suffer from considerable irregularities and non-uniformity in the spatial-intensity distribution. The use of thick targets counteracts this effect by inducing increased hot electron scattering during the transport from the front to the rear surface of the target [15]. In order to fully exploit the results of chapter 5 and 7, whereby defocused laser irradiation of thin targets has been shown to be a potential source of control and flux enhancement, it is important that the laser intensity distribution is smooth and uniform, especially for large focal spot size. Currently, efforts with this aim are being explored with the use of advanced adaptive optic systems [16] [17] [18].

8.2.2. Novel target design and laser cutting technique for demonstration of advanced laser proton acceleration schemes

Alternative laser-driven proton acceleration mechanisms, such as radiation pressure acceleration (RPA) (see chapter 3.3.2), are currently being investigated for their potential to deliver high energy (> 100 MeV), quasi-monochromatic ion beams with high conversion efficiency. Ion beams with these qualities could be applicable for use in advanced cancer treatment options, such as ion beam oncology, or other applications that require high energy, tunable ion beams. At the limit of present laser capabilities, the RPA mechanism is expected to be observable at high intensities with circular polarisation or by using low density targets in conjunction with long wavelength (~ 10 μm) drivers. First experimental observations of radiation pressure driven spectral features have been reported by employing long wavelength, CO_2 laser pulses with gas jet targets [19] or ultra-thin foil targets, with a thickness of the order of the laser skin-depth, and circular polarisation [20]. A novel target design, comprised of a small, thin central disk suspended by nano-wire spokes and further suspended to the supporting membrane by micro-wire spokes, is proposed for investigation of RPA. The area of the central disk is of the order of the laser focal spot, thereby limiting the range of intensities and mass with which the laser pulse interacts. Such targets would also minimise debris which is preferential for high repetition rate use. This type of limited mass target is predicted to lead to significant enhancements in the maximum energy of accelerated protons [21].

The ‘nanospoke’ is an extension of a ‘micro’ design version, first used by Strangio *et al* [22] for enhancing sheath acceleration beams. The 50 nm thick, silicon-nitride nanospoke (see figure 8.2) targets have been manufactured by the Central Laser Facility’s target fabrication group in collaboration with STFC’s Micro and Nano

Technology Centre, using a silicon-based, wafer-mask and etching process which can facilitate mass production. These targets will be irradiated in May 2012 using the Astra-GEMINI laser at the Central Laser Facility, UK, where their potential for use in laser-driven ion acceleration will be investigated. Beam pointing stability and ultra-high temporal contrast is an important consideration when developing this technique for any of the aforementioned applications.

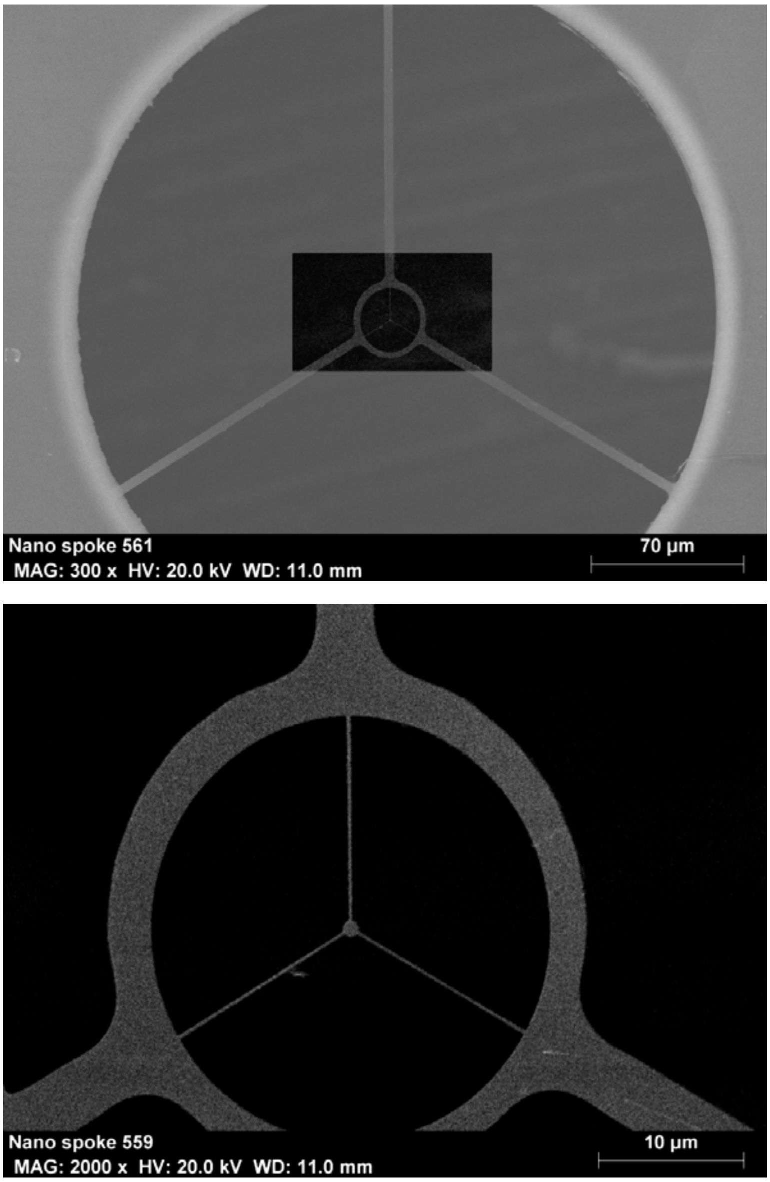

Figure 8.1: Nanospoke targets, imaged using a scanning electron microscope, showing the target suspended in the chip holder (above) and zoomed in on the central disk suspended by nano-wires (below). Scales are given in the bottom left hand corner of each image.

In an extension to this target design, the target mass can be reduced yet further by removing the spokes used to suspend it immediately prior to the laser interaction. A laser-cutting technique has been developed to trim the spokes of the above design, while maintaining the central disk target. Laser-cutting the spokes before the main, high intensity pulse arrives will effectively result in laser irradiation with a free-standing, isolated target. The author helped to develop this technique in the course of this PhD project in collaboration with G. Schaumann. A 532 nm, 5 ns laser pulse was combined with a custom-made axicon lens and accompanied by a 100 mm focus lens to produce a ring of laser light with diameter ~ 50 μm at the focal point to cut the target spokes. Demonstration of the technique was conducted using a two-spoke design, with a 30 μm diameter, ultra-thin (~ 50 nm) central disk target (see figure 8.2). A ring focus was produced and the upper-half of the beam was blocked. The spoke was then irradiated with a low-power, 5 ns laser pulse. Initial results suggest that this technique is sufficient to trim through a micro-wire spoke suspending the target in the chip holder and that the hydrodynamic effects of shock propagation and heating that the ‘long’ pulse interaction initiates does not damage the central region of the target.

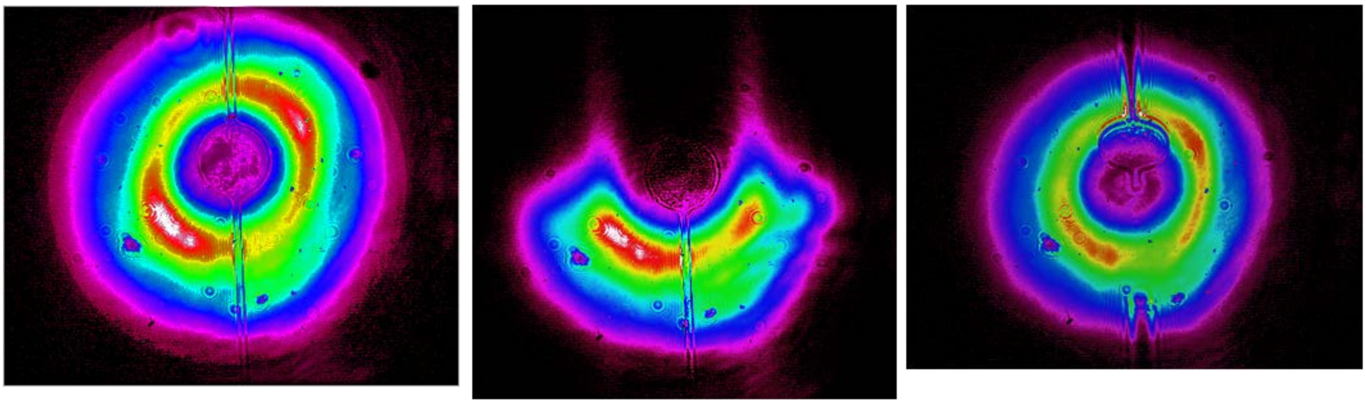

Figure 8.2: The laser-cutting technique investigated with micron-scale versions of the target design. The resultant image on the far right indicates that the spoke has been trimmed and that the central disk target is intact.

Many new experimental opportunities in preparation are expected to yield numerous breakthroughs in the field of laser-driven ion acceleration over the coming years. With much investment into higher intensity, high repetition rate lasers and multi-PW laser systems coming online in the near future (see [23] and [24] for details of the forthcoming Vulcan 10 PW project and ELI project, respectively), this field of research is heading towards a *bright* future.

References

1. *http://www.qub.ac.uk/sites/LIBRA/.*
2. *http://www.hiper-laser.org/.*
3. Brady, CS and Arber, TD. An ion acceleration mechanism in laser illuminated targets with internal electron density structure. *Plasma Physics and Controlled Fusion*, 53 (2011), 015001.
4. Harres, K., Alber, I., Tauschwitz, A. et al. Beam collimation and transport of quasineutral laser-accelerated protons by a solenoid field. *Physics of Plasmas*, 17 (2010), 023107.
5. Ter-Avetisyan, S., Schnurer, M., Polster, R., Nickles, PV, and Sandner, W. First demonstration of collimation and monochromatisation of a laser accelerated proton burst. *Laser and Particle Beams*, 26, 04 (2008), 637--642.
6. Schollmeier, M., Becker, S., Geißel, M. et al. Controlled transport and focusing of laser-accelerated protons with miniature magnetic devices. *Physical review letters*, 101, 5 (2008), 55004.
7. Toncian, T., Borghesi, M., Fuchs, J. et al. Ultrafast laser-driven microlens to focus and energy-select mega-electron volt protons. *Science*, 312, 5772 (2006), 410--413.
8. Kar, S., Markey, K., Simpson, PT et al. Dynamic control of laser-produced proton beams. *Physical review letters*, 100, 10 (2008), 105004.
9. Yang, XH, Ma, YY, Shao, FQ et al. Collimated proton beam generation from ultraintense laser-irradiated hole target. *Laser and Particle Beams*, 28, 02 (2010), 319--325.

10. Patel, PK, Mackinnon, AJ, Key, MH et al. Isochoric heating of solid-density matter with an ultrafast proton beam. *Physical review letters*, 91, 12 (2003), 125004.
11. Liu, M.P., Wu, H.C., Xie, B.S., Liu, J., Wang, H.Y., and Yu, MY. Energetic collimated ion bunch generation from an ultraintense laser interacting with thin concave targets. *Physics of Plasmas*, 15, 6 (2008), 063104--063104.
12. Ma, YY, Sheng, ZM, Gu, YQ et al. High-quality MeV protons from laser interaction with umbrellalike cavity target. *Physics of Plasmas*, 16 (2009), 034502.
13. M. Nishiuchi, A. S. Pirozhkov H. Sakaki K. Ogura T. Zh. Esirkepov T. Tanimoto M. Kanasaki A. Yogo T. Hori A. Sagisaka Y. Fukuda Y. Matsumoto S. Entani S. Sakai C. Brenner D. Neely T. Yamauchi S. V. Bulanov and Kondo, K. Quasi-monochromatic pencil beam of laser-driven protons generated using a conical cavity target holder. *Physics of Plasmas*, accepted (2012).
14. Ertel, K., Banerjee, S., Mason, P. et al. The DiPOLE project: towards high energy, high repetition rate diode pumped lasers. *Central Laser Facility Annual Report (2009-10). http://www. clf. rl. ac. uk/resources/PDF/ar09-10_lsd_full_rd. pdf.*
15. Schollmeier, M., Harres, K., Nürnberg, F. et al. Laser beam-profile impression and target thickness impact on laser-accelerated protons. *Physics of Plasmas*, 15 (2008), 053101.
16. Baker, KL, Homoelle, D., Utternback, E., Stappaerts, EA, Siders, CW, and Barty, CPJ. Interferometric adaptive optics testbed for laser pointing, wave-front control and phasing. *Optics Express*, 17, 19 (2009), 16696--16709.
17. Hooker, CJ, Collier, JL, Hawkes, SJ, and Spindloe, C. Adaptive optics development in the EU OTTER programme. *Central Laser Facility Annual Report*, 2006 (2005), 202--205.
18. Heuck, H.M., Wittrock, U., Fils, J. et al. Adaptive optics at the PHELIX laser. In *Proceedings of SPIE* (2007), 658402.
19. Palmer, C.A.J., Dover, NP, Pogorelsky, I. et al. Monoenergetic proton beams

accelerated by a radiation pressure driven shock. *Physical Review Letters*, 106, 1 (2011), 14801.

20. Henig, A., Steinke, S., Schnürer, M. et al. Radiation-pressure acceleration of ion beams driven by circularly polarized laser pulses. *Physical review letters*, 103, 24 (2009), 245003.
21. Limpouch, J., Psikal, J., Andreev, AA, Platonov, K.Y., and Kawata, S. Enhanced laser ion acceleration from mass-limited targets. *Laser and Particle Beams-Pulse Power and High Energy Densities*, 26, 2 (2008), 225--234.
22. Strangio, C., Caruso, A., Neely, D. et al. Production of multi-MeV per nucleon ions in the controlled amount of matter mode (CAM) by using causally isolated targets. *Laser and Particle Beams-Pulse Power and High Energy Densities*, 25, 1 (2007), 85--92.
23. Hernandez-Gomez, C., Blake, SP, Chekhlov, O. et al. The Vulcan 10 PW project. In *Journal of Physics: Conference Series* (2010), 032006.
24. Chambaret, J.P., Georges, P., Chériaux, G. et al. The Extreme Light Infrastructure Project ELI and Its Prototype APOLLON/ILE:“The Associated Laser Bottlenecks”. In *Frontiers in Optics* (2009).

Appendix A.1

Proton beams accelerated from the rear surface of 5 μm-thick Au foils, irradiated with a double-pulse (see chapter 7 for details), were sampled using Thomson parabola spectrometers positioned along the target normal and at 15° to the target normal. The combination of significant dose deviation across the proton beam and small solid angle (~ 1-7 × 10^{-10} sr) subtended by the pinhole of the spectrometers, means that Thomson parabola spectrometers are not a useful diagnostic in this case, compared to the information recorded by the radiochromic film stacks.

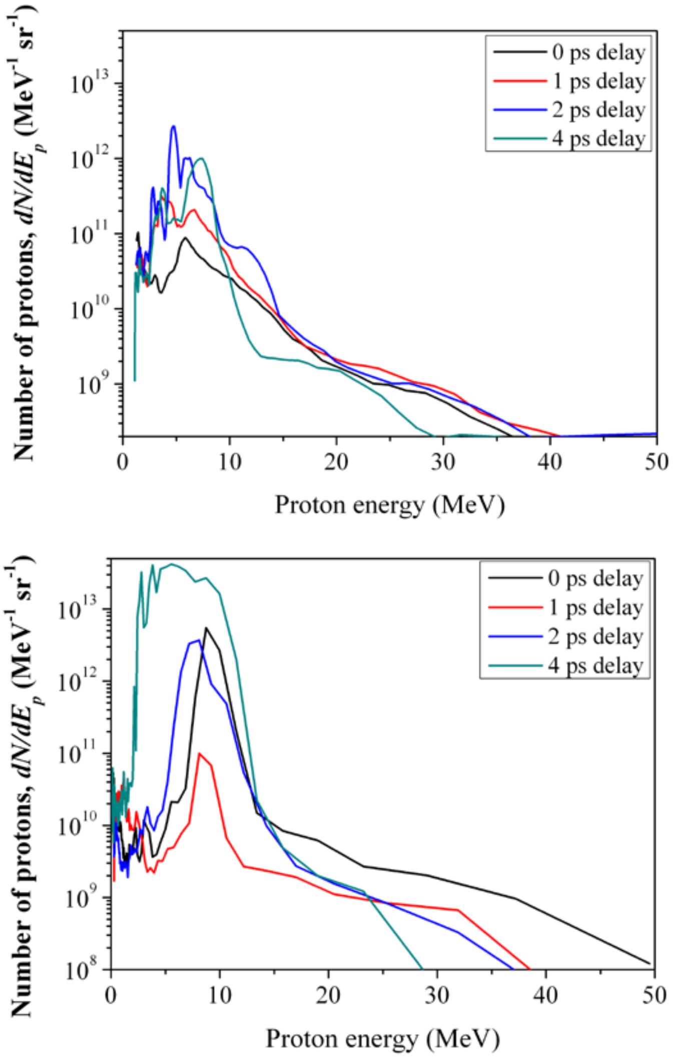

Figure A.1: Proton spectra obtained from Thomson parabola spectrometers from 5 μm-thick targets with single pulse (0 ps) and double pulse (1, 2 and 4 ps) irradiation.

Appendix A.2

A sheath model is used to investigate the divergence of proton beams accelerated with a single pulse (0 ps) and double pulse (0.75-4 ps) (see chapter 7 for details). The peak field strength required in the sheath model to reproduce the maximum detected proton energies using the thick (100 μm and 125 μm-thick) targets was in the range 0.58-0.68 TV/m. For each shot, the parameters used in the model (sheath shape and width) were varied until a good match was found with the experimental values of beam divergence as a function of proton energy (see figures A.2 and A.3).

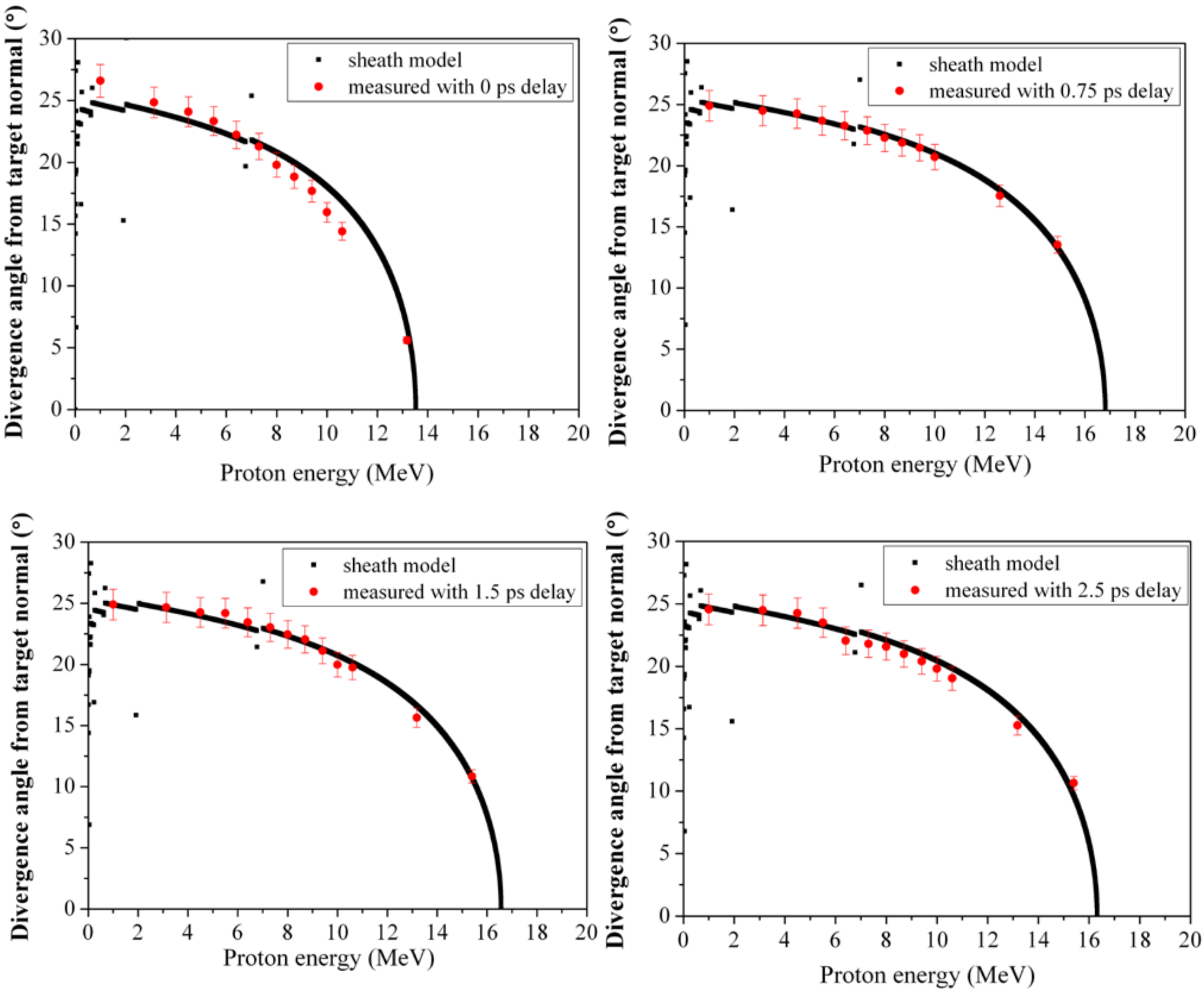

Figure A.2: Measured (red) and modelled (black) values of half angle divergence plotted as a function of proton energy for targets of thickness 100 μm.

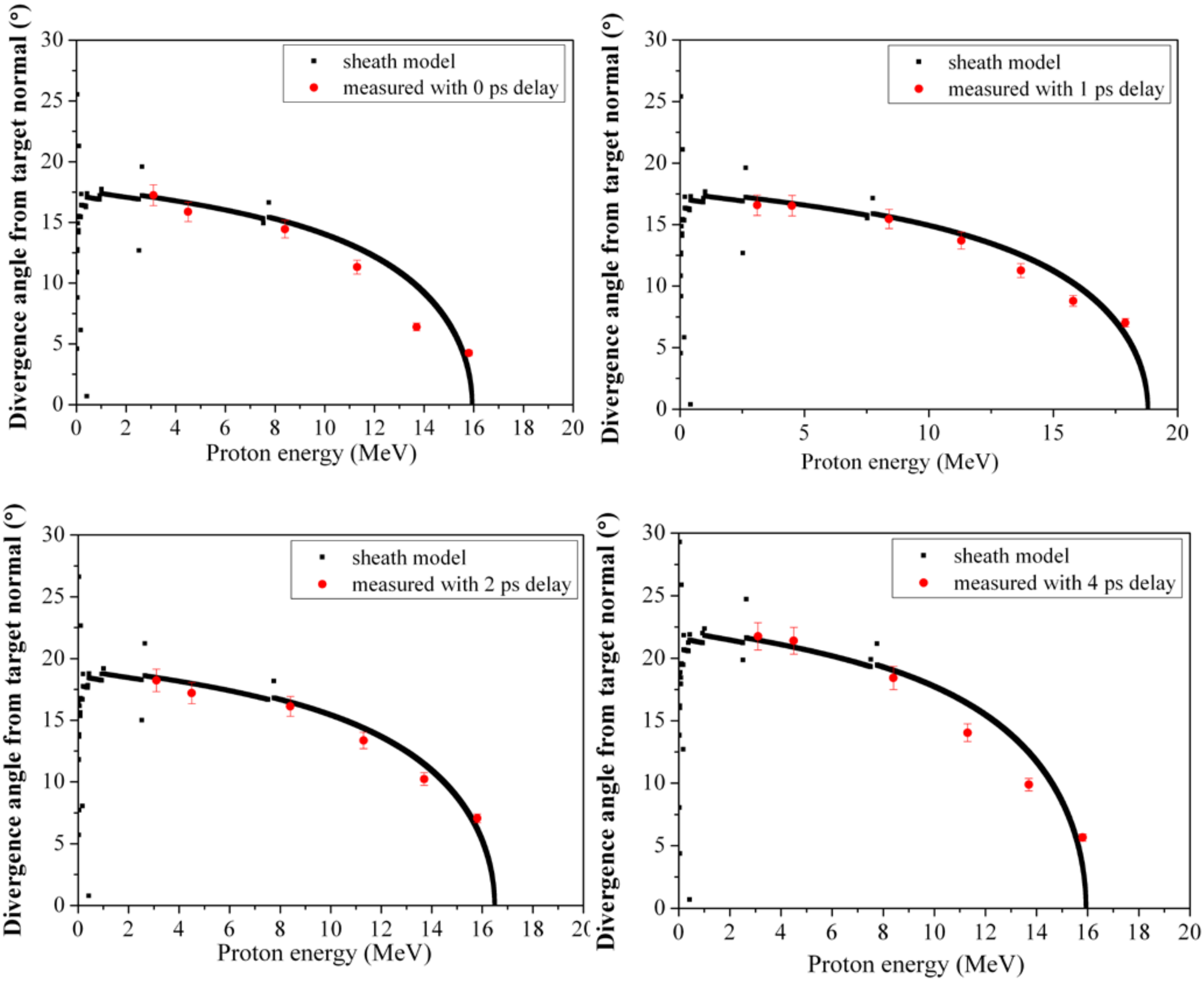

Figure A.3: Measured (red) and modelled (black) values of half angle divergence plotted as a function of proton energy for targets of thickness 125 μm.